universität wien

MASTERARBEIT / MASTER'S THESIS

Titel der Masterarbeit / Title of the Master's Thesis

„MEASURING THE HYDROGEN GROUND STATE HYPERFINE SPLITTING THROUGH THE π_1 AND σ_1 TRANSITIONS“

verfasst von / submitted by

Sergio Arguedas Cuendis, BSc

angestrebter akademischer Grad / in partial fulfilment of the requirements for the degree of

Master of Science (MSc)

Wien, 2017 / Vienna, 2017

Studienkennzahl lt. Studienblatt / degree programme code as it appears on the student record sheet:	A 0600121
Studienrichtung lt. Studienblatt / degree programme as it appears on the student record sheet:	Masterstudium Physik
Betreut von / Supervisor:	Hon.-Prof. Dipl.-Phys. Dr. Eberhard Widmann
Mitbetreut von / Co-Supervisor:	

Abstract

The ASACUSA collaboration is aiming to measure the ground state hyperfine structure (GSHS) of antihydrogen to test the CPT symmetry in a Rabi like experiment. The GSHS of hydrogen is a very precisely known value. In addition the hyperfine splitting frequency is a small quantity, therefore a comparison with antihydrogen has the potential to yield one of the most precise tests of the CPT symmetry on an absolute energy scale. A good characterization of the experiment's spectrometry is a premise to achieve a high precision. The high cost and the low production rates of antihydrogen require alternative methods for this characterization and justify the use of matter for such preparations. For this reason the Stefan Meyer Institute (SMI) as part of the ASACUSA collaboration constructed a hydrogen beam experiment. This will help to shorten the time frame needed for the antihydrogen measurements.

The main components of the hydrogen-beam setup are: a source of cold, modulated atomic hydrogen, a set of permanent sextupoles for polarization, a cavity to induce the spin flips, McKeehan-like coils to produce a homogeneous external magnetic field, another set of permanent sextupoles for state analysis and a quadropole mass spectrometer as detector. The same cavity is going to be used on the antihydrogen experiment and hence its characterization is highly relevant.

Within the scope of this work, the cavity and coils assembly was modified to enable measurements of two transitions. While the σ_1-transition has been accessible by the previous setup as well, the π_1-transition requires an improved external magnetic field homogeneity of $(\sigma_B/|B|) \leq 1000$ ppm. Therefore a new shielding as well as new McKeehan-like coils have been constructed. The characterization of these two new pieces of equipment is also part of the present work and a homogeneity of $(\sigma_B/|B|) \approx 590$ ppm has been verified.

Both π_1 and σ_1 transitions in hydrogen were measured for the first time using an upgraded setup. From these results the GSHS at zero magnetic field are calculated by extrapolation using the π_1 or σ_1 transitions separately and it will also be calculated using both transitions at the same static magnetic field. The results presented in this work of the GSHS using the π_1 extrapolation are the first results ever made using this method.

The obtained GSHS result has the value of $\nu_0 = (1420405753 \pm 8)$ Hz using both transitions at the same static magnetic field. For the π_1 extrapolation, $\nu_0 = (1420405760 \pm 34)$ Hz. For the σ_1 extrapolation, $\nu_0 = (1420405767 \pm 15)$ Hz.

Zusammenfassung

Die ASACUSA Kollaboration arbeitet an einer Messung der Hyperfeinstruktur von Antiwasserstoff im Grundzustand (GSHS) mittels Rabi Spektroskopie, um die CPT Symmetrie zu testen. Die Hyperfeinstruktur von Wasserstoff wurde mit hoher Präzision bestimmt, weshalb der Vergleich mit diesem Wert für Antiwasserstoff auf einer absoluten Energieskala potenziell einer der genauesten Tests der CPT Symmetrie werden kann. Eine gute Charakterisierung des Spektrometers für dieses Experiment ist eine Voraussetzung, um die angestrebte Präzision zu erreichen. Der hohe Aufwand, der für die Produktion selbst von geringen Mengen von Antiwasserstoff erforderlich ist, verlangt nach alternativen Ansätzen für die Charakterisierung und rechtfertigt vorbereitende Messungen mit Materie. Aus diesem Grund hat das Stefan-Meyer-Institut (SMI) als Teil der ASACUSA Kollaboration ein Wassserstoffstrahlexperiment aufgebaut. Dieses wird dazu beitragen, dass der Zeitbedarf der Antiwasserstoffexperimente reduziert werden kann.

Die Hauptkomponenten des Wasserstoffstrahlexperiments sind: Eine Quelle von gekühlten und modulierten atomaren Wasserstoff; ein Set von Permanentsextupolmagneten für die Polarisation des Strahls; ein Hohlraumresonator um die Hyperfeinübergänge zu treiben; McKeehan-artige Spulen um ein konstantes externes Magnetfeld zu generieren; ein weiteres Set von Permanentsextupolmagneten zwecks Analyse der Zustände; und ein Quadrupolmassenspectrometer als Wasserstoffdetektor.

Im Rahmen der vorliegenden Arbeit wurde der Hohlraumresonator und Spulen-Aufbau verbessert, um die Untersuchung von zwei Hyperfeinübergängen zu ermöglichen. Während bereits im vorangegangen Aufbau der σ_1-Übergang zugänglich war, verlangt die Untersuchung des π_1-Übergangs eine verbesserte Homogenität des externen Magnetfeldes auf $(\sigma_B/|B|) \leq 1000$ ppm. Deshalb wurden eine neue Magnetfeldabschirmung und McKeehan-artige Spulen konstruiert. Die Charakterisierung dieser neuen Bauteile ist ein wesentlicher Bestandteil dieser Arbeit und ein erreichter Wert von $(\sigma_B/|B|) \approx 590$ ppm konnte verifiziert werden.

Sowohl der σ_1- als auch der π_1-Übergang wurden zum ersten Mal unter Verwendung der neuen Abschirmung und Spulen vermessen. Von diesen Ergebnissen lässt sich die Hyperfeinstrukturaufspaltung von Wasserstoff im Grundzustand im feldfreien Fall ableiten. Die beiden Übergange erlauben unabhängig von einander die Extrapolation zum Nullfeld und alternativ können auch die Ergebnisse beider Übergänge beim gleichen Magnetfeldwert für eine Bestimmung benutzt werden. Die Extrapolationsmethode basierend auf dem π_1-Übergang wurde im Rahmen dieser Arbeit zum ersten Mal angewandt. Die Ergebnisse dieser Messungen sind alle innerhalb einer Standardabweichung in Übereinstimmung mit dem Literaturwert: $\nu_0 = (1420405753 \pm 8)$ Hz für die Methode mit beiden Übergängen beim gleichen externen Magnetfeld; $\nu_0 = (1420405760 \pm 34)$ Hz für die Extrapolation der Ergebnisse mittels π_1-Übergängen; und $\nu_0 = (1420405767 \pm 15)$ Hz für die Extrapolation der Ergebnisse mittels σ_1-Übergängen.

Acknowledgements

First and foremost, I would like to thank my parents Beatriz Cuendis Olaso and Felipe Arguedas Gamboa for all the support they have given me during my entire life. I would not be who I am without them.

I would also like to thank professor Eberhard Widmann for giving me the opportunity to be part of this project as well as for supervising this work and for all the help and advises he gave me during my period at SMI.

Another person who was a big part of this work is Dr. Martin C Simon. Thank you very much for supervising this thesis, but more importantly for all the time and patience you invested in explaining and discussing with me every single aspect of the experiment. I appreciate it.

Finally, I would also like to thank all my colleagues at SMI, CERN and the university of Vienna who helped during this process.

Contents

1 Introduction

1.1 Motivation

The Standard Model (SM) of elementary particles is a mathematical model that describes the different interactions of the elementary particles. The main components of the SM are the gauge bosons which transmit the particle interactions (electromagnetic, strong and weak) and the fermions (leptons and quarks) which make up the known matter. The SM is currently the best description of subatomic physics. Nevertheless, there are still many known phenomena that cannot be explained by the SM. For example, gravity is not included in the SM. Also, it does not answer fundamental questions as why there are three generations of quarks and leptons, or why only matter has been found so far in the universe. Since the SM is not complete, extensions to this model are needed.

A new theory with all the proper mathematical and physical properties can be developed, but it has to also be experimentally proven. Having that in mind, very well known systems are the perfect candidates to test a new theory. There is probably no better known system than the hydrogen atom and atomic spectroscopy allows for extremely precise investigation of its properties. Due to its comparatively simple structure, theoretical calculation can reach high precision as well. As a result hydrogen is an ideal test-bench for theory.

A very important achievement of the last century was the prediction and discovery of antimatter. In 1927 Dirac discovered the equation that nowadays bears his name. The modification of Schrödinger's equation is motivated by the relativistic relationship of energy and momentum: $E^2 - p^2c^2 = m^2c^4$. At first, this was a troublesome equation because it admits a negative energy solution $E = -\sqrt{m^2c^4 + p^2c^2}$. It were Feynman and Stukelberg who came up with the idea of seeing the negative energy solution as a positive energy state of new particle or anti-particle. This idea was experimentally proven by Anderson in 1932 with the discovery of the positron [1]. Shortly after that more anti-particles were found. A noteworthy milestone in antimatter research was the first formation of antihydrogen [2]. With the availability of antiatoms and other exotic atoms precise atomic spectroscopy methods became applicable to this field of physics.

The Atomic Spectroscopy And Collisions Using Slow Antiprotons (ASACUSA) collaboration has been developing a beam line to produce and investigate antihydrogen. Antihydrogen was chosen because it is the only antiatom that can be produced at low energy in sufficient amounts to perform spectroscopy. In addition hydrogen is one of the best known and characterized atoms. A comparison between the antihydrogen and hydrogen properties offers a test of fundamental symmetries in nature, especially the combined symmetry of Charge conjugation, Parity and Time reversal (see section 2.1). The CPT symmetry predicts the same properties for each particle-antiparticle pair.

The ground-state hyperfine structure (GSHS) of antihydrogen is the first spectroscopic property that will be investigated by the ASACUSA collaboration. The main reason to choose this transition is given by the Standard Model extension (SME) developed by the Kostelecký group [3, 4]. In this model small deviations for the energy levels of antihydrogen compared to the hydrogen ones can be caused by the violation of the CPT symmetry (see section 2.1 and 2.4). Since the predicted deviation is at an absolute energy scale, it can be detected at a much smaller relative precision, when a transition with a small energy is probed. This makes the hyperfine structure transition preferable over the 1S - 2S transition.

1.2 ASACUSA H-Beam

The most precise measurements of the GSHS were performed with hydrogen masers [5–8]. However, since the high precision is due to the hydrogen being kept in a storage bulb within

the microwave resonator, this technique is not applicable to antihydrogen. ASACUSA therefore plans to create a beam of antihydrogen atoms and to perform a Rabi type measurement (see section 2.4) of the GSHS transition.

Antiprotons from the antiproton decelerator (AD) of CERN are mixed with positrons in a dedicated trap, which then emits a beam of antihydrogen atoms. However, the production of antihydrogen is extremely difficult. Most of the beam time is currently used to optimize the production of antihydrogen and to test the improvements made on the detector. In order to test and characterize the spectroscopy beamline of the antihydrogen experiment, an atomic hydrogen source was constructed at SMI and transported to CERN. A good understanding and characterization is essential and can shorten the required amount of antiproton beam time for the measurement of the GSHS of antihydrogen.

Within the GSHS there are two transitions of importance to this work, the so called π_1 and σ_1 transitions (see section 2.2.2). The π_1-transition is of high interest, since only it could be sensitive to CPT violations according to the SME. For the measurement of the π_1-transition an extremely homogeneous magnetic field is needed, therefore only the σ_1-transition has been measured with the ASACUSA hydrogen beam so far (see [9]). Within this work, the existing setup was improved to incorporate the ability of measuring the π_1-transition. The first results show, that a similar precision as for the σ_1-transition is reached (see chapter 5).

Even though the H-beam was initially constructed to support the antihydrogen experiment, the actual setup could make its own contribution to test the SME (see chapter 6).

2 Theoretical Background

2.1 CPT Symmetry

The transformation of an object, which leaves this object unchanged, is known as a symmetry transformation. The set of symmetry transformations is known as a symmetry group. In physics the understanding of nature's symmetries has been a field of study for many years. Many experiments have been developed in order to measure and test these symmetries. Any conserved symmetry comes with a conserved physical quantity. For example, the momentum is conserved in all systems which are invariant under a translational transformation, the energy under invariant time transformation, and angular momentum under invariant rotational transformation.

In addition to the aforementioned continuous transformations, there are also discrete symmetries, for example charge conjugation, parity and time reversal (see figure 1). If for instance, someone reverses all the signs of the electrical charges, the fields and potentials will reverse their sign, but the force will stay the same. This means, that classical electrodynamics is invariant under charge conjugation. The charge operation transforms the particle to its antiparticle: $\mathrm{C}\langle\psi| \rightarrow \langle\bar{\psi}|$. It reverses the charge, baryon number and lepton number, but the mass, energy and spin are unchanged. The parity transformation mirrors the position of the particle. In other words, it swaps the spatial components: $\mathrm{P}(\vec{x}) \rightarrow (-\vec{x})$.

It was expected that physical laws obey charge and parity symmetry. The weak decay, however, proved this wrong. The decay of cobalt 60 was the first proof of a P violation [10]. The weak decay also violates the C operator. In the Standard Model all neutrinos are left handed (helicity of -1) and the antineutrino right handed (helicity of $+1$). Applying the C operator on a neutrino will give a left handed antineutrino.

The combination of both of Charge and Parity is called the CP symmetry. This symmetry was assumed to be conserved until 1964, when it was found that the decay of the neutral Kaon violates the CP symmetry [11]. The T operator is a time-reversal transformation: $\mathrm{T}(t) \rightarrow -t$. If the T symmetry is conserved, it is not possible to distinguish if the time is going backwards or forwards in the studied process. From a quantum field theory with Lorentz invariance, locality and energy positivity follows that the Charge-Parity-Time (CPT) symmetry is an invariant symmetry. The CPT theorem states that any physical system that undergoes a Charge, Parity and Time transformation is unchanged. In QFT a particle is defined as a localized quantized excitation of a relativistic invariant quantum field. These excitation are distinguished from each other by parameters like mass, spin and charge. In quantum field theories (QFT) like the Standard Model and Quantum Electrodynamics these excitations are invariant under CPT operations. To prove the CPT theorem the underlying model has to be Lorentz invariant [12, 13]. For that reason it is said that the CPT theorem is based on Lorentz invariance and quantum field theory.

The CPT theorem predicts identical properties for particle and antiparticles. A comparison opens a direct way for experiments to test the CPT symmetry. An outstanding candidate for these tests is the $\mathrm{H}/\bar{\mathrm{H}}$ pair. Comparing the hyperfine structure of both is a promising CPT test, because a CPT symmetry violation is possible in some SME, which means that the hyperfine structure transition could be different for particles and antiparticles.

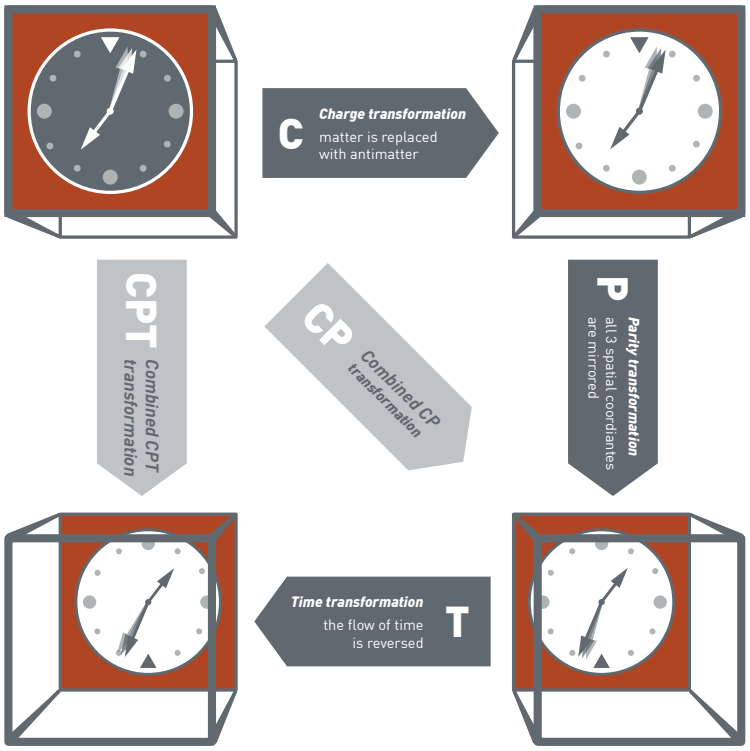

Figure 1: Illustration of the CPT transformation (made by Doris Pristauz-Telsnigg)

2.2 Hydrogen Atom

The main focus of this and the next section is the analysis of the hydrogen ground state. In a quantum mechanical system the ground state is the state of lowest energy. For hydrogen it means that the electron is at the lowest possible orbit. In hydrogen, the energy difference between the ground state and the first excited energy state is around 10 eV. Even though the ground state of hydrogen is divided into 4 sub-states (as shown later in this section), the energy difference between these states is much smaller than the 10 eV between the ground state and the first excited state. For that reason, one talks of 4 ground states of hydrogen.

2.2.1 Ground State Splitting

The hydrogen atom is made up of an electron bound to a proton. Both particles have an intrinsic angular momentum or spin. The spin can take two possible values defined here just as up ($\uparrow$) or down ($\downarrow$). That means, there are 4 possible configurations for the proton and electron spin:

$$\begin{aligned} \text{State I: } &|\uparrow\uparrow\rangle \,; \text{electron spin up, proton spin up} \\ \text{State II: } &|\uparrow\downarrow\rangle \,; \text{electron spin up, proton spin down} \\ \text{State III: } &|\downarrow\uparrow\rangle \,; \text{electron spin down, proton spin up} \\ \text{State IV: } &|\downarrow\downarrow\rangle \,; \text{electron spin down, proton spin down} \end{aligned} \tag{1}$$

These shall be the selected base states of the hydrogen atom. Any state can be written as a linear combination of these states.

$$\begin{aligned} |\psi\rangle = &|\uparrow\uparrow\rangle \langle\uparrow\uparrow |\psi\rangle + |\uparrow\downarrow\rangle \langle\uparrow\downarrow |\psi\rangle \\ &+ |\downarrow\uparrow\rangle \langle\downarrow\uparrow |\psi\rangle + |\downarrow\downarrow\rangle \langle\downarrow\downarrow |\psi\rangle \end{aligned} \tag{2}$$

The brackets can be written as complex numbers K_i, where i = 1,2,3 or 4.

$$|\psi\rangle = |\uparrow\uparrow\rangle K_1 + |\uparrow\downarrow\rangle K_2 + |\downarrow\uparrow\rangle K_3 + |\downarrow\downarrow\rangle K_4 \tag{3}$$

If these four amplitudes change with time, the rate of change in time is given by the Hamiltonian operator. If the Hamiltonian does not depends explicitly on the time, these amplitudes will stay unchanged. Any Hamilton operator for a single half-spin particle can be written using the Pauli matrices $\vec{\sigma}$. The spin operator is defined as $\hat{S} = \frac{\hbar \cdot \vec{\sigma}}{2}$. For a system with two half-spins, the $\vec{\sigma}$ matrices can be also used, but in this case one has to define two sets of $\vec{\sigma}$ matrices. One set acts only on the electron spin ($\vec{\sigma}^e$) and the other one acts only on the proton spin ($\vec{\sigma}^p$).

For a four state system the Hamiltonian has to be a four by four matrix. If one takes all possible combinations of the $\vec{\sigma}^e$ and $\vec{\sigma}^p$ matrices (9 combinations) plus all the single matrices (6 matrices) plus the unitary matrix $\hat{I}$, there all 16 possibilities in total. Any four by four matrix can be written as a linear combination of these 16 matrices. That means, the Hamiltonian is a linear combination of these matrices. To find the right combination a space symmetry approach shall be used. The Hamiltonian has to be independent of the direction of the x-,y- and z-axes and it has to be invariant under any rotation of the coordinate system. The only possible combination of the 16 matrices that fulfills the invariant requirement is:

$$\begin{aligned} \hat{H} &= E_r \cdot \hat{I} + C \cdot (\hat{S}^e \otimes \hat{S}^p), \\ \hat{H} &= E_r \cdot \hat{I} + \frac{C \cdot \hbar^2}{4} \cdot (\vec{\sigma}^e \otimes \vec{\sigma}^p), \\ \hat{H} &= E_r \cdot \hat{I} + D \cdot (\vec{\sigma}^e \otimes \vec{\sigma}^p), \end{aligned} \tag{4}$$

where $D = \frac{C \cdot \hbar^2}{4}$ and $\otimes$ is the tensor product.

The E_r depends on the level chosen to measure the energies from. For now E_r is going to be equal to zero.

The Schrödinger equation is defined as:

$$i\hbar\dot{\psi} = \hat{H}\psi \tag{5}$$

Using equation (3), equation (5) can be re-written as:

$$i\hbar\dot{K_i} = \sum_j H_{ij} K_j \tag{6}$$

Using equation (6), one can calculate the spin interaction due to the energy level. This can be done by calculating $H_{ij} = \langle i | \hat{H} | j \rangle$ with i and j = I,II,III or IV the four base states. H_{ij} can be calculated using the properties of the Pauli matrices when applied to the up ($\uparrow$) or down state ($\downarrow$). These properties are listed in table 1.

Table 1: Pauli matrices acting on the up ($\uparrow$) or down state ($\downarrow$)

	$\|\uparrow\rangle$	$\|\downarrow\rangle$
σ_x	$\|\downarrow\rangle$	$\|\uparrow\rangle$
σ_y	i$\|\downarrow\rangle$	-i$\|\uparrow\rangle$
σ_z	$\|\uparrow\rangle$	$-\|\downarrow\rangle$

Working out these scalar products gives the following H_{ij} matrix:

$$H_{ij} = \begin{bmatrix} D & 0 & 0 & 0 \\ 0 & -D & 2D & 0 \\ 0 & 2D & -D & 0 \\ 0 & 0 & 0 & D \end{bmatrix} \tag{7}$$

Using this matrix and equation (6) gives four differential equations:

$$\begin{aligned} i\hbar\dot{K_1} &= DK_1 \\ i\hbar\dot{K_2} &= -DK_2 + 2DK_3 \\ i\hbar\dot{K_3} &= 2DK_2 - DK_3 \\ i\hbar\dot{K_4} &= DK_4 \end{aligned} \tag{8}$$

Finally, for stationary states like the ones here (the Hamiltonian is time independent), the K_i amplitudes can be expressed as:

$$K_i = a_i e^{-(\frac{i}{\hbar})Et} \tag{9}$$

Where a_i are time independent variables. This gives the final linear equations:

$$\begin{aligned} Ea_1 &= Da_1 \\ Ea_2 &= -Da_2 + 2Da_3 \\ Ea_3 &= 2Da_2 - Da_3 \\ Ea_4 &= Da_4 \end{aligned} \tag{10}$$

the solution of these equations delivers the final states and the corresponding energy:

$$|1\rangle = |I\rangle = |\uparrow\uparrow\rangle \text{, with } E_1 = D \tag{11}$$

$$|2\rangle = \frac{|II\rangle + |III\rangle}{\sqrt{2}} = \frac{|\uparrow\downarrow\rangle + |\downarrow\uparrow\rangle}{\sqrt{2}} \text{, with } E_3 = D \tag{12}$$

$$|3\rangle = |IV\rangle = |\downarrow\downarrow\rangle \text{, with } E_2 = D \tag{13}$$

$$|4\rangle = \frac{|II\rangle - |III\rangle}{\sqrt{2}} = \frac{|\uparrow\downarrow\rangle - |\downarrow\uparrow\rangle}{\sqrt{2}} \text{, with } E_4 = -3D \tag{14}$$

The interaction between the proton and the electron spin leads to a singlet state with total angular momentum F = 0 and a triple state with F = 1 (see Figure 2).

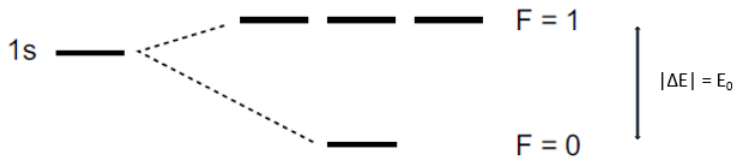

Figure 2: Hydrogen ground state splitting due to proton-electron spin interaction

The energy gap between the singlet and the triplet will be defined as E_0. In equations (11) to (14), the energy was given in terms of a value D. Using the definition of E_0 the value of D becomes $D = \frac{E_0}{4}$.

The transition frequency between these two levels is one of the most accurately measured quantities [6, 14] :

$$\nu_{\text{HF}} = 1420405751.768 \pm 0.002\text{Hz} \tag{15}$$

corresponding to a relative precision of $1.4 \cdot 10^{-12}$.

2.2.2 Zeeman splitting

In the last section, it was shown that the ground state of hydrogen is divided into 4 states. Three of them have the same energy and the other has a lower energy. In the presence of an external magnetic field, the energy levels will split and shift. This splitting of the energy level is known as the Zeeman effect.

The analysis done in the last section has to be repeated for a Hamiltonian, which includes the interaction with the external magnetic field.

$$\begin{aligned}\hat{H} &= C(\hat{S}^e \cdot \hat{S}^p) - \mu_e \frac{1}{\hbar}\hat{S}^e\vec{B} - \mu_p \frac{1}{\hbar}\hat{S}^p\vec{B} \\ \hat{H} &= \frac{E_0}{4}(\vec{\sigma}^e \cdot \vec{\sigma}^p) - \frac{\mu_B \cdot g_J}{2}\vec{\sigma}^e\vec{B} - \frac{\mu_B \cdot g_I}{2}\vec{\sigma}^p\vec{B}\end{aligned} \tag{16}$$

Where $\mu_e = \frac{g_J\mu_B}{\hbar}$ and $\mu_p = \frac{g_I\mu_B}{\hbar}$.

The first term in the right hand side of the equation (16) has been computed already. For a constant magnetic field in the z-direction one can define the other terms of equation (16) as:

$$\hat{H^1} = -(\mu_J\sigma_z^e + \mu_I\sigma_z^p)B \tag{17}$$

Where $\mu_J = \frac{g_J\mu_B}{2}$ and $\mu_I = \frac{g_I\mu_B}{2}$.

Applying $\hat{H^1}$ on the four states of equation (1), one can see that the matrix $\hat{H^1_{ij}} = \langle i|\hat{H^1}|j\rangle$ will have only diagonal elements.

$$\begin{aligned}\hat{H^1}\,|\uparrow\uparrow\rangle &= -(\mu_J + \mu_I)B\,|\uparrow\uparrow\rangle \\ \hat{H^1}\,|\uparrow\downarrow\rangle &= -(\mu_J - \mu_I)B\,|\uparrow\downarrow\rangle \\ \hat{H^1}\,|\downarrow\uparrow\rangle &= -(-\mu_J + \mu_I)B\,|\downarrow\uparrow\rangle \\ \hat{H^1}\,|\downarrow\downarrow\rangle &= \quad(\mu_J + \mu_I)B\,|\downarrow\downarrow\rangle\end{aligned} \tag{18}$$

The final $\hat{H^f_{ij}}$ is the addition of $\hat{H_{ij}}$ and $\hat{H^1_{ij}}$:

$$H^f_{ij} = \begin{bmatrix} D - (\mu_J + \mu_I)B & 0 & 0 & 0 \\ 0 & -D - (\mu_J - \mu_I)B & 2D & 0 \\ 0 & 2D & -D + (\mu_J - \mu_I)B & 0 \\ 0 & 0 & 0 & D + (\mu_J + \mu_I)B \end{bmatrix} \tag{19}$$

Adding these terms to equation (10) gives the linear equations for finding the energies in presence of an external magnetic field.

$$Ea_1 = H^f_{11} \cdot a_1 \tag{20}$$

$$Ea_2 = H^f_{22} \cdot a_2 + H^f_{23} \cdot a_3 \tag{21}$$

$$Ea_3 = H^f_{32} \cdot a_2 + H^f_{33} \cdot a_3 \tag{22}$$

$$Ea_4 = H^f_{44} \cdot a_4 \tag{23}$$

Equation (20) and (23) are independent from equation (21) and (22). For equation (20) one can take a_1=1 and $a_2, a_3, a_4 = 0$. For equation (23), a_4=1 and $a_2, a_3, a_1 = 0$. Equation (21) and (22) have to be solved simultaneously. One calculates the $\frac{a_2}{a_3}$ ratio for both equations:

$$\frac{a_2}{a_3} = \frac{H^f_{23}}{E - H^f_{22}} \tag{24}$$

$$\frac{a_2}{a_3} = \frac{E - H^f_{33}}{H^f_{32}} \tag{25}$$

Subtracting these two ratios, one gets a quadratic equation for E:

$$(E - H^f_{22})(E - H^f_{33}) - H^f_{32} \cdot H^f_{23} = 0 \tag{26}$$

which has the following solutions:

$$E = \frac{H^f_{22} + H^f_{33}}{2} \pm \sqrt{\frac{(H^f_{22} - H^f_{33})^2}{4} + H^f_{23} H^f_{32}} \tag{27}$$

The solution of equations 20 to 23 is known as the Breit-Rabi formula for the hyperfine splitting of the hydrogen ground state. Applying these values to H^f_{ij}, one gets the following equations:

$$E_1 = \frac{E_0}{4} + \frac{1}{2}(g_J + g_I)\mu_B B, \text{ State } |1\rangle \tag{28}$$

$$E_2 = -\frac{E_0}{4} + \frac{E_0}{2}\sqrt{1 + \frac{(g_J - g_I)^2 \mu_B^2 B^2}{E_0^2}}, \text{ State } |2\rangle \tag{29}$$

$$E_3 = \frac{E_0}{4} - \frac{1}{2}(g_J + g_I)\mu_B B, \text{ State } |3\rangle \tag{30}$$

$$E_4 = -\frac{E_0}{4} - \frac{E_0}{2}\sqrt{1 + \frac{(g_J - g_I)^2 \mu_B^2 B^2}{E_0^2}}, \text{ State } |4\rangle \tag{31}$$

Where $g_J = -2.00231930436182(52)$ [15] is the Landé factor of the coupled spin angular momentum ($g_J = |g_e|$ for $J = 1/2$) and $g_I = g_p m_e/m_p$ with $g_P = 5.585694702(17)$ the proton g-factor, $m_e = 9.10938356(11) \cdot 10^{-31}$ kg, the electron mass, $m_p = 1.672621898(21) \cdot 10^{-27}$ kg, the proton mass [15] and $\mu_B = 5.7883818012(26) \cdot 10^{-5}\text{eVT}^{-1}$ [15] the Bohr magneton.

Taking a closer look at the equations (28) - (31) it can be seen that the three states making up the triplet are going to split. The first state (equation (28)) increases linearly with B, the third state (equation (30)) decreases linearly with B. The other two states have an hyperbolic B-dependence. For small B, they depend quadratically on B, for large B they approach a straight line.

Figure 3 shows the splitting of the hydrogen ground state in the presence of an external magnetic field.

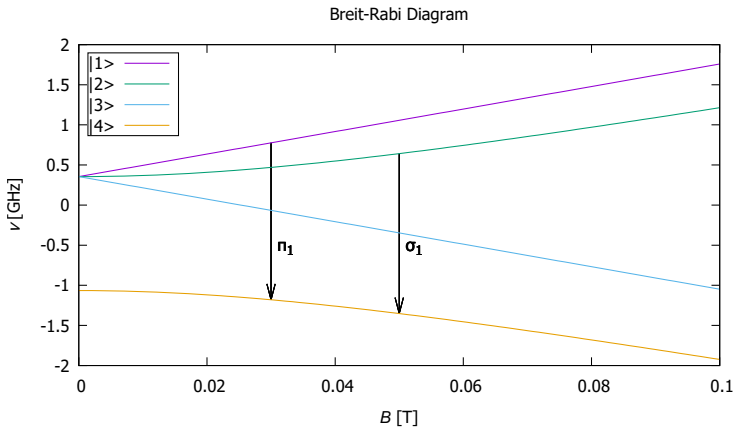

Figure 3: Hydrogen ground state hyperfine splitting

Moreover, the four states can be classified depending on their behavior inside an inhomogeneous magnetic field. States 1 and 2 move towards lower magnetic fields and are classified as low field seekers (LFS). States 3 and 4 move towards higher magnetic fields and are classified as high field seekers (HFS). This classification is also shown in figure 3.

The main focus of this work is to measure the π_1 and the σ_1 transitions. The σ_1 is the transition from state 2 to state 4 (Equation (32)). The π_1-transition is the one from state 1 to state 4 (Equation (33)).

$$\nu_{\sigma_1} = \frac{E_2 - E_4}{h} = \frac{E_0}{h}\sqrt{1 + \frac{(g_J - g_I)^2 \mu_B^2 B^2}{E_0^2}} \tag{32}$$

$$\nu_{\pi_1} = \frac{E_1 - E_4}{h} = \left(\frac{E_0}{2} + \frac{1}{2}(g_J + g_I)\mu_B B + \frac{E_0}{2}\sqrt{1 + \frac{(g_J - g_I)^2 \mu_B^2 B^2}{E_0^2}}\right) \cdot \frac{1}{h} \tag{33}$$

2.3 Two level system with an interaction Hamiltonian

In this section the influence of the oscillating magnetic field is going to be studied for a two level system. Consider a two level system with energies E_1 and E_2 and a transition frequency ω_t (see figure 4).

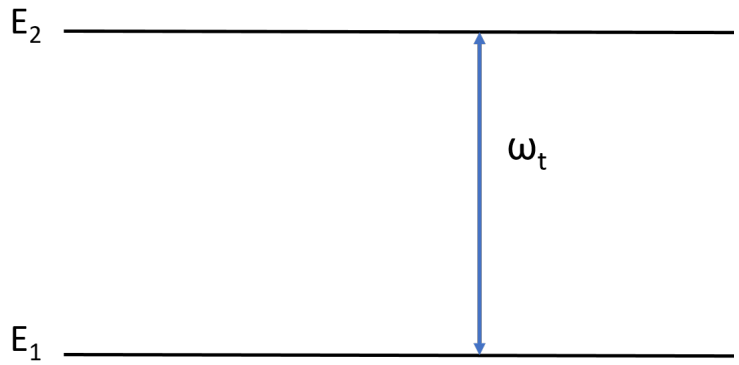

Figure 4: States $|1\rangle$ and $|2\rangle$ with corresponding energies E_1 and E_2 and transition frequency ω_t

Consider the Schrödinger equation (equation (5)), which has the solution of the form:

$$\Psi(\vec{r}, t) = \psi(\vec{r})\exp(-iEt/\hbar) \tag{34}$$

Inserting equation (34) in equation (5) gives:

$$\hat{H}\psi(\vec{r}) = E\psi(\vec{r}) \tag{35}$$

for a time independent Hamiltonian. For the two level system:

$$\begin{aligned} \hat{H}\psi_1(\vec{r}) &= E_1\psi_1(\vec{r}) \\ \hat{H}\psi_2(\vec{r}) &= E_2\psi_2(\vec{r}) \end{aligned} \tag{36}$$

These atomic states and the ones in section 2.2 are known as stationary states. Such a state has the property that the average value of an observable is independent of time, if the operator is time independent. All the Hamiltonians in section 2.2 do not depend on the time explicitly. Here it will be shown, that an oscillating magnetic field leads to the conversion of one state to the other. The Hamiltonian for the oscillating magnetic field is given by:

$$\hat{H}_I = \vec{\mu}\vec{B}\cos(wt) \tag{37}$$

This is known as the interaction Hamiltonian and is time dependent. That means, the wave equation has no longer stationary solutions. For the two level system the wave function is now given by a linear combination of both states with time-dependent coefficients C(t):

$$\Psi(\vec{r},t) = C_1(t)\Psi_1(\vec{r},t) + C_2(t)\Psi_2(\vec{r},t) \tag{38}$$

Inserting equation (38) into equation (5) gives:

$$\hat{H}_I(C_1\Psi_1 + C_2\Psi_2) = i\hbar\left(\Psi_1\frac{dC_1}{dt} + \Psi_2\frac{dC_2}{dt}\right) \tag{39}$$

Multiplying equation (39) by $\Psi_1^\star/\Psi_2^\star$, inserting it in equation (34) and integration over the whole space leads to [16]:

$$\langle 1|\,\hat{H}_I\,|1\rangle\,C_1 + \exp(-it\omega_t)\,\langle 1|\,\hat{H}_I\,|2\rangle\,C_2 = i\hbar\frac{dC_1}{dt} \tag{40}$$

$$\exp(-it\omega_t)\,\langle 2|\,\hat{H}_I\,|1\rangle\,C_1 + \langle 2|\,\hat{H}_I\,|2\rangle\,C_2 = i\hbar\frac{dC_2}{dt} \tag{41}$$

with,

$$\langle i|\,\hat{H}_I\,|j\rangle = \int dV\,\psi_i^\star\hat{H}_I\psi_j \tag{42}$$

Taking a closer look to equation (42), it can be concluded that $\langle i|\,\hat{H}_I\,|j\rangle = 0$ for i=j ($\psi/\psi^\star$ and $\hat{H}_I$ are odd functions). If ψ_1 and ψ_2 have opposite parity, the value for $\langle i|\,\hat{H}_I\,|j\rangle$ for i $\neq$ j is not zero. For the Hamiltonian given in equation (37) one gets [17]:

$$\langle i|\,\hat{H}_I\,|j\rangle = \mu_{ij}\cdot \mathrm{B_{osc}}\cos(\omega t), \text{ for i} \neq \text{j} \tag{43}$$

where $\mu_{ij} = \langle i|\mu|j\rangle$ is the magnetic transition moment between two states. Inserting these results into equations 40 and 41 gives:

$$\Omega_R C_2 \exp(-it\omega_t)\cos(\omega t) = i\frac{dC_1}{dt} \tag{44}$$

$$\Omega_R C_1 \exp(-it\omega_t)\cos(\omega t) = i\frac{dC_2}{dt} \tag{45}$$

with Ω_R equal to:

$$\Omega_R = \frac{\mu_{ij}\mathrm{B_{osc}}}{\hbar} \tag{46}$$

Ω_R is known as the Rabi frequency, which is the frequency of oscillation for a given atomic transition.

Furthermore, for an initial condition where all the particles are in one state (e.g. state $|1\rangle$) the initial expectation values are $|C_1(0)|^2 = 1$, $|C_2(0)|^2 = 0$. Using that $\cos(\omega t) = \frac{1}{2}\left(e^{i\omega t} + e^{-i\omega t}\right)$, the solutions for equations 44 and 45 at the resonance frequency $\omega = \omega_t$ are [17]:

$$|C_1(t)|^2 = \cos^2(\Omega_R t/2) \tag{47}$$

$$|C_2(t)|^2 = \sin^2(\Omega_R t/2) \tag{48}$$

Equations (47) and (48) describe the possibility of finding the system in state $|1\rangle$ or $|2\rangle$ after a time t.

2.3.1 Transition probabilities for the hydrogen ground state

The Rabi method is going to be used to measure the hyperfine structure of ground state hydrogen (see section 3.3). That means an oscillating magnetic field is going to be used to drive the transition from one state to another. Two transitions are going to be measured (see figure 3). The π_1 (state $|1\rangle$ to state $|4\rangle$) and σ_1 transitions (state $|2\rangle$ to state $|4\rangle$). At resonance only the two desired atomic states are going to be involved in the interactive process, which means in that means that both transitions can be treated as a two level system.

One of the key aspects of the Rabi method is the count drop at the detector at the resonance frequency. It is ideal to look for the oscillating magnetic field which maximizes the probability of a transition from one level to the other. The transition probability $|C_2(t)|^2$ given in equation (48) reaches a maximum at:

$$\Omega_R = \frac{\pi}{t} = \frac{\mu B_{\text{osc}}}{\hbar} \tag{49}$$

Finally, the Rabi frequency is related to the interaction Hamiltonian by:

$$\hbar\Omega_{ij} = \hat{H}_{ij} \tag{50}$$

The matrix element $\langle i|\hat{H}_I|j\rangle$ can be calculated to find the corresponding Rabi frequency for the π_1 and σ_1 transitions, or alternatively the required amplitude of B_{osc} for a given interaction time t to achieve one complete state conversion.

The σ_1-transition

The matrix element $\langle 4|\hat{H}_I|2\rangle$ has to be calculated for the σ_1-transition. For this transition the oscillating magnetic field has to be parallel to the static magnetic field (z direction). Any orthogonal component leads to vanishing matrix elements. The interaction Hamiltonian given in equation (37) takes the form:

$$\begin{aligned}
\hat{H}_I &= -\left(\mu_e \frac{1}{\hbar}\hat{S}^e\vec{B} + \mu_p \frac{1}{\hbar}\hat{S}^p\vec{B}\right)\cos(\omega t) \\
\hat{H}_I &= -\left(\frac{\mu_B \cdot g_J}{2}\vec{\sigma}^e\vec{B} + \frac{\mu_B \cdot g_I}{2}\vec{\sigma}^p\vec{B}\right) cos(\omega t) \\
\hat{H}_I &= -(\mu_J\sigma_z^e + \mu_I\sigma_z^p)\mathrm{B}_{\text{osc}}\cos(\omega t)
\end{aligned} \tag{51}$$

with the definition of μ_J and μ_I given in section 2.2.2. Plugging in the definition of states $|2\rangle$ and $|4\rangle$ (see equations 12 and 14), $\langle 4|\hat{H}_I|2\rangle$ takes the following form:

$$\begin{aligned}
\langle 4|\hat{H}_I|2\rangle =& \frac{K_1}{2}(\langle\uparrow\downarrow|\sigma_z^e|\uparrow\downarrow\rangle + \underbrace{\langle\uparrow\downarrow|\sigma_z^e|\downarrow\uparrow\rangle}_{=0} \\
&- \underbrace{\langle\downarrow\uparrow|\sigma_z^e|\uparrow\downarrow\rangle}_{=0} - \langle\downarrow\uparrow|\sigma_z^e|\downarrow\uparrow\rangle) \\
&+ \frac{K_2}{2}(\langle\uparrow\downarrow|\sigma_z^p|\uparrow\downarrow\rangle + \underbrace{\langle\uparrow\downarrow|\sigma_z^p|\downarrow\uparrow\rangle}_{=0} \\
&- \underbrace{\langle\downarrow\uparrow|\sigma_z^p|\uparrow\downarrow\rangle}_{=0} - \langle\downarrow\uparrow|\sigma_z^p|\downarrow\uparrow\rangle)
\end{aligned} \tag{52}$$

with $K_1 = -\mu_J\mathrm{B}_{\text{osc}}\cos(\omega t)$ and $K_2 = -\mu_I\mathrm{B}_{\text{osc}}\cos(\omega t)$. Using table 1 one can calculate the scalar products in equation (52). The second, third, sixth and seventh term from equation (52) are equal to zero because the up and down states form an orthonormal normal system. Working out the other terms give the following solution:

$$\langle 4|\hat{H}_I|2\rangle = -\frac{\mathrm{B_{osc}}}{2}\cos(\omega t)(\mu_B g_J - \mu_B g_I) \tag{53}$$

Finally, using equations (49), (50) and (53), the oscillating magnetic field needed for the σ_1-transition can be computed:

$$\begin{aligned} \Omega_{\sigma_1}\hbar &= \frac{\mathrm{B_{osc}}}{2}(\mu_B g_J - \mu_B g_I) \\ \mathrm{B}_{\sigma_1} &= \frac{2\pi\hbar}{t(\mu_B g_J - \mu_B g_I)} \end{aligned} \tag{54}$$

The π_1-transition

For the π_1-transition, the matrix $\langle 4|\hat{H}_I|1\rangle$ has to be calculated. For this transition the oscillating magnetic field has to be perpendicular to the static magnetic field. Here, a parallel oscillating magnetic field component would lead to vanishing matrix elements. Without loss of generality, $\vec{B}$ can be defined as:

$$\vec{B} = \mathrm{B_{osc}}\vec{x}\cos(\omega t) \tag{55}$$

It follows for the interaction Hamiltonian:

$$\hat{H}_I = -(\mu_J\sigma_x^e + \mu_I\sigma_x^p)\mathrm{B_{osc}}\cos(\omega t) \tag{56}$$

The same calculation as for the σ_1-transition is going to be made. First, the matrix element is going to be computed:

$$\begin{aligned} \langle 4|\hat{H}_I|1\rangle =& \frac{K_1}{\sqrt{2}}(\underbrace{\langle\uparrow\downarrow|\sigma_x^e|\uparrow\uparrow\rangle}_{=0} - \langle\downarrow\uparrow|\sigma_x^e|\uparrow\uparrow\rangle \\ &+ \frac{K_2}{\sqrt{2}}(\langle\uparrow\downarrow|\sigma_x^p|\uparrow\uparrow\rangle - \underbrace{\langle\downarrow\uparrow|\sigma_x^p|\uparrow\uparrow\rangle}_{=0}) \end{aligned} \tag{57}$$

Using table 1 one can calculate the scalar products in equation (57). The first and fourth term of equation (57) are equal to zero and the solution takes the following form:

$$\langle 4|\hat{H}_I|1\rangle = -\frac{\mathrm{B_{osc}}}{2\sqrt{2}}\cos(\omega t)(\mu_B g_I - \mu_B g_J) \tag{58}$$

With this result the oscillating magnetic field for the π_1-transition can be calculated:

$$\begin{aligned} \Omega_{\pi_1}\hbar &= \frac{\mathrm{B_{osc}}}{2\sqrt{2}}(\mu_B g_I - \mu_B g_J) \\ \mathrm{B}_{\pi_1} &= \frac{2\sqrt{2}\pi\hbar}{t(\mu_B g_I - \mu_B g_J)} \end{aligned} \tag{59}$$

Note that the equations (54) and (59) are not equal. A different B-field is needed to drive the π_1 and the σ_1 transitions. It is important to mention that the analysis done here is for a conventional Rabi experiment (see section 2.4). At the H-beam experiment a cavity with strip-line geometry is going to be used to provide the oscillating magnetic field (see section 3.7). The oscillating magnetic field is not constant along the axis parallel to the beam trajectory (see figure 18). The strip line geometry will cause the maximum of the state conversion probability to move to a higher oscillating magnetic field value (see figure 41); the ratio between the field amplitudes of $\sqrt{2}$ will stay the same.

2.4 Principle of Rabi Experiment

Isidor Isaac Rabi and his colleagues invented a new method to measure the magnetic moment of atoms and molecules and demonstrated it with an investigation on ${}_3\mathrm{Li}^6$, ${}_3\mathrm{Li}^7$, ${}_9\mathrm{F}^{19\star}$ [18]. For this method Rabi was awarded with the Nobel Prize in 1944. It works as follows: for a given classical nucleus with spin angular momentum $\hbar\vec{J}$, magnetic moment $\vec{\mu} = (\mu/J)\vec{J}$ and a static magnetic field $\vec{H}_{stat} = H_0 \cdot \vec{z}$, the equation of motion describing this system is given by:

$$\hbar \cdot \frac{d\vec{J}}{dt} = \vec{\mu} \times \vec{H}_{stat} \tag{60}$$

The nucleus' spin will precess around the magnetic field axis. From equation (60) one can calculate the angular frequency for this precession, which is known as the Larmor frequency [7]:

$$\omega_0 = 2\pi\nu_0 = \frac{\mu H_{\mathrm{stat}}}{\hbar J} \tag{61}$$

The Rabi method is based on a precise measurement of the Larmor frequency in order to compute the magnetic moment. For the measurement of the Larmor frequency, a rotating magnetic field perpendicular to the static magnetic field will be applied to the system. For a given rotation angular frequency ω and magnetic field $\vec{H}_{rot}$. In the rotating frame, the equation of motion is:

$$\hbar \cdot \frac{d\vec{J}_R}{dt} = \hbar \cdot \frac{d\vec{J}}{dt} - \vec{J} \times \vec{\omega} \tag{62}$$

Inserting equation (60) into equation (62) gives:

$$\hbar \cdot \frac{d\vec{J}_R}{dt} = \cdot\frac{\mu}{J\hbar}\vec{J} \times (\vec{H}_{stat} + \vec{H}_{rot}) - \vec{J} \times \vec{\omega} \tag{63}$$

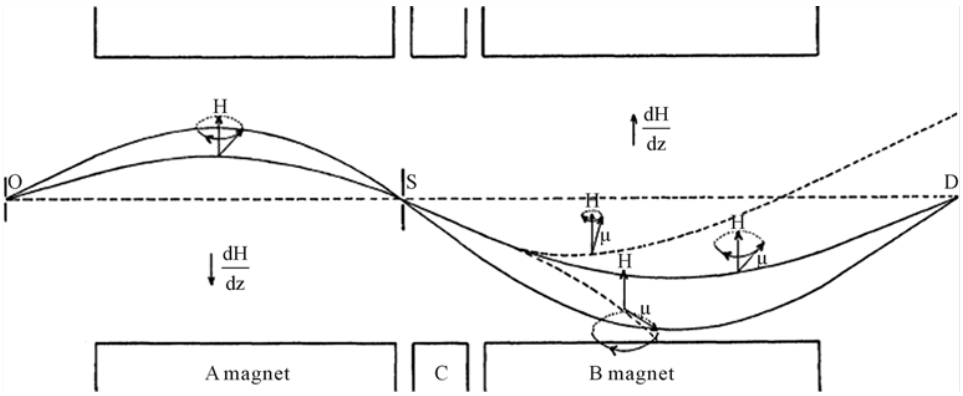

Figure 5: Rabi's experimental setup [18]

If $\omega_0 = \omega$, the first and last terms of equation (63) cancel each other, and the precession is around $\vec{H}_{rot}$. Since $\vec{H}_{rot}$ is perpendicular to $\vec{H}_{stat}$, the spin is able to flip between up and down. In practice, an oscillating magnetic field can be used instead of the rotating magnetic field [18]. For a known static magnetic field, ν_0 can be measured by making a scan over ω.

Figure 5 shows the experimental setup of Rabi's method. Here, the source "O" sends a beam of particles in a high vacuum beam line. The A-magnet section produces an inhomogeneous magnetic field, with a gradient (dH/dZ) pointing downwards. The particles inside this section will follow different paths depending on their μ_z and their velocity. A slit "S"

at the end of this section will function as a path selector. Only the particles with a specific combination of μ_z and v will pass through the slit (solid lines in figure 5).

The B-magnet section produces an inhomogeneous magnetic field, but pointing in the other direction. The value of the gradient is set to be the same for the A-magnet and B-magnet. The particles going through the B-magnet section will then be redirected to the detector "D" (solid lines in figure 5).

Finally, both the static and the oscillating magnetic field are produced in the C-region of the experiment. As explained before, due to both magnetic fields the particle spin can flip between the two states. This will change the value of μ_z if the frequency is right. If the spin is flipped the particle will now follow a different trajectory within the field gradients of the B-magnet and will not arrive at the detector (dotted lines in figure 5). When performing a frequency scan the number of counts at the detector will drop and reach a minimum when the frequency of the oscillating magnetic field is equal to the Larmor frequency. Thus, the transition frequency (or resonance frequency) can be extracted by a fit to the observed count rate spectrum.

2.5 Standard Model Extension

The Standard Model is not a complete theory because it does not include gravity and can not describe all processes present in nature (e.g. neutrino oscillations). For that reason, physicists have developed new extensions of the Standard Model (Standard Model Extensions, SME).

A group of theorists led by Alan Kostelecký has developed an SME where they combine the SM with gravity [3]. In this model microscopic violations of the Lorentz symmetry and the CPT symmetry are allowed.

According to this SME, additional terms due to the symmetry violation are added to the Lagrangian. These modifications have a direct impact on the energy splitting of the H/$\bar{\text{H}}$. The Breit-Rabi equations get the extra energy terms:

$$\begin{aligned}
E_1 &= \frac{E_0}{4} + (g_J + g_I)\mu_B B + \Delta E_1 \\
E_2 &= -\frac{E_0}{4} + \frac{E_0}{2}\sqrt{1 + \frac{(g_J - g_I)^2\mu_B^2 B^2}{E_0^2}} + \Delta E_2 \\
E_3 &= \frac{E_0}{4} - (g_J + g_I)\mu_B B + \Delta E_3 \\
E_4 &= -\frac{E_0}{4} - \frac{E_0}{2}\sqrt{1 + \frac{(g_J - g_I)^2\mu_B^2 B^2}{E_0^2}} + \Delta E_4
\end{aligned} \tag{64}$$

Due to these extra terms, the triplet states are not degenerate at zero magnetic field and the GSHS does not have the same energy anymore. Figure 6 shows the potential antihydrogen splitting at zero magnetic field for the SME. The deviation possible in this model are given in units of energy. Therefore, they have an effect on an absolute scale. For this reason the measurement of the GSHS has an advantage over the 2S-1S transition. Since the energy difference between the first excited level and the ground state is much bigger than the energy difference between hyperfine structure transitions, it would be harder to detect an energy shift as described by the SME for the 2S-1S transition. Moreover, within the minimal SME (mSME) a CPT violation in the 2S-1S transition is not expected.

It is beyond the scope of this work to explain and derive where these extra energy terms come from (see [3, 4, 19, 20] for more detail). Nevertheless, it is important to note that these

extra terms imply that the hyperfine splitting of ground state hydrogen and antihydrogen could be different if certain CPT violation terms are found to have non vanishing coefficients.

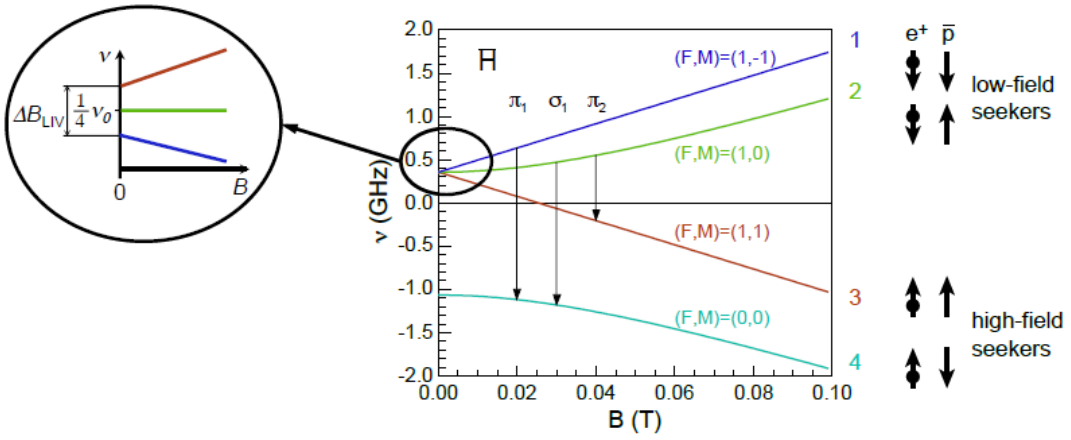

Figure 6: Antihydrogen ground state hyperfine splitting for CPT symmetry violation [21].

3 The ASACUSA hydrogen beam setup

The ASACUSA hydrogen beam has been set up for characterizing the rabi-like spectroscopy parts (e.g. the cavity and McKeehan coils) that are going to be used for the measurement of the antihydrogen hyperfine structure. The main components of the hydrogen beam are listed below:

- Atomic hydrogen source,
- Tunning fork chopper,
- Polarization sextupole magnets,
- Cavity,
- McKeehan-like coils,
- Shielding,
- Analysis sextupole magnets and
- Quadropole mass spectrometer (QMS).

Figure 7 and 8 show a photograph and a sketch of the beam line, respectively. The atomic hydrogen enters the beam line and first passes through the polarizing sextupole magnets. These magnets produce an inhomogeneous magnetic field. The four hydrogen ground states can be classified into low field seekers (LFS) and high field seekers (HFS). The LFS states are focused in the middle of the beam line while the HFS states will be bent towards the walls of the chamber. The beam is now polarized into a LFS only type beam. The polarizing sextupoles account for the magnet region A of figure 5. A cavity tuned to $\approx$ 1.4 GHz produces the required oscillating magnetic field and the McKeehan-like coils with shielding produces the static magnetic field. These two components make up the region C in figure 5. At the resonance frequency (either for σ_1 or the π_1 transition) one of the LFS states will change into the HFS state $|4\rangle$. The analysis sextupole magnets, which corresponds to the magnet section B of the figure 5, will then filter out the HFS by the spin flip. At resonance frequency the count rate at the detector will drop. The detector for the H-Beam setup is a quadrupole mass spectrometer.

3.1 Atomic hydrogen source

A Packhard 9100 hydrogen source supplies hydrogen gas to the beam lime via electrolysis. The molecular H_2 needs to be dissociated to create atomic hydrogen. The molecular hydrogen enters a pyrex cylindrical tube enclosed by a radio frequency antenna. A microwave generator set to an initial frequency of 2.45 GHz feeds the antenna through two coaxial connectors (See figure 9b). The typical power for igniting the plasma is 30 W, during the measurement the power is raised to 60 W. The frequency was then tuned to reduce the reflected power to a value between 1 and 8 W. Further information can be found in [9].

The pyrex tube is mounted perpendicular to the beam axis. The atomic hydrogen is transferred to the beam line by a 90° bent Teflon tube. This tube is surrounded by two aluminum plates (See figure 9a). These plates are connected to a cryocooler system which main components are a coldhead and a compressor. The Gifford-McMahon refrigeration cycle process will take place inside the coldhead to cool down the aluminum plates to the desired temperature.

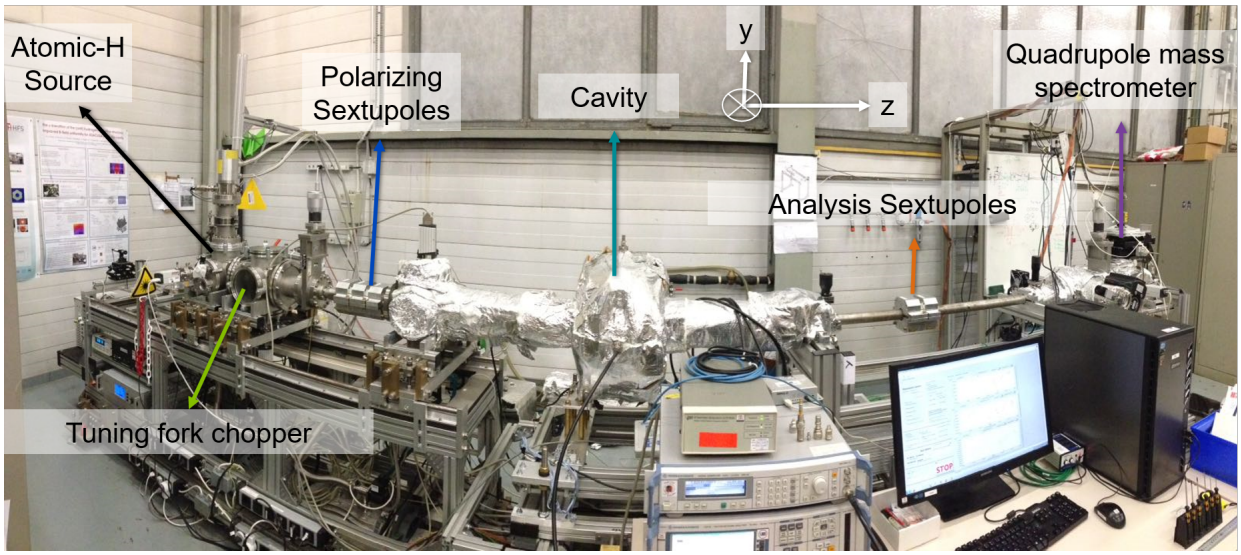

Figure 7: Hydrogen beam setup.

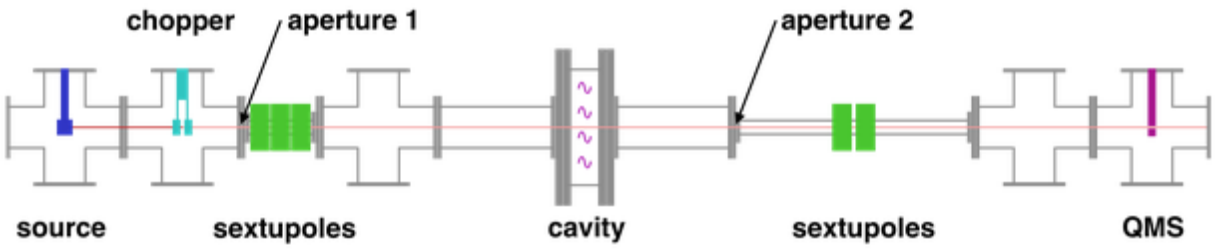

Figure 8: Schematic representation of the hydrogen beam [Made by Markus Wiesinger].

This cooling process has to be carried out, because the expected condition for the antihydrogen GSHS experiment is a beam of approximately 50 K and the hydrogen beam measurements have to be made under similar conditions. The nominal temperature of the Teflon tube was set to 20 K for the measurements.

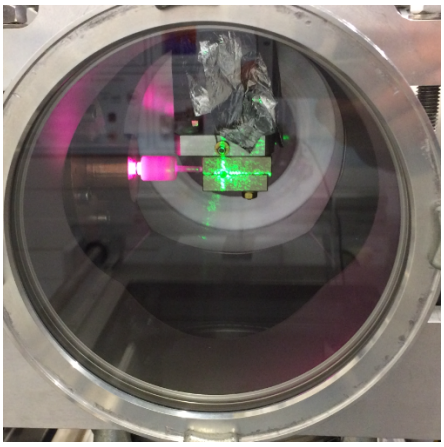

(a)

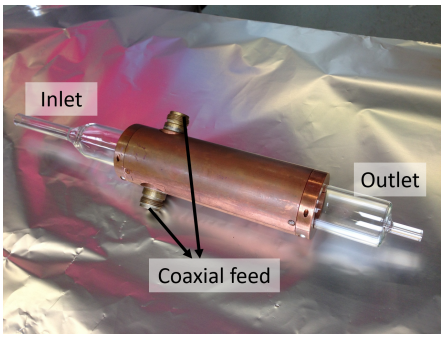

(b)

Figure 9: (a): Setup for the supply of atomic hydrogen to the beam line. (b): Pyrex tube encapsulated in a radio frequency antenna

After all these processes, a cold atomic hydrogen beam will enter the evacuated hydrogen beam line.

3.2 Tuning fork chopper

A Scitec CH-10 tunning fork chopper (see figure 10) with an oscillating frequency of $\approx$ 180 Hz and duty cycle of 50% will modulate the beam signal arriving at the detector. The advantages of such a chopper are the UHV capability, direct output of a reference signal for data acquisition and adjustable amplitude (by means of a manual turn knob). However, the frequency is fixed. The modulated signal produced by the chopper was used for the lock-in amplifier (LIA, see section 3.5).

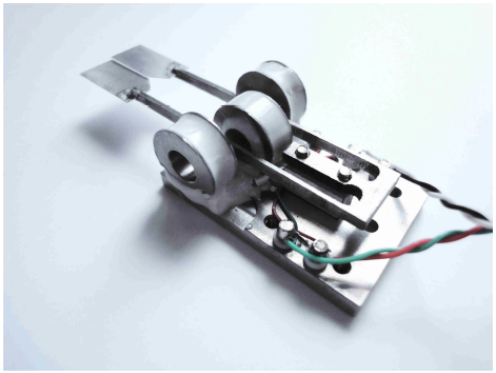

Figure 10: Tuning fork chopper

3.3 Sextupole magnets

The magnetic field gradients required in a Rabi experiment are now produced by a set of permanent magnets arranged in a Halbach-like configuration. They replace the superconducting sextupole magnet which is used for antihydrogen spectroscopy and was only available to the

hydrogen experiment during the last long shut down period at CERN. They also replace the polarizing sextupole doublet [22], as they were not suitable to provide a polarized beam for the σ and π transitions of comparable quality.

The SMI sextupole magnets were designed to replicate the characteristics of the ideal Halbach cylinder [23]. For this purpose, 12 cuboid magnets blocks of NdFeB material (15 mm x 15 mm x 50 mm) with uniform magnetization are arranged in a circular pattern. The 12 magnets are inserted into a 3D-printed holder and mounted onto the beam line using an aluminum enclosing (See figure 11). By placing five to six such assemblies in series a similar refocusing strength as for the super conducting magnet is achieved. The SMI sextupoles have a magnetic field gradient of about 1600 T m^{-2} and an integrated gradient of ≈ 84 Tm^{-1}. A full characterization and analysis of the SMI sextupole magnets can be found in [24, 25].

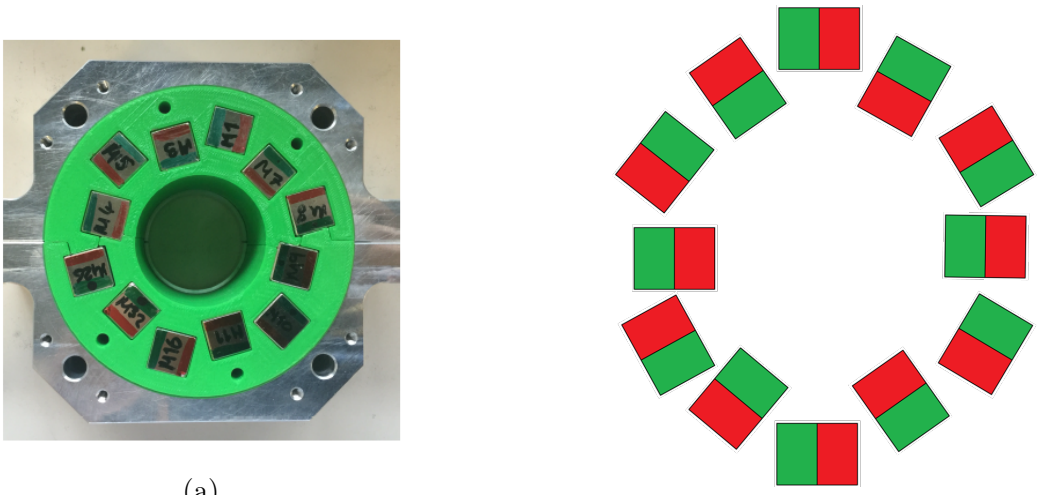

(a) (b)

Figure 11: (a): SMI sextupole magnet (b): Sextupole magnet configuration

3.4 Detector

A quadrupole mass spectrometer mounted perpendicular to the beam axis is used to detect the atomic hydrogen. The hydrogen enters the QMS apparatus through a 3 mm diameter hole (see figure 12a). There, hydrogen atoms and residual gas get ionized by collisions with electrons emitted from a filament. The ions are accelerated towards the oscillating quadrupole field of the spectrometer. Depending on the settings only ions of a certain mass-to-charge ratio can pass this section on stable trajectories. The settings are chosen to select mass 1 (protons p = hydrogen ions H^+). The selected particles are counted using a channeltron for efficient single particle detection. The pulses are amplified and converted to logic NIM signals using a LeCroy-LRS 333 and CAEN mode 84 NIM discriminator, respectively. A NIM-TTL converter (model LeCroy 668AL) adapts the signal for recording with a data acquisition card (National Instruments PCIe-6361). Afterwards the counts can be transfered to a personal computer where the counts will be discriminated on-line based on a digital LIA scheme.

3.5 Lock-in Amplifier (LIA)

To separate the signal from the background LIA is going to be used. Lock-in amplifiers are used, when small periodic signals within huge background noise have to be measured. Generally, lock-in-amplifiers use a periodic reference signal to map out signals with the same frequency from the input signal, while suppressing other signals with extremely narrow

bandwidths. This periodic signal can be expressed in a Fourier series. The lock-in-amplifier extract the amplitudes and phases of this Fourier series [26].

The tuning fork chopper modulates the beam signal arriving to the detector. One period of the chopper is divided and recorded in typically 200 phase bins. The counts, which are registered during the measurement in certain time bins are accumulated in the corresponding phase bin. This produces a histogram of counts versus phase bins.

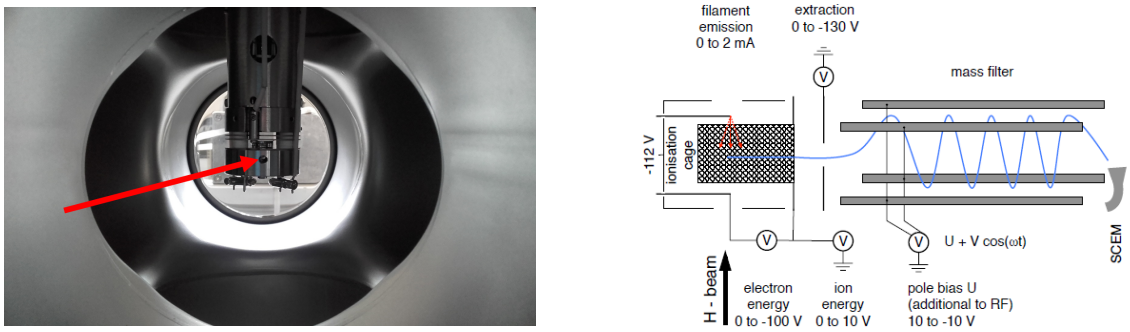

(a) (b)

Figure 12: (a): 3 mm diameter hole entrance to the detector apparatus (b): Schematic representation of the detector apparatus [27].

From such a histogram the background signal and the beam rate can be found. At some chopper phases the chopper blades will be closed. At those phases with a delay matching the typical time-of-flight (ToF) from the chopper to the detector, no particle should be detected. Moreover, using a laser signal the time of flight of the beam particle between the chopper and the QMS can be calculated using the phase difference between the beam signal and the laser signal. This is necessary as the phase of the monitor signal is offset from the chopper phase by an amplitude-dependent value.

The measured counts during the time the blades are closed corresponds to the residual gas in the detector chamber. Hence, this constant value is known as the background signal. At the phase bins where the blades let the beam particle go through, the measured counts will be the addition of the background signal plus the beam signal (known as the beam rate).

Even though the total amount of counts (signal) is going to decrease by introducing the chopper, the signal to noise ratio will become significantly better (see figure 13).

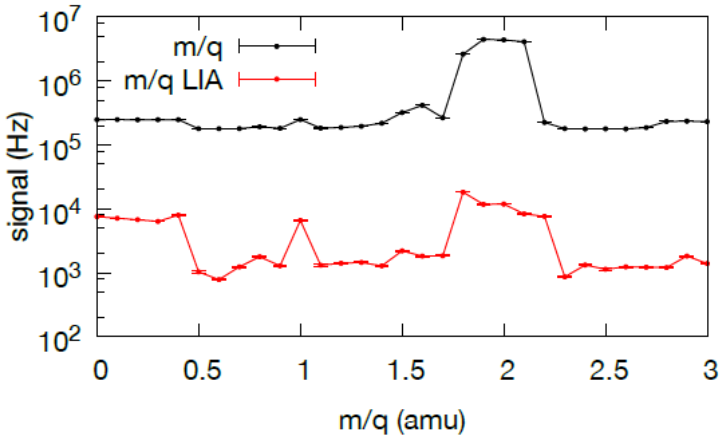

Figure 13: Number of counts for different atomic masses. The black line show the results without the LIA and the red line the results with LIA. The peak at 1 amu is more prominent with the LIA. Taken from [9].

3.6 Ring aperture and beam trajectory

The equation of motion for the trajectories of the four hydrogen ground states through the field gradients along the beamline were derived and numerically solved in [24]. Figure 14 shows the relative acceleration in radial direction for state $|1\rangle$ and $|2\rangle$ as experienced in the SMI permanent sextupole magnets. From this figure, it can be concluded that states $|1\rangle$ and $|2\rangle$ will follow a different trajectory throughout the sextupoles for a small radius. This implies that depending on the position of the analysis sextupoles (see figure 8), the states will not arrive with equal intensity at the detector. This would be counterproductive for the anticipated measurements using both transitions, as the count rate drop would be significantly bigger for one of the transitions. This was experimentally verified in [24].

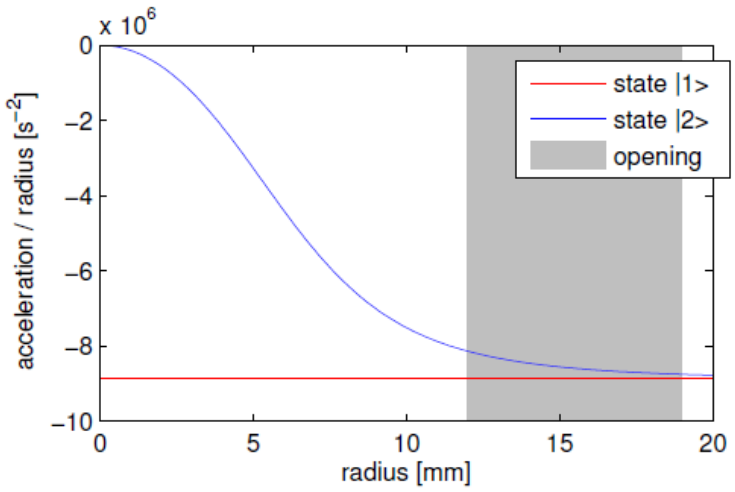

Figure 14: Relative acceleration in radial direction as produced by the SMI sextupole field. The gray area represents the opening of the ring aperture. Taken from [24]

.

To solve this problem, ring apertures constructed at the SMI workshop were introduced into the beam line (see figure 15) after the chopper chamber and at the CF100 to CF40 adapter (see figure 8). The ring apertures will select atoms following a trajectory by a defined radius and will block the central component (radius = 0 mm) of the beam. The openings of the ring apertures let atoms at radii between 12 and 18 mm go through (gray area in figure 14). Within this area, both states will follow a similar path and will arrive with a similar intensity at the detector.

Finally, a trajectory simulation program was developed and implemented by Markus Wiesinger [24] to test the effects of the ring apertures and the SMI constructed sextupole magnets on the beam trajectory. Figure 16 shows the simulated trajectories for the four hydrogen ground states in the described hydrogen beam setup.

3.7 Cavity

The cavity produces the oscillating magnetic field required for the spin flip (see sections 2.3 and 2.4). This cavity is going to be used in the antihydrogen experiment. Its characterization is essential to reach the desired goal of measuring the antihydrogen hyperfine structure. The cavity was designed and developed by Silke Federmann [28]. The most important condition the cavity has to fulfill is the production of a trajectory independent oscillating magnetic field in the x-y plane (plane perpendicular to the beam axis) across the large open diameter of 100 mm. As a consequence the amplitude of the oscillating field cannot be constant along the z-direction (i.e, beam propagation direction).

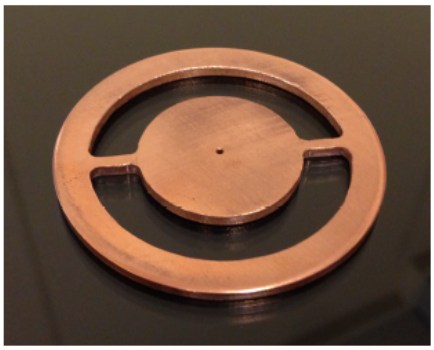

(a)

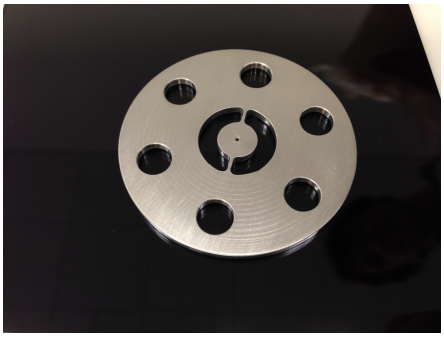

(b)

Figure 15: (a): Ring aperture with outer and inner diameter of, 38 mm and 23 mm respectively (b): Ring aperture with an outer and inner diameter of, 20 mm and 12 mm respectively

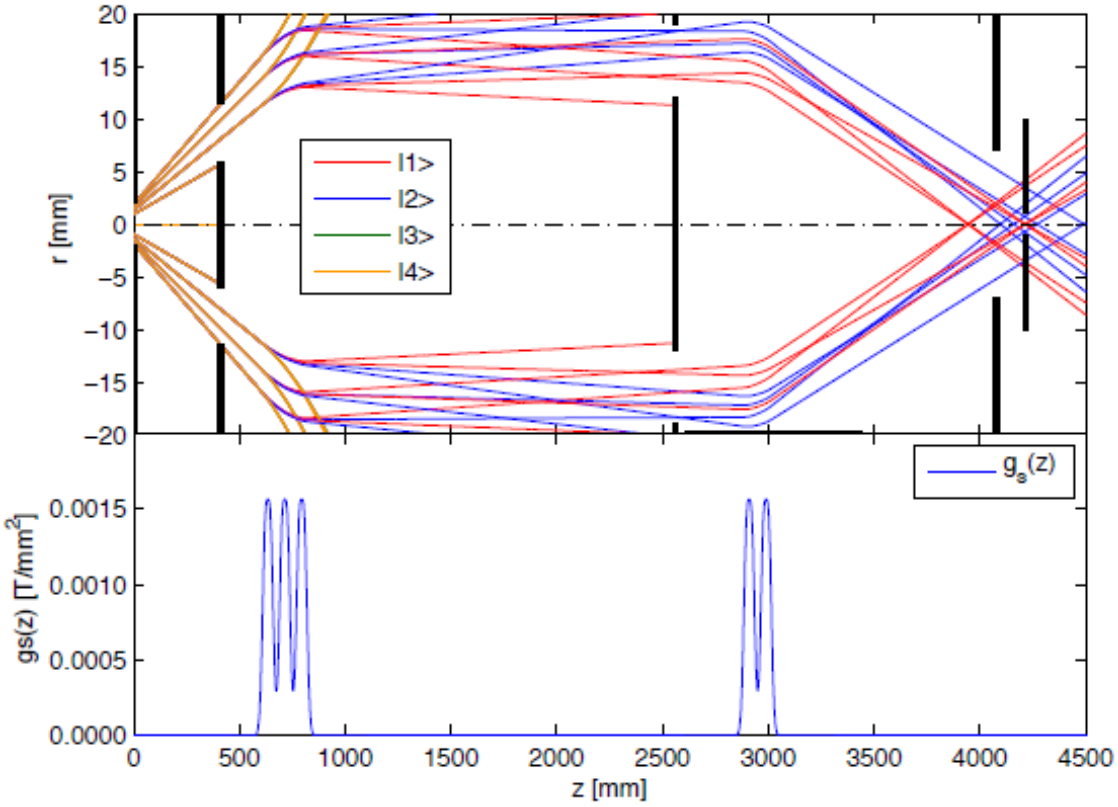

Figure 16: Upper part of the graph is the simulated trajectories of the four hydrogen ground states. The first three vertical black lines at z = 410 mm represent the first ring aperture. The ones at z = 2560 represent the second ring aperture. The detector 3 mm aperture is represented by the last two black lines. The lower part shows the sextupole strength $gs(z)$ against the position of the SMI sextupole magnet. Taken from [24]

.

Based on this premise, a strip-line geometry was selected for the cavity (see figure 17). The second condition is to set the radio frequency field resonantly amplified by the cavity at the hydrogen ground state hyperfine structure resonance frequency. This leads to the dimensions of $\sim \lambda_{\mathrm{HF}}/2 \approx 105.5$ mm for the cavity thickness and the strip line spacing. The spring contacts rather ensure good electrical contact between the main body and the lids of the cavity. Since the cavity aperture is quite large, meshes were implemented at the

entrance and exit aperture of the cavity to confine the microwaves. The mesh-mesh distance was used to tune the radio frequency to the desired frequency. In addition small metal disks (see figure 17a) were also used for tuning. Further information on the tuning process can be found in [28].

A Rohde & Schwarz SLM02 signal generator produces the microwaves at the desired frequency and power. This signal will be amplified by a 1189 - BBM3K5KKO with an amplification factor of 42 dB. A stub tuner is used to fine tune the first resonance peak to the right frequency (see chapter 5). The microwaves are introduced into the cavity via an antenna and the stub tuner is used to optimize the coupling. A second antenna picks up the signal and is connected to a ZVB20 vector network analyzer (VNA). The VNA will work in this setup as a spectrum analyzer to measure the power. The remaining two antennas are terminated with a 50 Ω resistance. Both the VNA and the signal generator are locked to a rubidium standard, which is stabilized by the timing signal of the Global Positioning System (GPS).

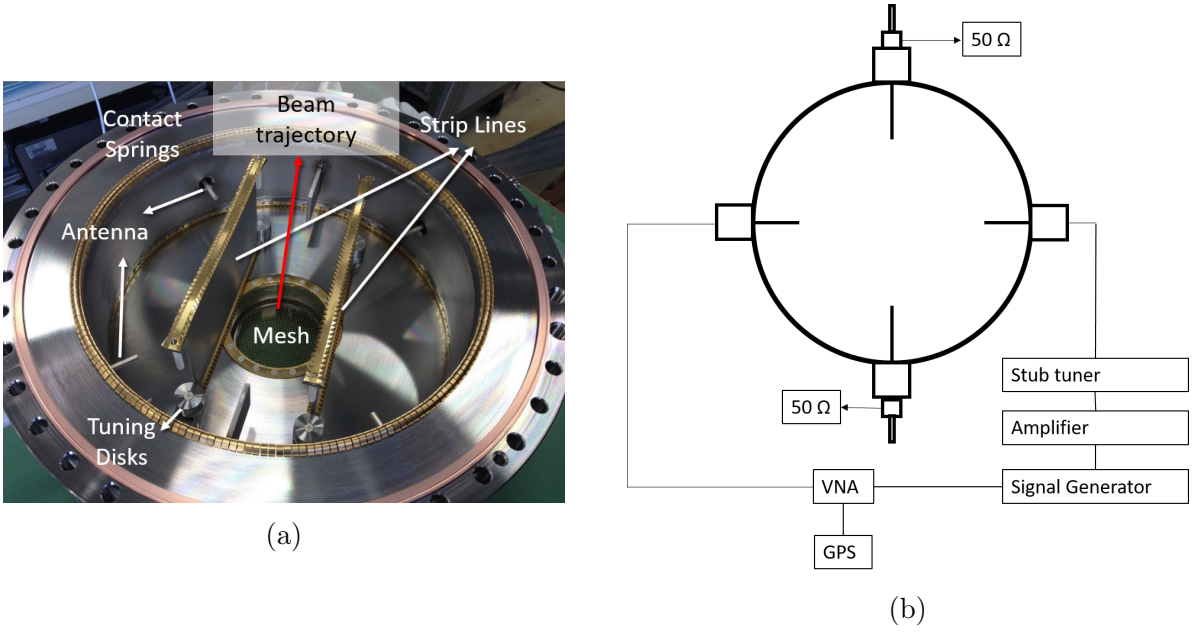

(a) (b)

Figure 17: (a): Strip-line geometry cavity (b): Schematic representation of microwave excitation apparatus.

Finally, simulations were carried out by C. Sauerzopf to show the effects of the strip-line geometry on the transition probabilities. The simulations were done by numerically solving the optical Bloch equation [29]. Figure 18 shows the results. It can be seen that at the resonance frequency the initial state population density will be restored when the beam leaves the cavity due to the change of sign in the B field. On the other hand, at a small detuned frequency the state population density change will reach a maximum. Due to the strip-line geometry two fringes are expected at the detuned frequency instead of just one at the resonance frequency.

To drive the spin flips a static magnetic field is needed. This magnetic field has to be generated inside the cavity region. The McKeehan-like coils are going to produce this static magnetic field which needs a shielding from external magnetic field sources. The characterization of these two components presents a major part of this thesis and is going to be discussed on the following chapter.

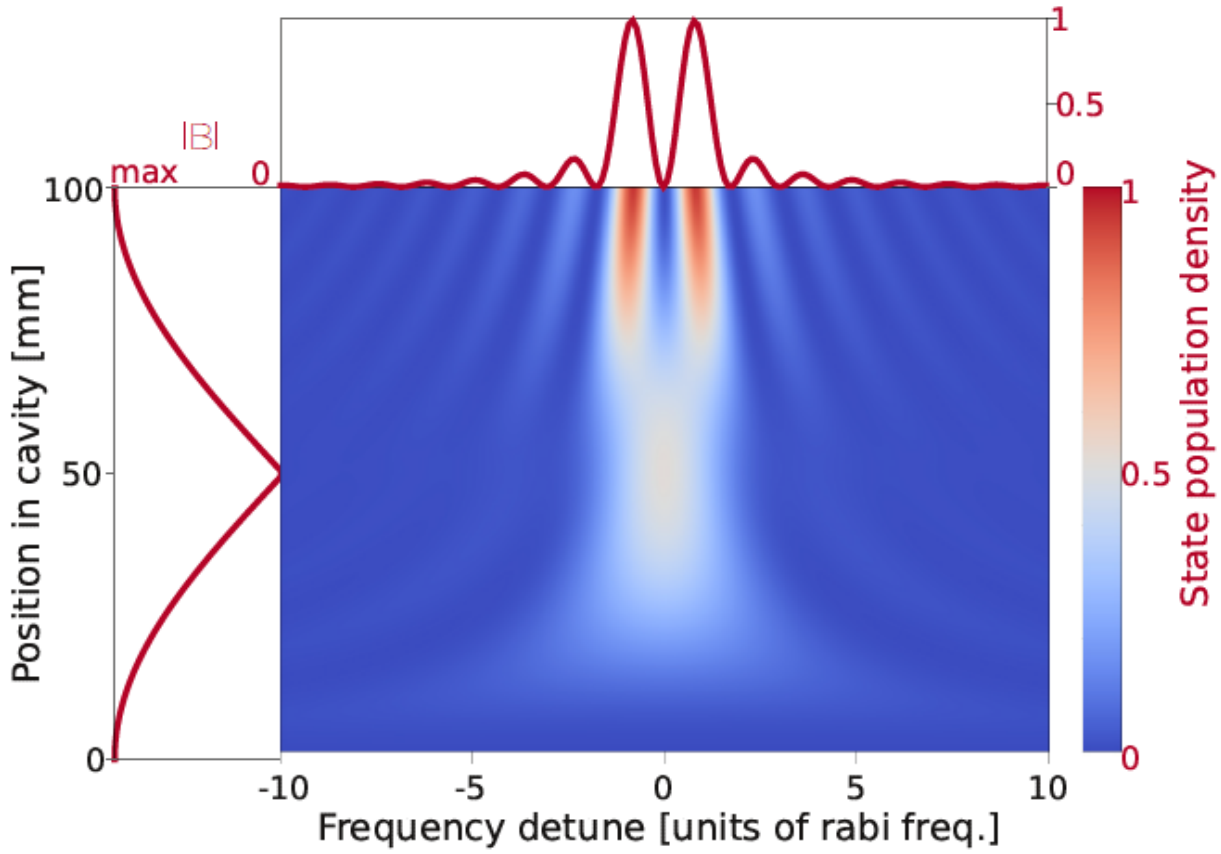

Figure 18: Simulated development of the state population density withing the cavity. The plot on the top is a projection of the spin flip probability when leaving the cavity. The plot on the left side shows the dependency of the value of the norm of B in the z direction. The simulations applied to a mono-energetic beam and a power adjusted to drive the π_1-transition. Taken from [29]

.

4 Characterization of the static magnetic field produced by the McKeehan-like coils

The static magnetic field is responsible for producing a splitting of all 4 hydrogen ground states (see section 2.2.2). Figure 19 shows the energy shift of the σ_1 and π_1 transitions at the low magnetic field regime. A fluctuation of the static magnetic field will have a small effect on the energy of the σ_1-transition. On the other hand, a fluctuation will have a considerable effect on the energy shift of the π_1-transition. A magnetic field inhomogeneity translates into a frequency broadening or a frequency shift. If the static magnetic field is not homogeneous enough, the broadening will dissolve the resonance structure or will shift the transition frequency and distort the results.

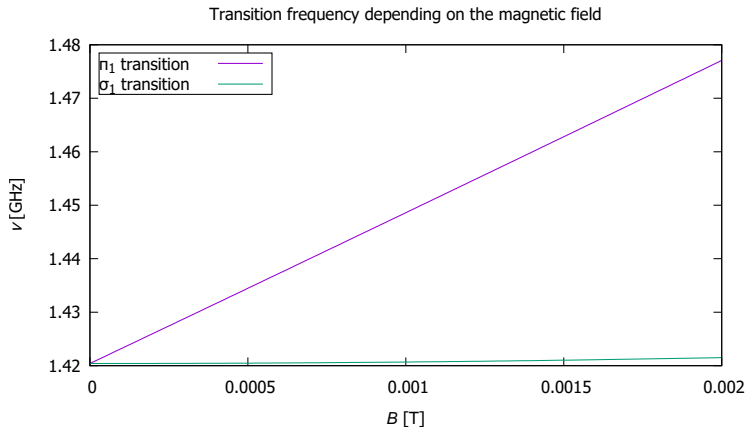

Figure 19: Energy shift for the σ_1 and π_1 transitions at a low B-field regime

Therefore, it is important to set a limit to the magnetic field inhomogeneity. The shift on the π_1-transition can be approximated by:

$$\Delta\nu = \frac{\partial\nu}{\partial B} \cdot \Delta B \approx \frac{\mu_B}{h} \cdot \Delta B \approx 1.4 \frac{\text{MHz}}{\text{Gauss}} \cdot \Delta B \tag{65}$$

where ν is given by equation (33).

For the double peak structure as obtained due to the characteristics of the strip-line cavity a reasonable limit is, that the two peaks shall remain resolved. Figure 20 shows the spin flip probability as a function of a Gaussian broadening of the resonance and the detuning frequencies. From this figure, it can be estimated that for a value of $\approx 1.3\ \Omega_{\text{Rabi}}$ the double peak structure will not be resolved. The Ω_{Rabi} would correspond to a frequency of ≈ 7 kHz for the interaction time of the present setup. This sets the limit for the $\Delta\nu$ at ≈ 10 kHz. Using this value and equation (65) yields the upper limit for the magnetic field inhomogeneity. For a magnetic field of 10 Gauss the relative homogeneity of the required magnetic field corresponds to:

$$\frac{\Delta B}{B} \approx 0.1\% \tag{66}$$

To achieve a relative homogeneity of 1000 parts per million (ppm), a McKeehan-like coils configuration is going to be used, as the Helmholtz coils provide a field of merely 5% homogeneity over the cavity volume with the same size of coils.

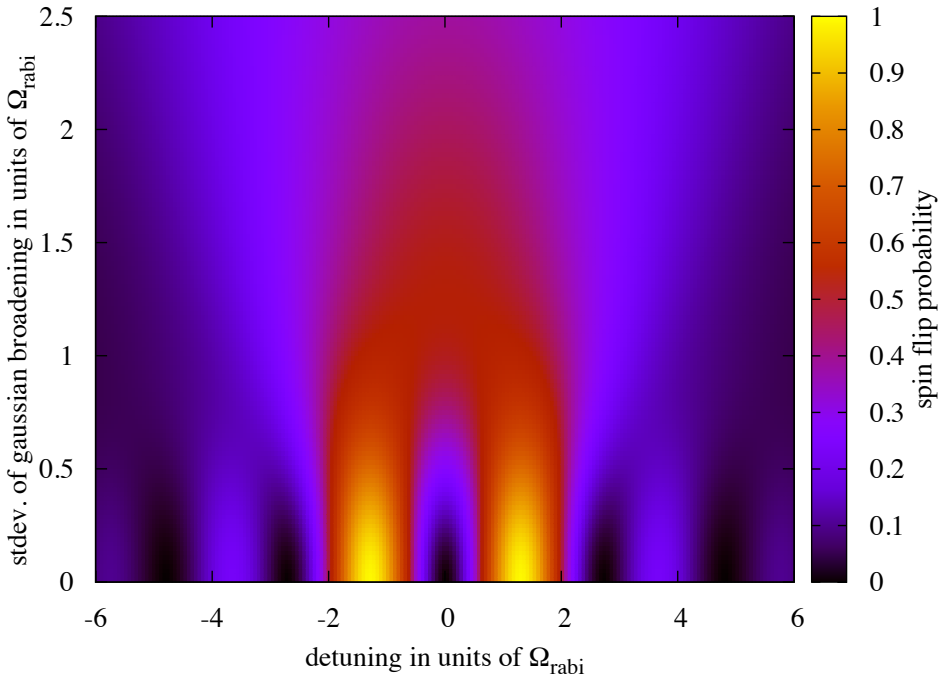

Figure 20: Spin flip probability for various extents of a Gaussian broadening of the resonance and line shape. The x-axis gives the detuning and the y-axis the standard deviation of the Gauss broadening. Both in units of Ω_{Rabi} (Made by Martin C Simon).

4.1 McKeehan coils configuration

The idea of producing a homogeneous static magnetic field using coils comes from the analysis of the magnetic field produced by an electrical current in a circular loop. The loop produces a nearly homogeneous axial magnetic field at its center. However, the inhomogeneity increases proportionally to the squared distance from the center. To produce a homogeneous magnetic field of a few centimeters at the center a large loop radius is needed, which is disadvantageous in view of the given space constrains. This problem can be solved by combining two or more loops.

The magnetic field intensity near the origin due to a combination loops can be derived from the following potential [30]:

$$\mathrm{V}_p = \frac{2\pi i_p}{c}\Bigg\{ \sum i_p + \sum i_p u_p \sum_{n=1}^{n=\infty} \frac{1}{n} \sum_p [i_p(1-u_p^2) r_p^{-n} P_n'(u_p)] r^n P_n(u) \Bigg\} \tag{67}$$

where i_p is the current in the pth loop, r_p and $u_p = \cos(\theta)$ determine the geometry of the loop (see figure 21). $P(u)$ is the nth surface zonal harmonic of the argument u (the explicit definition for $P(u)$ and its first derivative as well as their values up to n= 12 can be found in Appendix 6).

Furthermore, it is convenient to define the quantity S_n:

$$S_n = \frac{1}{n} \sum_p [i_p(1-u_p^2) r_p^{-n} P_n'(u_p)] \tag{68}$$

A simple calculation shows that for a single loop with $u_1 = 0$ and $V_p = V_1$, no n = even terms appear in V_p. For n = 1, the value of S_n is 1 and V_1 takes the following form:

$$V_1 = \frac{2\pi i_1}{c}(1+u) \tag{69}$$

This term corresponds to the constant term when calculating the magnetic field. Higher odd orders of n will contribute as corrections to the B-field. The ideal homogeneous static magnetic field will not have these corrections and would be just a constant. The idea behind the coil configuration is to make the correction terms vanish. In other words, looking for the solution of the following equations:

$$\begin{aligned}
\sum_p [i_p(1-u_p^2)r_p^{-3}P_3'(u_p)] &= 0 \\
\sum_p [i_p(1-u_p^2)r_p^{-5}P_5'(u_p)] &= 0 \\
\sum_p [i_p(1-u_p^2)r_p^{-7}P_7'(u_p)] &= 0 \\
&\vdots
\end{aligned} \tag{70}$$

For example, for two symmetrical placed coils with $i_2 = i_1$, $r_1 = r_2$, $u_2 = -u_1 = 5^{-\frac{1}{2}}$ and $V = V_1 + V_2$, the n = 3 correction would be equal to zero [30]. The field is uniform to the forth order correction. This two-coil configuration is known as Helmholtz coils. Complete solutions of equation (70) were calculated for 4, 6 and partially for 8 loops by Neumann and Fanselau [31,32] assuming the same r_p for all loops. The McKeehan configuration is a 4 loop configuration and allows for an 8th order compensation at the center.

The previous measurement of the hyperfine splitting with the ASACUSA H-beam was conducted using Helmholtz coils [9]. The newly constructed McKeehan-like coil assembly now provides a better static magnetic field enabling better experimental conditions for the measurement of the π_1-transition. Even though equation (70) can be solved analytically, at SMI the values for r and u were found by doing simulations because the theory assumes several ideal conditions, which are not satisfied within this experiment. For instance, the need of a shielding, the cavity body (=magnetic material within coil volume), larger finite region has to be homogeneous (not only the center) are not taken into consideration in the theory.

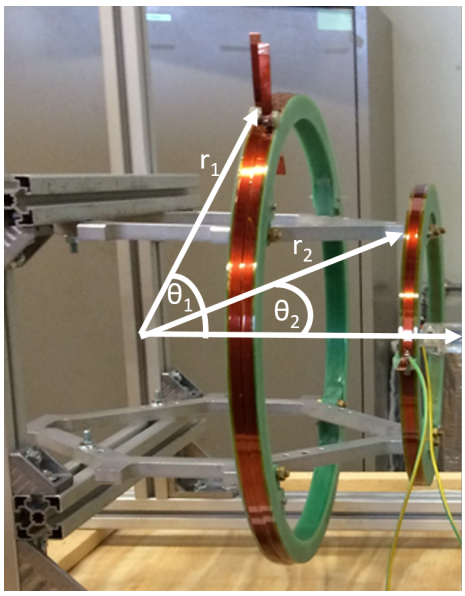

Figure 21: Standard coordinate system for the McKeehan-like loop combination.

4.2 Simulations of the shielding and the McKeehan-like coils

All the simulations presented in this section were done with COMSOL Multiphysics® Modeling Software.

4.2.1 Shielding

The importance of the homogeneity of the magnetic field was discussed in the previous sections. It is desired that the only static magnetic field produced inside the cavity comes from the McKeehan-like coils. Static magnetic fields from other sources (e.g. the earth magnetic field and neighboring trap magnets) will increase the inhomogeneity of the magnetic field inside the cavity region. Therefore, these magnetic fields have to be shielded.

The parameter defining the effectiveness of a shielding is the shielding factor. This is simply given by the ratio of the remaining field with shielding (B^s) over the hypothetical field without shielding (B^0):

$$\mathrm{SF} = \frac{1}{N}\sum_{i=0}^{N}\frac{|B_i^s|}{|B_i^0|} \tag{71}$$

The simulations calculate the magnetic field inside the cavity for the geometry with and without shielding. Inserting these values into equation (71), one can calculate the best geometry and material to use for the shielding. It turned out that a three layer cylindrical shielding will be sufficient to shield the external magnetic sources presented in the hydrogen and antihydrogen experiment [33]. Once the shielding geometry was chosen, the gap between the layers was optimized. Figures 22a and 22b show, respectively the geometry of the simulated shielding and the values of the shielding factor for different gap length.

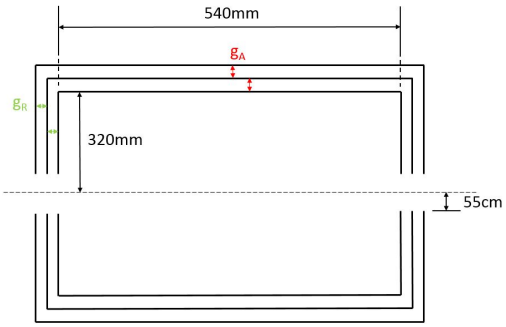

(a)

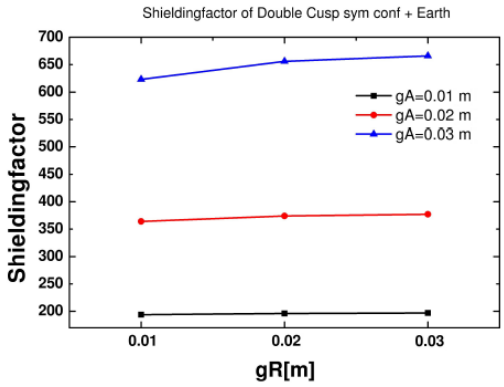

(b)

Figure 22: (a): Shielding geometry (rotationally symmetric along the dotted line) (b): Shielding factor for different gaps (Taken from [33]).

Finally, figure 23 shows the behavior of the absolute magnetic field value inside and outside of the shielding. This shielding is going to be used in the future for the antihydrogen experiment, the antihydrogen production will take place in a CUSP trap [34]. The CUSP will present another external magnetic field source that has to be shielded. All the simulation took into account this field and the earth magnetic field. For the hydrogen experiment this field is not present. Nevertheless, the behavior in figure 23 will be similar to just the earth magnetic field. Figure 23 shows that in the cavity region ($-0.15 < z < 0.15$) the magnetic field produced by the CUSP field and earth magnetic field is almost zero.

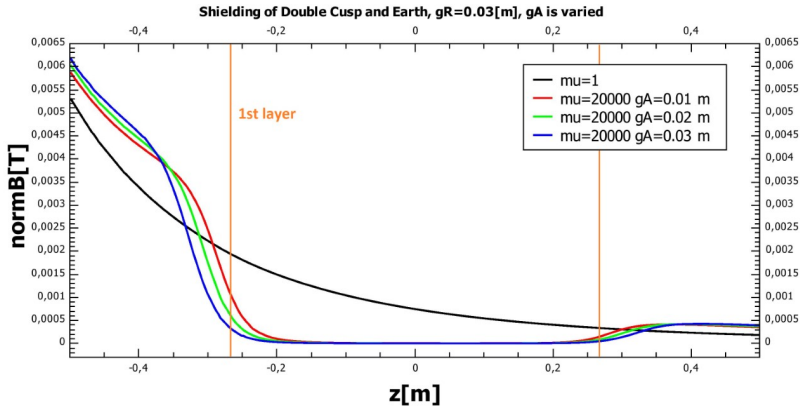

Figure 23: Behavior of the magnetic field inside and outside the shielding. The x axis represent the distance from the center of the cavity (Taken from [33]).

4.2.2 McKeehan-like coils

Now that the shielding geometry is settled, the next step is to find a coil configuration that produces the required homogeneity. The main parameters to optimize are the position of the coils (i.e radius, angle (see figure 21)) and the ratio of the currents of the coils ($i_2/i_1 = N_2/N_1$, assumed each turn carries the same current). The optimization procedure is straight forward. First, the radius of the McKeehan sphere is selected, then the angles θ_1 and θ_2. Afterwards, the current ratio is optimized using a script that calculates all the possible two coil combinations. The sphere radius is then varied for the best coil combination and the process is repeated several times until the parameters converge. Table 2 compares the final simulated values with the theoretical ideal values:

Table 2: Comparison of the theoretical and simulated values for the McKeehan configuration.

	Simulations		Theory	
	McKeehan-like coils		McKeehan coils	
	Large	Small	Large	Small
r	267 mm	279 mm		
θ	71.2°	34.4°	73.4°	40.1°
Turns	38	23	22	15
Turn ratio	1.65		1.46	

The theoretical calculations assumes that the radius (see figure 21) is the same for both coils (McKeehan).

For the McKeehan like configuration, the simulated relative magnetic field homogeneity for a magnetic field of ≈ 24 Gauss is:

$$\frac{\text{stdev}(|B|)}{\text{mean}|B|} = \frac{\sigma_{|B|}}{|B|} = 108 \text{ ppm} \tag{72}$$

This value is 10 times smaller than the required value given in equation (66). Following these specifications, the McKeehan-like coils were built at the CERN machine shops. Nevertheless, a small, unexpected problem occurred during the manufacturing process. The coils were made with 22 and 36 turns as the size of the mandrels could not house all turns because the additional layer thickness of the strip-wire insulation was not taken into account. As a result, the magnetic field was simulated again for the new number of turns to see the effect of less turns on the homogeneity. Figures 24 and 25 shows the results of the simulations.

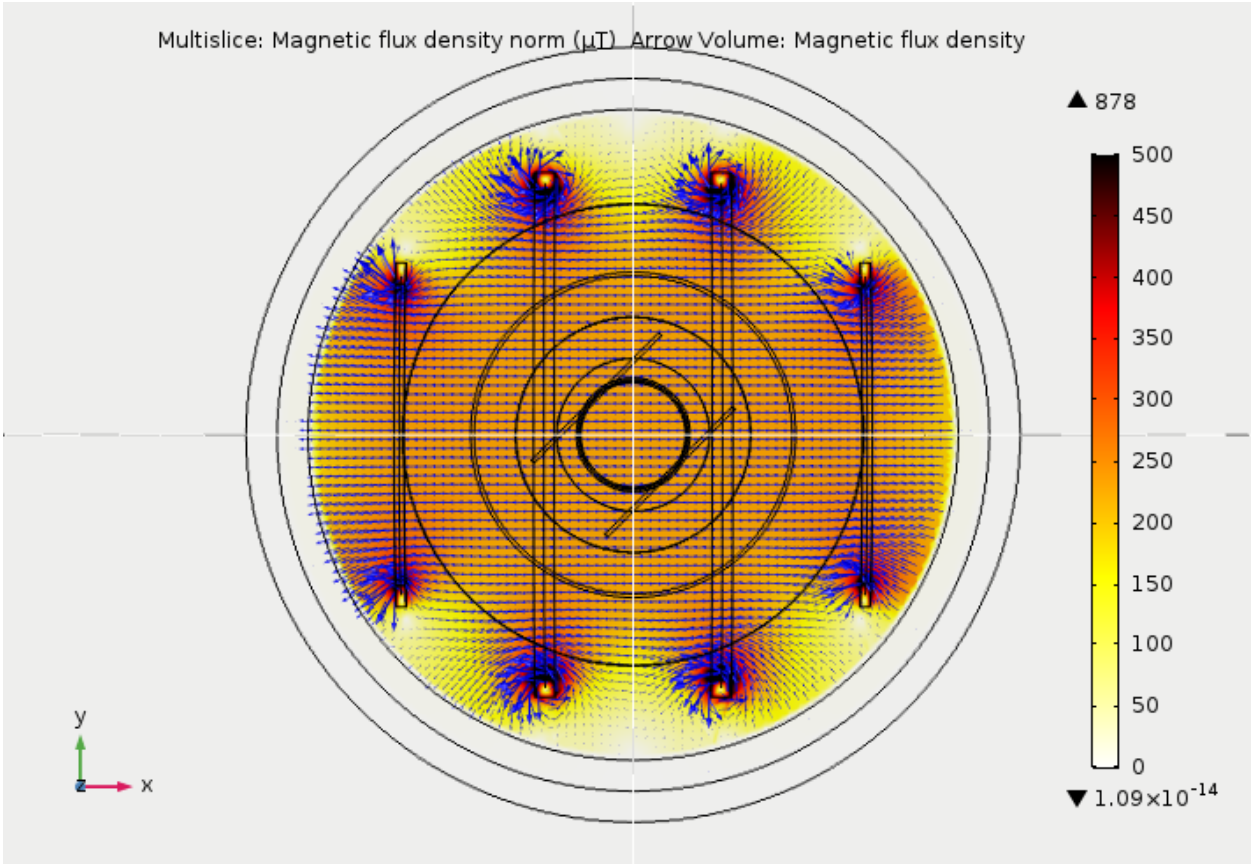

Figure 24: Magnetic field lines produced by the McKeehan-like coils for 1 A viewed along the z axis. Simulation made by Martin C. Simon.

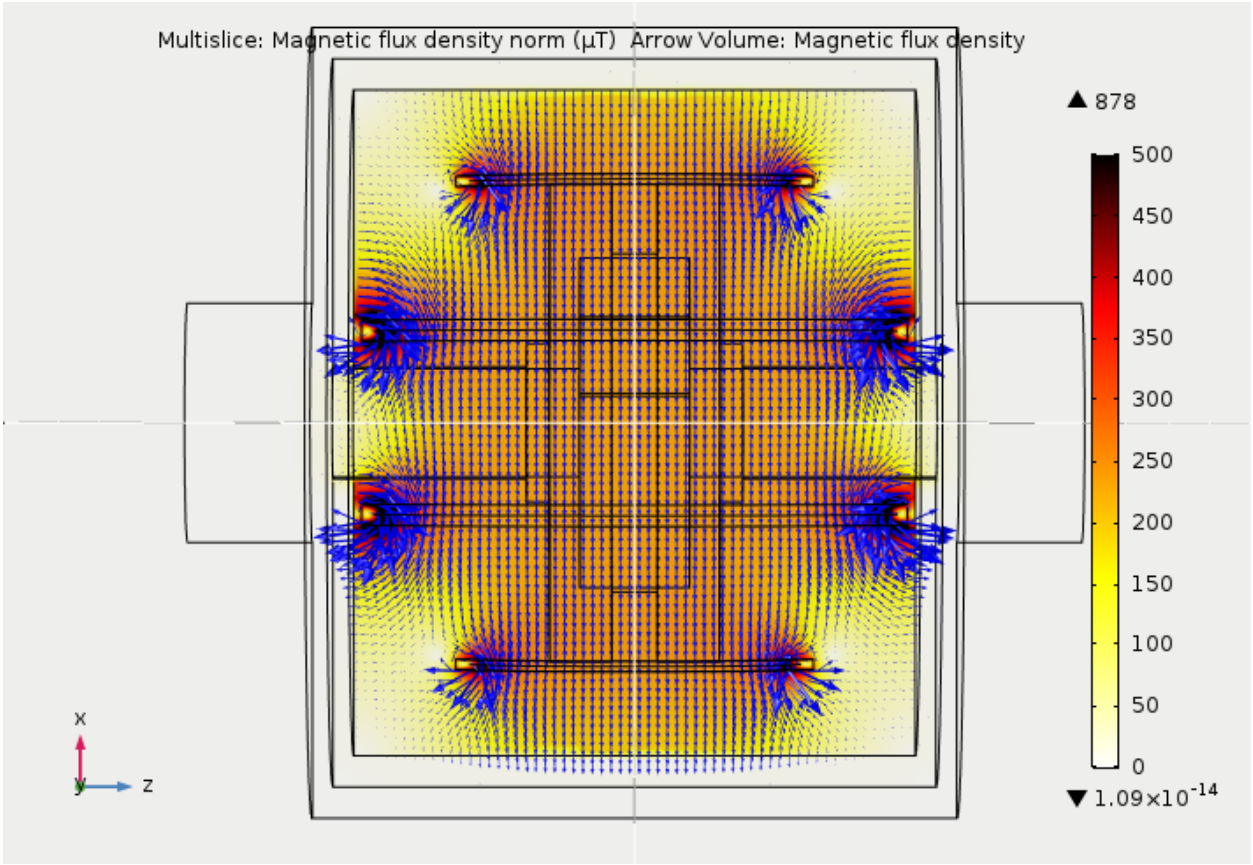

Figure 25: Magnetic field lines produced by the McKeehan-like coils for 1 A viewed along the y axis. Simulation made by Martin C. Simon.

From these figures, it can be seen that the coils will produce a static magnetic field perpendicular to the beam axis. At this point, it is important to notice the positions of the strip lines (two diagonal lines in the center of figure 24). They were mounted at 45° degrees with respect to the beam axis. The oscillating magnetic field will have a component perpendicular to the static magnetic field (needed for the π_1-transition) and one component parallel to it (needed for the σ_1-transition). From figure 25 the shielding structure can be appreciated, one sees the three layers as well as how the magnetic field it kept inside the shielding.

Using the simulated magnetic field values the homogeneity can be calculated. Figure 26 shows the results for 6 different μ values of the cavity (stainless steel) and different coil positions both relative to the optimal position.. The coils have the possibility to be moved $\pm$ 2 mm from the simulated position as it will be done in the characterization described in the next sections. The x-axis gives the position of the big coils and the y-axis the position of the small coils. The right hand side bar gives the homogeneity in ppm. The center of the plot indicates the optimal position given in table 2. From the optimal position the simulations moved the position of the coils in $\pm$ 2 mm. The simulations show that the maximal homogeneity achieved with this setup is theoretically $\approx$ 200 ppm.

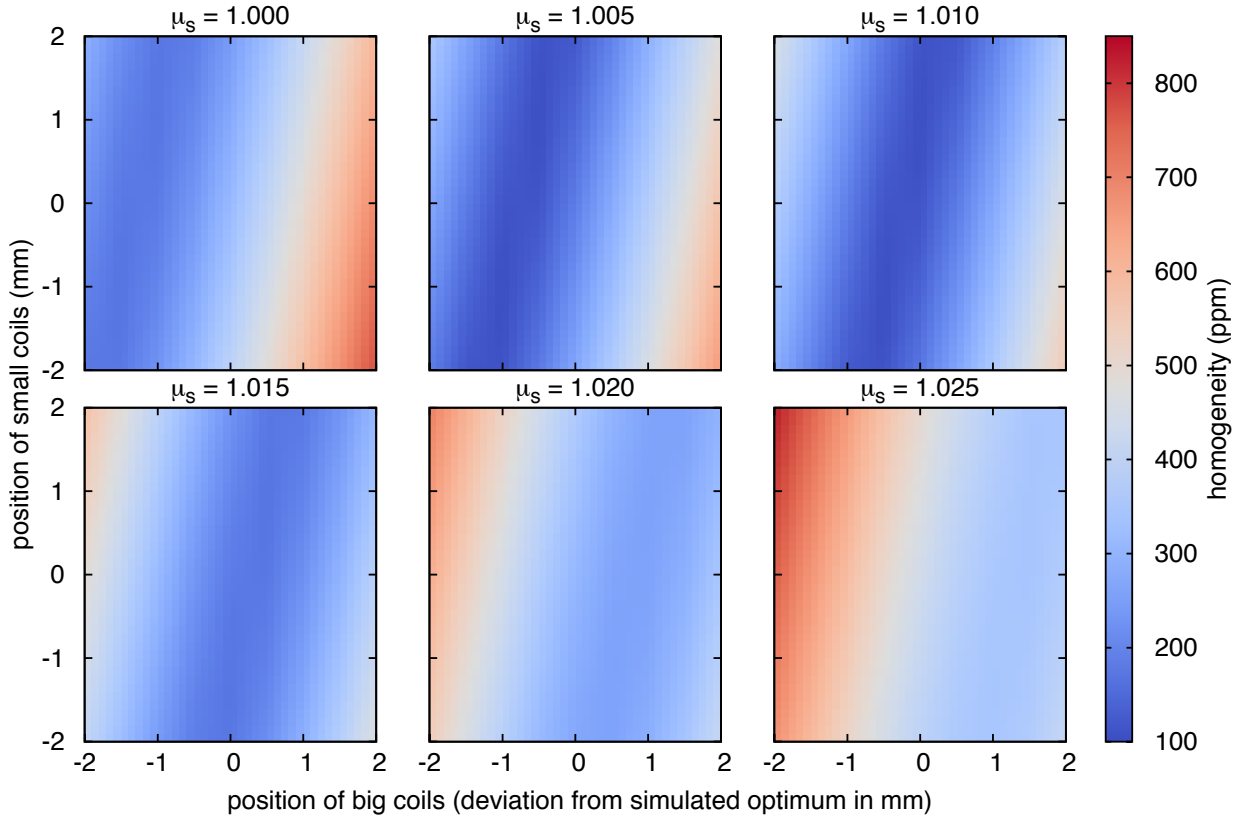

Figure 26: Simulated homogeneity values for different relative permeability values and different positions. Done for the number of turns and coil radii as built. Made by Martin C. Simon

The final step after simulation and production of the new McKeehan-like coils and shielding was the field characterization and then to assemble them into the beam line. Figure 27a shows the coils when they are mounted around the cavity, while figure 27b shows the shielding when it is closed.

4.3 Measurement of the static magnetic field produced by the McKeehan-like coils

The simulations were done under ideal conditions which are impossible to reproduce in the laboratory. For that reason, it is important to measure the actual value of the relative homogeneity and see how much it deviates from the ideal value. Moreover, the mount for the coils allows for the adjustment of the position in direction of the produced field by ±2 mm around the ideal value. The main goal of this measurement is to determine the actual homogeneity and optimize the position of the coils.

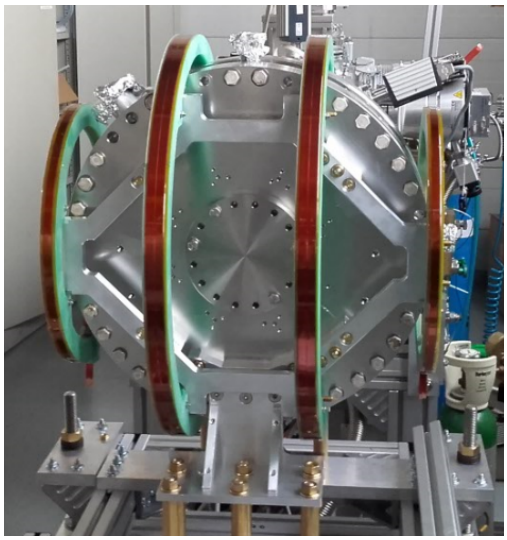

(a)

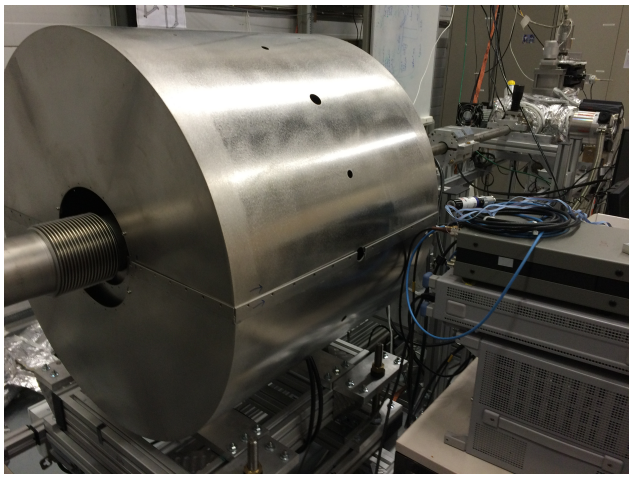

(b)

Figure 27: (a) Final assembly of the McKeehan-like coils (b) Final assembly of the shielding

In addition to the beam pipes, meshes block the entrance and exit of the cavity (see figure 7) and it is not possible to make the measurements directly at the beam line as the volume of interest is not accessible. For that reason, a small frame was built onto which the cavity and shielding were mounted. Figure 28 shows a picture of the setup for the magnetic field measurement. The main components of this setup are:

- Cavity,
- McKeehan-like coils,
- Shielding,
- Heizinger PTNhp 32-10 power supplier,
- Keithley 2001 multimeter,
- 3 M-404 precision translation stage [35],
- Mag-03 three-axis fluxgate magnetic field sensors [36] and
- PT 100 temperature sensor.

The magnetic field was measured using fluxgates. The fluxgates were inserted into a sensor holder (see figures 28 and 29a). The holder was then connected into a rotational disk (see figure 29b) which at the same time was screwed into the precision translation stage. The

rotational disk is used to make measurements at 0° and 180°, which gives an opportunity to correct for sensor offsets, as described blow. The translation stage is controlled by a computer using a Labview program. This allowed the sensors to scan and measure the magnetic field in the desired cavity volume.

Ideally, the complete cavity volume of interest is mapped, but there were some constraints. The first one is that the holder cannot be bent. The maximal measurable volume is the cylindrical volume between the two cavity openings.

The second constraint is the placement of the sensors in the sensor holder's head. For a given sensor holder head positions, the three sensors for the three axis measure the field at slightly different locations. Consequently, in order to calculate the $|B|$ correctly B_x, B_y, B_z measured with different sensor head's position have to be used. Inversely, the position of B_x, B_y, B_z as measured at a certain sensor head's position have to be corrected. The origin was chosen such that the three sensors are located at the positions given in table 3.

Table 3: Sensor Position

Sensor	Position 0° [mm]	Position 180° [mm]
X	(0,-5,5)	(0,5,5)
Y	(5,0,-5)	(-5,0,-5)
Z	(-5,5,0)	(5,-5,0)

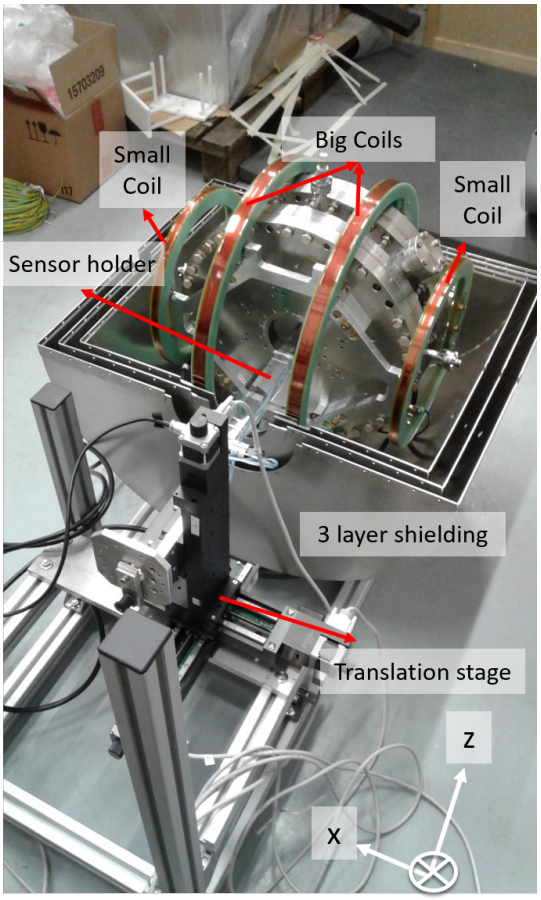

(a)

(b)

Figure 28: Setup for the magnetic field measurement. The shielding was closed during the measurement. (a): Shielding, Coils, sensor holder, translation stage (b): High precision current supply, Keithley multimeter, sensor read out apparatus and temperature read out apparatus.

The software of the translation stage can not recognize this offset, it just gives the actual position of the stage. Nonetheless, a script can be written to make the stage move. This script was written using the origin as a guideline. The offset of the sensors will constrain the total amount of measurable points inside the volume. While measuring the volume one has to take into consideration that the three sensors are shifted. The step size has to be chosen in such a way that the actual position mapped by the 3 sensors coincide over a volume as large as possible.

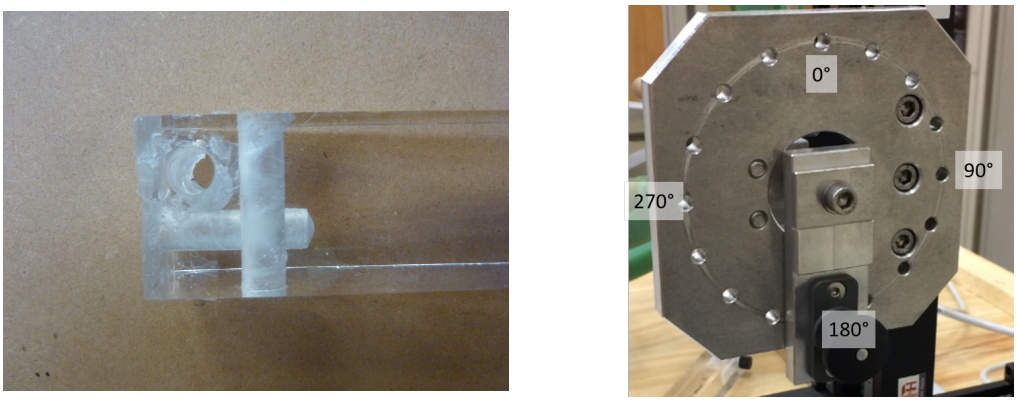

(a) (b)

Figure 29: (a): Sensor holder's head (b): Rotational disk

Further constraints were the shape of the cavity aperture and the sensor holder. The squared shape of the holder does not allow a full scan until the edge of the cavity aperture. Furthermore, the contact springs between the cavity main body and the strip lines will also cover a small section of the cavity aperture (see figure 17a). Figures 31 and 32 show the final volume measured in the x-y plane and the x-z plane.

As soon as the measured points are set, the next step is to produce the static magnetic field. A Heizinger power supply provides the current to the coils. It was then connected in series to a Keithley multimeter, which was in charge of measuring the current with high precision. The multimeter was coupled to the coils circuit box (see figure 30), where the four coils were connected. It is important to have the coils connected in series to have exactly the same current on all coils. Furthermore the box is placed oustide of the shielding, which allows swapping between the aforementioned operation modes without having to open the three layer shielding. This is an advantage for the field measurement (see section 4.3.1). The series connection allows the current to run through all coils, just the smalls or just the big coils.

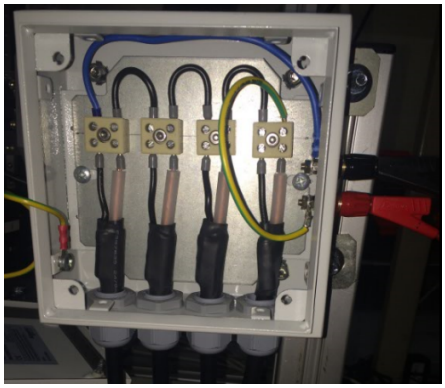

Figure 30: Circuit box. Configuration for driving all 4 coils at the same time

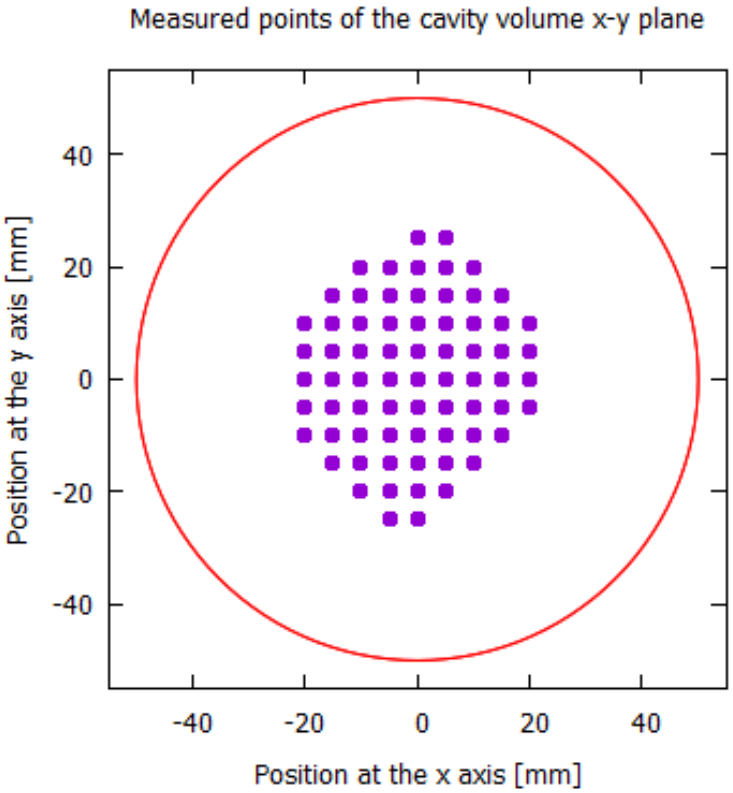

Figure 31: Measured points in the x-y plane where B_x, B_y and B_z values are known for the 0° and the 180° measurement. The red circle represents the cavity opening

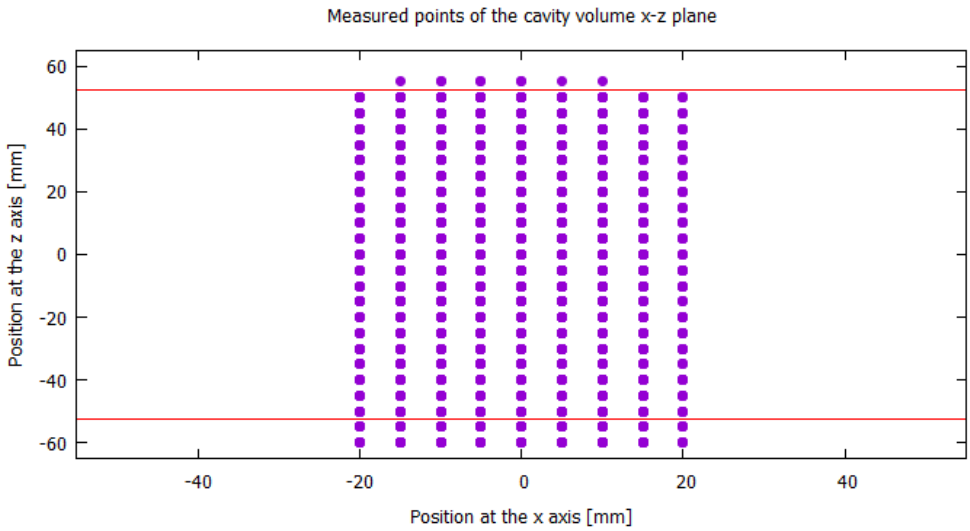

Figure 32: Measured points in the x-z plane where B_x, B_y and B_z values are known for the 0° and the 180° measurement. Bottom red line represent the cavity entrance, the upper line the cavity exit

Finally, a PT 100 temperature sensor was inserted inside the shielding volume to measure the temperature and to look for any temperature dependency of the magnetic field measurement. All the components were connected to the computer as shown in the data acquisition schematic (see figure 33).

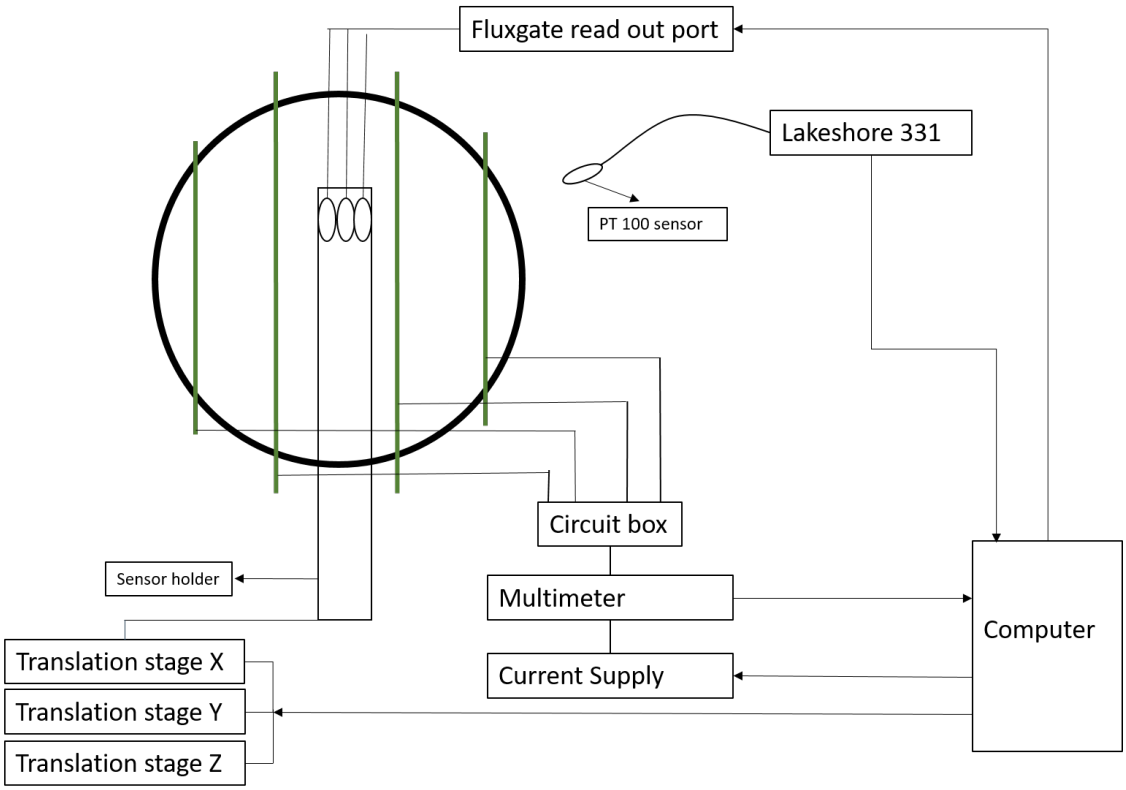

Figure 33: Data acquisition schematic for the magnetic field measurement of the McKeehan-like coils

4.3.1 Results

To find the homogeneity of the static magnetic field, 3 fluxgate sensors were used to measure the magnetic field inside the cavity. Besides, the measurement should determine the coils' position in which the homogeneity is optimized. To achieve this, the superposition of magnetic fields as well as linear interpolation are going to be used. As mentioned before, the position of the coils can be changed. The coils will be first placed in the position given by the simulations. Afterwards, the distance between the coils of a pair will be reduced 4 mm total (2 mm each side). This will be called the starting point or 0 mm. Then the coil pair distance was increased 8 mm (4 mm each side), this will be known as the 4 mm position.

At these two positions the magnetic field was measured for a current of 1 A for the following 16 configurations:

- Small-Coils_0mm (0° and 180°),
- Small-Coils_4mm (0° and 180°),
- Big-Coils_0mm (0° and 180°),
- Big-Coils_4mm (0° and 180°),
- 4-Coils_0mm (0° and 180°),

- 4-Coils_4mm (0° and 180°),
- Background_0mm (0° and 180°) and
- Background_4mm (0° and 180°).

As mentioned in the previous section a circuit box permits the selection of the coils which are going to be supplied with current. The name on the list indicates which coils were supplied with current. Background means that no current was flowing through any of the coils.

The fluxgates have a small offset. In order to eliminate the influence of this offset in the final results, the measurements were done with the pin of the rotating disk at 0° and 180° (see figure 29b).

To find the best position for the coils, one can calculate the total magnetic field produced by all 4 coils by linearly combining the magnetic field produced by the small coils and the big coils. As apparent form the list above, measurements with only one coil pair were done for the 0 mm and the 4 mm position. Assuming linearity of the change of the fields between the slightly different start (0 mm) and end (4 mm) position, one can use interpolation to create a grid of the homogeneity values for different coils positions between 0 mm and 4 mm.

To calculate the results presented in figure 34 the following procedure was followed:

1. Measurement: Using a labview based program and the setup described in the last section, the position of the origin of the head holder, magnetic field of the x, y and z axis, current and temperature were taken for the 16 configurations mention above.

2. Correction of the position script: Using table 3 the data of the position was changed into the actual position of the sensor. The corresponding magnetic field measurement, current and temperature are attached to each corrected position

3. Background subtraction: Using the last 4 configurations mention above, one can subtract the background from the magnetic field measurements.

4. Sensor offset correction: To correct for an offset of the fluxgates the magnetic field measurement of the 0° and 180° configuration were combined to give an offset corrected (oc) value:

$$\frac{\vec{B}_{\mathrm{oc}}}{I} = \frac{1}{2}\left(\frac{\vec{B}_0}{I_0} + \frac{\vec{B}_{180}}{I_{180}}\right), \tag{73}$$

   where B_0 and B_{180} are the magnetic field measured corresponding to a 0° and 180° configuration, similarly I_0 and I_{180} are the current values recorded by the high precision multimeter.

5. Interpolation of the $\vec{B}_{\mathrm{oc}}$ values: The interpolation was done using the following algorithm (the normalization to the current I is omitted):

$$\vec{B}(j)_{\mathrm{sm,s}} = \frac{j-1}{8} \cdot \vec{B}_{\mathrm{oc\_sm\_4,s}}(j) + \frac{9-j}{8} \cdot \vec{B}_{\mathrm{oc\_sm\_0,s}}(j), \tag{74}$$

$$\vec{B}(l)_{\mathrm{bg,s}} = \frac{l-1}{8} \cdot \vec{B}_{\mathrm{oc\_bg\_4,s}}(l) + \frac{9-l}{8} \cdot \vec{B}_{\mathrm{oc\_bg\_0,s}}(l), \tag{75}$$

$$\vec{B}(j,l)_{\mathrm{final,s}} = \vec{B}(j)_{\mathrm{sm,s}} + \vec{B}(l)_{\mathrm{bg,s}}, \tag{76}$$

   where j and l runs from 1 to 9, s runs from 1 to the total number of points.

6. Homogeneity calculation: Finally, the norm of $B(s)_{\text{final}}$, its mean value and standard deviation were computed to calculate the homogeneity value for each grid point according to equation (72). Figure 34 shows the result of the expected homogeneity distribution calculated from the measurement by interpolation and superposition as described above.

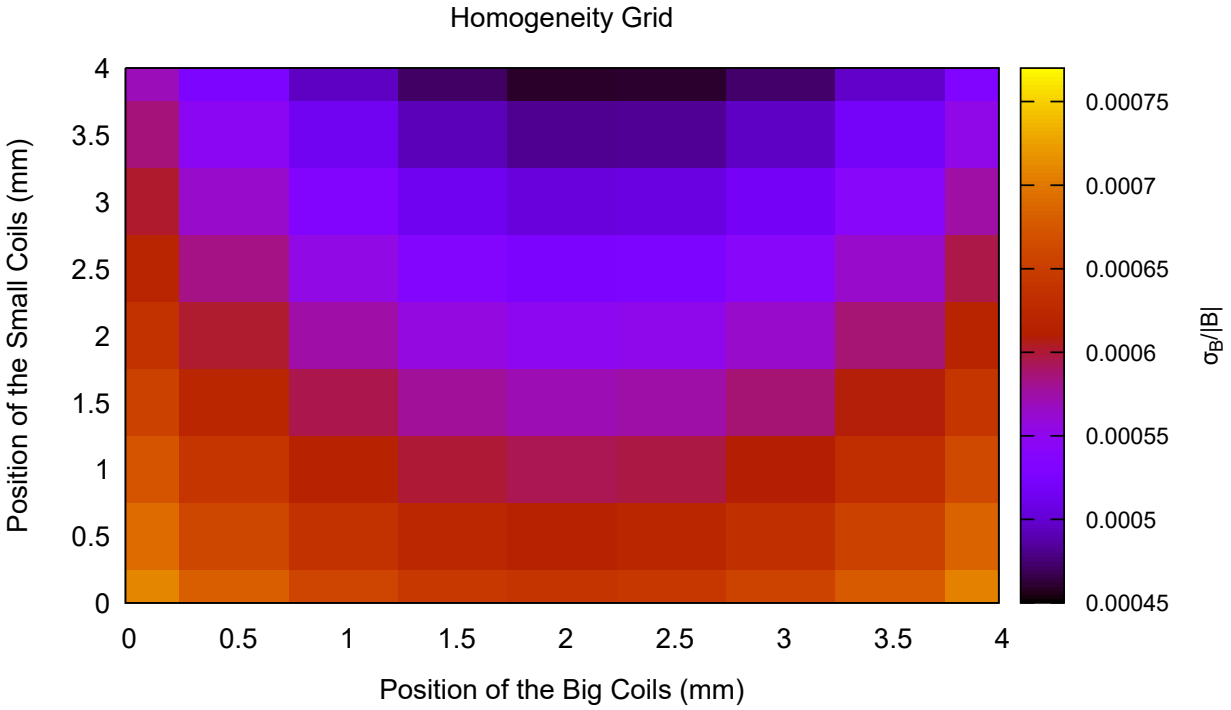

Figure 34: Homogeneity grid for different coils position

To evaluate the validity of the assumption that the total magnetic field can be given as a superposition of the magnetic fields produced by the small and big coils individually, the homogeneity of the 4 Coils measurements for 0 mm and 4 mm were compared to the homogeneity calculated using the previous process calculations. Table 4 compares the homogeneity values of superposition field to the one of the directly measure field.

Table 4: Comparison of the homogeneity

	Superposition (ppm)	4 Coils experimental measurements (ppm)
(σ_B/B)-0 mm	740	804
(σ_B/B)-4 mm	580	577

The difference between the 0 mm superposition and experimental results shows that values computed using superposition will have an uncertainty of $\approx$ 70 ppm. Furthermore, the best position for the coils can be found using figure 34. Table 5 compares the results from the simulations with the measured ones.

Table 5: Comparison of the optimal position to place the coils

	Simulations (COMSOL)	Experimental measurements with superposition
Small Coils position	2 mm	4 mm
Big Coils position	2 mm	2 mm
(σ_B/B)	≈200 ppm	≈450 ppm

After finishing the analysis the coils were placed in the optimal position (i.e. 4 mm for the small coils and 2 mm for the big one). The magnetic field inside the cavity was measured again to calculate the final homogeneity value:

$$\boxed{\frac{\sigma_{\mathrm{B}}}{\mathrm{B}} = (590 \pm 70)\mathrm{ppm}} \tag{77}$$

The actual value is higher than the one expected using superposition and linear interpolation. For table 4 one sees that the approximation is good but not ideal, this will have an effect on the final value. A probable more technical reason is the difficulty to set the coils in the exact same position as they were before. In principle the design of the mount uses a single-piece structure and dowel pins for exact positioning of coils with respect to another, and distance rings should enable to reproduce every chosen position. However, it is not a smooth process to mount the coils without forces and tricks. That means that the final position could be tilted by a very small angle compared to the position it was before moving the coils. This can produce a small variation on the field lines which also influence the final result. Nonetheless, the final value is under the maximal value needed ($\approx$ 1000 ppm) to resolve the double peak structure. It is important to mention that there is a possibility for a better homogeneity if the small coils are moved even further apart (beyond the 4 mm position). This is technically possible to do for the actual setup. Due to time reasons this possibility could not be investigated in the scope of this work.

5 Measuring the hydrogen ground state hyperfine splitting

This chapter will describe the measurements and determination of the hydrogen ground state hyperfine splitting frequency. While previous measurements with this apparatus used the σ_1-transition only, here the π_1-transition is included.

5.1 Optimization of the beam signal

To observe a clear drop in the count rate as indication for spin-flips a strong beam signal (as defined in section 3.5) is desired. The bigger the count rate is the more precise the fit result will be. The beam was detected using a QMS detector and the beam signal was obtained using LIA method (see sections 3.4 and 3.5). A Labview based program recorded the count rate. This program allows the user to set a time interval in which the counts are accumulated (e.g. every 5 min). Also the amount of time intervals can be set (e.g. 100 intervals of 5 min each). The program will then plot the beam count rate versus the time (other parameters can be also used for the y axis. It was found out that the LIA first order amplitude is the most sensitive parameter to changes in the beam line). When changing experimental conditions the effect on the beam rate can be observed, thus allowing for the optimization of the setup. The most important parameters are:

- Cold head position,
- Analysis sextupoles position and
- QMS position.

The cold head has three screws that change the position of the aluminum plates encapsulating the Teflon tube (see section 3.1). The analysis sextupoles can be moved along the 1 m CF40 pipe (see figure 7). The QMS aperture shown in figure 12a is connected to a 2D translation stage, which allows for the movement of the QMS aperture.

For the final beam optimization before the measurement, 116 intervals of 30 seconds were taken. The amount of counts measured by each interval is a statistical process which is described by Poisson statistics. For that reason, more than 1 set were measured for each condition. Table 6 summarizes the changes made and the effects they had on the LIA first order amplitude (see section 3.5). The mean value is given in the sixth column of table 6. The set number where the change was made was not taken to calculate the mean value. The results are plotted in figure 35.

A strange drop was measured at set 38 (see figure 35). This point was also discarded when computing the mean value. After the optimization the beam rate increased from (431 ± 21) Hz to (601 ± 25) Hz. These two values are the beam count rate for the first and last value of column six.

The next parameter to be optimize was the position of the QMS. Using a 2D translation stage, a scan of the detector chamber can be performed. A window of 3x3 mm was scanned. At each point 2 sets of 30 seconds were measured. Figure 36 shows the results of this scan.

The QMS was moved to the optimal position, which corresponds to a distance of 16.6 mm for the x axis and 27.6 mm for the y axis. The distance was measured from the base of the translation stage until the adjustable part of the stage. After the optimization process of the QMS position the beam count rate increased from (613 ± 25) Hz to (932 ± 31) Hz.

Table 6: Optimization of the beam signal. The distance between the two metal plates regulated by the cold head knobs is given, the knobs were were named A,B,C. The position of the analysis sextupoles were measured from the upstream edge of the 1 m CF40 pipe until the edge of the first sextupole holder.

Set number	Coldhead position [mm]			Analysis sextupoles position [cm]	First LIA amplitude [Hz]
	A	B	C		
1-8	39.90	42.67	42.00	28.50	42 ± 7
10-13	38.50				53 ± 8
15-18	38.00				48 ± 7
20-23	37.50				47 ± 7
25-28	37.90				44 ± 7
30-33		42.50			59 ± 8
35-42		42.25			74 ± 9
44-47		41.70			78 ± 9
49-52			41.65		80 ± 9
54-57			41.10		56 ± 8
59-62			41.40		60 ± 8
64-75		41.40			69 ± 9
77-81	38.40				75 ± 9
83-89	38.76	41.40	41.40	28.50	72 ± 9
91-92				38.50	33 ± 6
95-98				18.50	82 ± 10
102-106				8.50	81± 10
110-116				21.50	79 ± 9

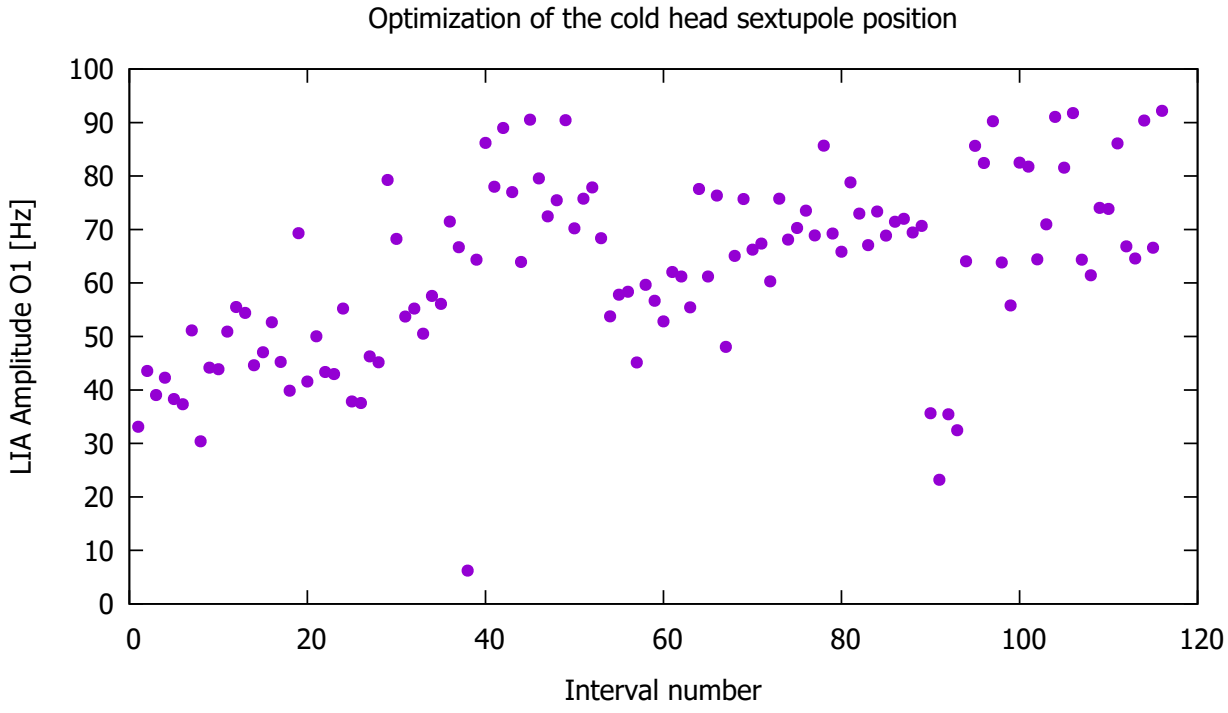

Figure 35: Optimization of the cold head and sextupoles position

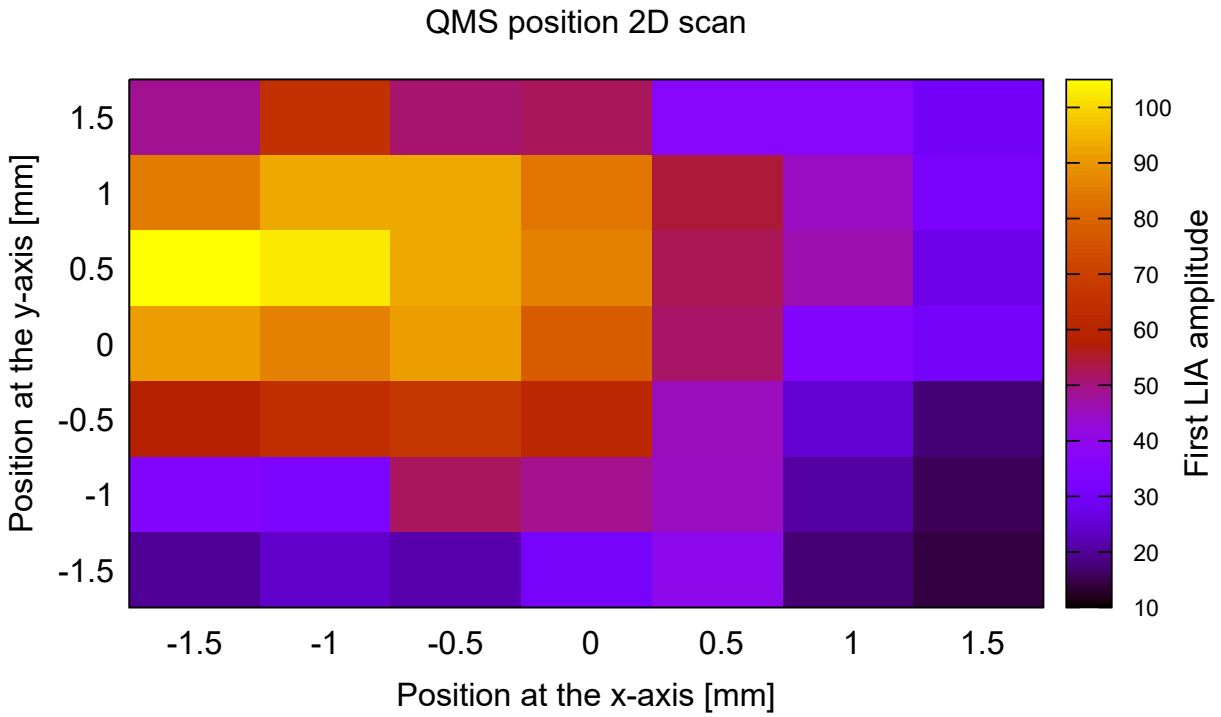

Figure 36: Optimization of the QMS position

5.2 Optimization of the cavity

To drive the π_1 and σ_1 transitions, the first harmonic of the cavity has to be at the ground state hyperfine splitting frequency (given in equation (15)). The structure of the resonance peaks can be investigated using the vector network analyzer (VNA), more specifically, by looking at the S-parameter (see appendix 6). For the optimization, the parameter of interest is the S21, defined as the forward voltage gain. The measurement will follow the schematic shown in the figure 17b. However, this time the VNA will produce and read the signal. The signal generator is not used for the optimization. The optimization was performed for three setups (all of them taken at a pressure of $\approx 10^{-6}$ mbar):

1. Setup 1: The VNA is connected directly to the cavity port 1 where the antenna will produce the oscillating magnetic field. The pick up antenna (port 2) will be connected back again to the VNA.

   Figures 37a and 37b shows the S-parameters for a power output of 0 dBm a frequency span of 1 GHz and 50 MHz.

   The M2 marker points the position of the peak maximum while the M1 marker is set to the desired frequency. It can be seen that the first resonance structure is not at the desired frequency

2. Setup 2: An amplifier was introduced between the VNA and the cavity port1 one. Figures 38a and 38b shows the S-parameters for a Power output of -60 dBm a frequency, span of 1 GHz and 50 MHz.

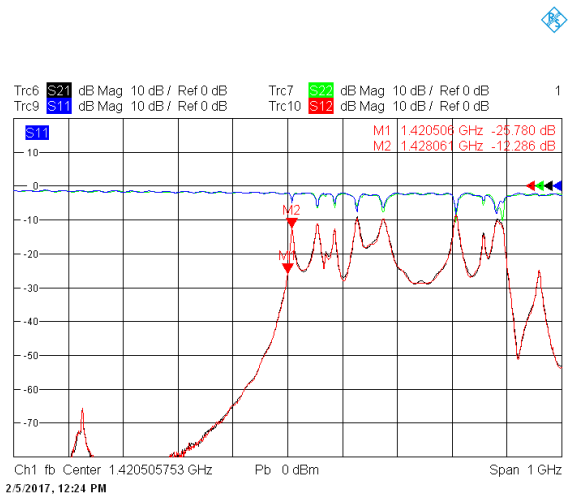

(a)

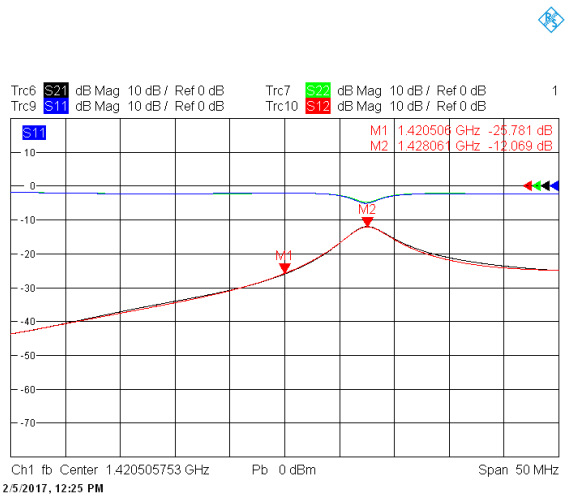

(b)

Figure 37: Setup 1 (a): S-parameters for a power output of 0 dBm and a frequency span of 1 GHz (b): S-parameters for a power output of 0 dBm and a frequency span of 50 MHz

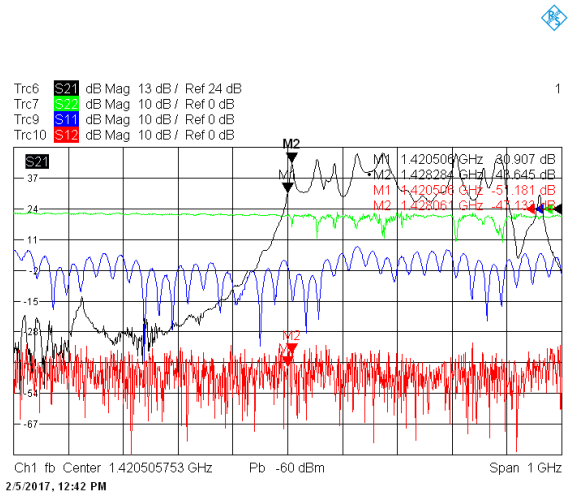

(a)

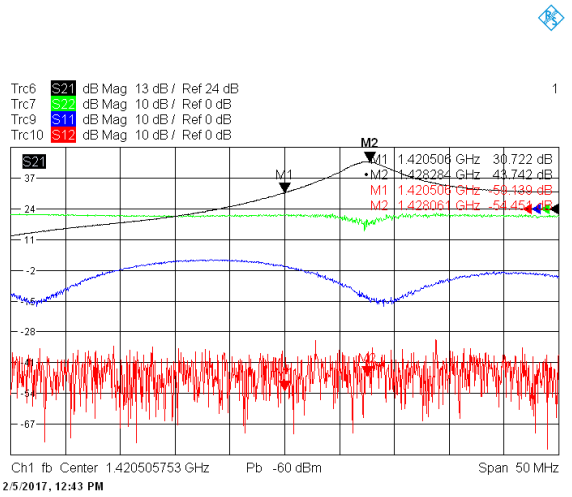

(b)

Figure 38: Setup 2 (a): S-parameters for a power output of -60 dBm and a frequency span of 1 GHz (b): S-parameters for a power output of -60 dBm and a frequency span of 50 MHz

3. Setup 3: The stub tuner was introduced between the amplifier and the cavity port1 one. Figures 39a and 39b shows the S-parameters for a power output of -60 dBm a frequency span of 1 GHz and 50 MHz.

   The stub tuner was used to optimized the first resonance. The optimal position was found for a distance of 9.59 mm between the stub tuner's ring connected to the cavity port 1 (see figure 40a) and the first element of the stub tuner. The ring connected to the amplifier and the second element were set to a distance of 49.48 mm (see figure 40b). Comparing figures 39b, 38b and 37b one can see that using the stub tuner a small peak was produced at the desired frequency.

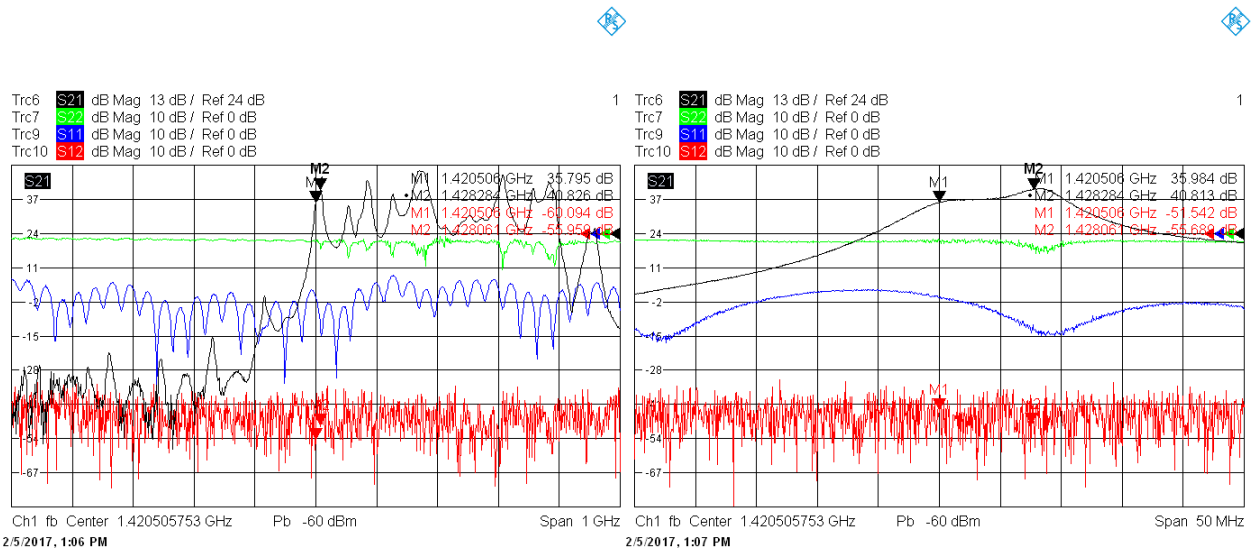

(a) (b)

Figure 39: Setup 3 (a): S-parameters for a power output of -60 dBm and a frequency span of 1 GHz (b): S-parameters for a power output of -60 dBm and a frequency span of 50 MHz

The marker M1 measured a power of 30.7 dB in figure 38b and a power of 36 dB in figure 39b (it increased by a factor of 3.4). It is also important to mention that the frequency scan span to measure the π_1 and σ_1 was $\approx$ 50 kHz. Within this frequency span the power can be regarded as constant. The flat region between the markers is beneficial specially for the π_1-transition due to its higher dependency on the magnetic field. At 10 Gauss the transition frequency will shift by more than 10 MHz, which is already more than the distance between the markers.

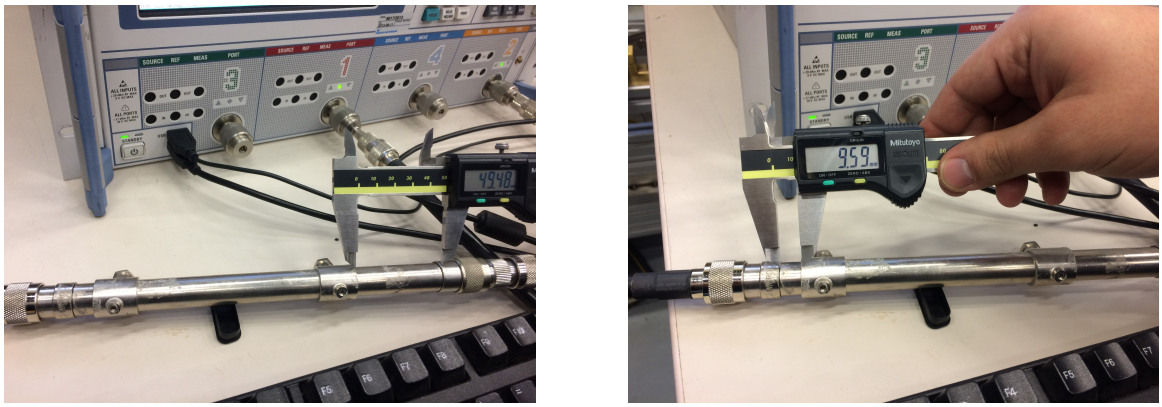

(a) (b)

Figure 40: Stub tuner optimal position

5.3 Line shape and fit function

The two level system (see section 2.3) or the optical Bloch equation [17] describe the line shape of the transition probability. The system was solved using numerical algorithms in [17, 29]. The solution of the transition probability as a function of the frequency detune and the oscillating magnetic field amplitude for a mono-energetic beam (i.e. given interaction time) in conventional Rabi spectroscopy and a strip line cavity are shown in figure 41. A structure like the one shown in the panel (d) is expected for the transition measurements

in this setup. However, the actual hydrogen beam is not mono-energetic. The particles will travel through the cavity with different velocities. This means that they will experience different interaction times. The transition probability depends on the interaction time of the particles with the oscillating magnetic field.

To account for this velocity spread the final fit function is a weighted sum of several mono-energetic lines-shapes. The line shapes for different velocities can be scaled using $B_0' = B_0 \frac{v'}{v}$ and $\Omega_D' = \Omega_D \frac{v'}{v}$ where Ω_D is the detune frequency.

The final transition probability function performs a 2D spline interpolation on a grid of simulated values. The weights for different velocities use binomial factors as an approximation of a Gaussian velocity distribution.

The initial fitting program was developed in C++/ROOT by C. Jepsen [37] and improved by M. Diermeier [9]. A Matlab routine was written by M. Wiesinger [24], which is also used for the present analysis. The fit function for the detected rate S is given by:

$$S = b - aP(\Omega_D - \Omega_T; v, \sigma_v, B_0) \tag{78}$$

where P is the transition probability, a and b scale the probability to the observed rate. The parameter of the fit function are the velocity v, the beam velocity width σ_v, the oscillating magnetic field inside the cavity B_0 and the transition frequency Ω_T.

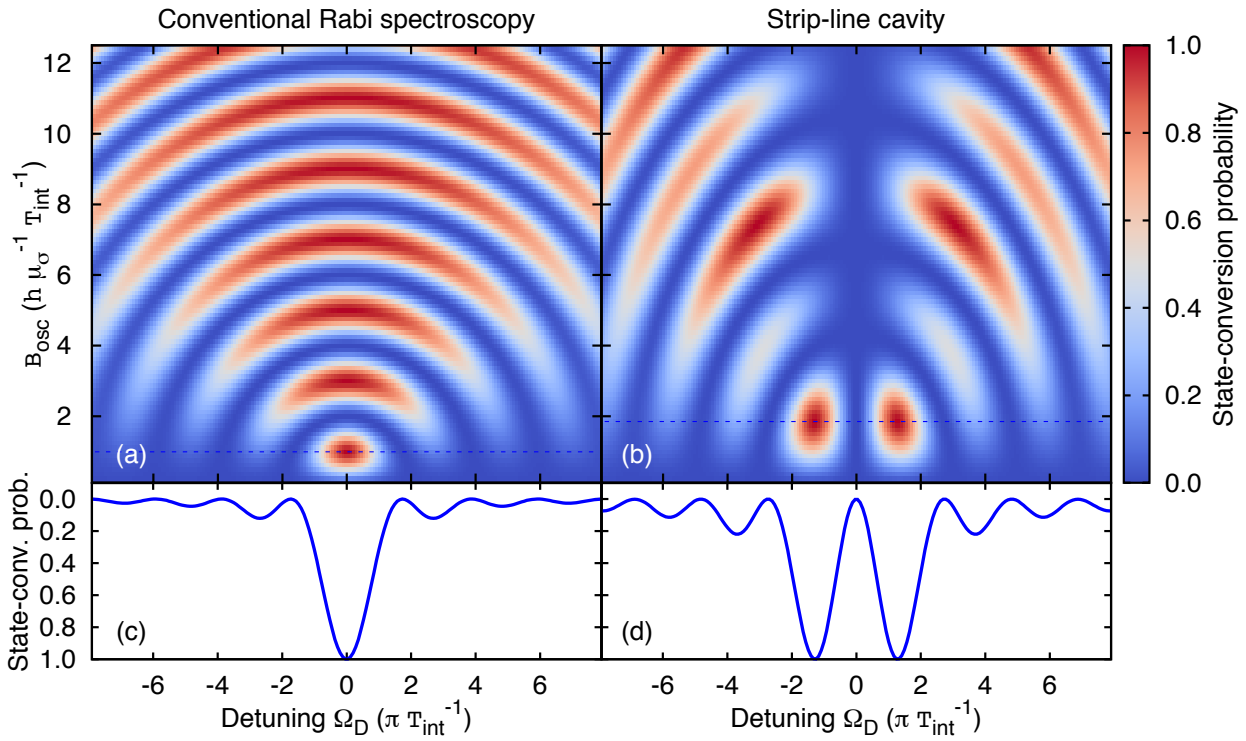

Figure 41: Spin flip probability conversion for conventional Rabi spectroscopy and the Strip-line cavity. The (a) and (b) panels show the transition as a function of the oscillating magnetic field and the frequency detune. The (c) and (d) panels show the transition as a function of the detune frequency for a constant oscillating magnetic field at the first conversion maximum. Taken from [38].

5.4 Power scan

As the figure 41 suggests, by doing a power scan for a constant frequency (in the case of conventional Rabi spectroscopy at the transition frequency and in the present case at an appropriately detuned frequency) one can find the optimal power where the state conversion

is maximized. This power was used during the frequency scans. It was shown in section 2.3.1 that the π_1 and σ_1 transitions need different oscillating magnetic field values to achieve the same spin flip probability. That corresponds to different power values. Figures 42 and 43 correspond to the results of the power scan done for the π_1 and σ_1 transitions.

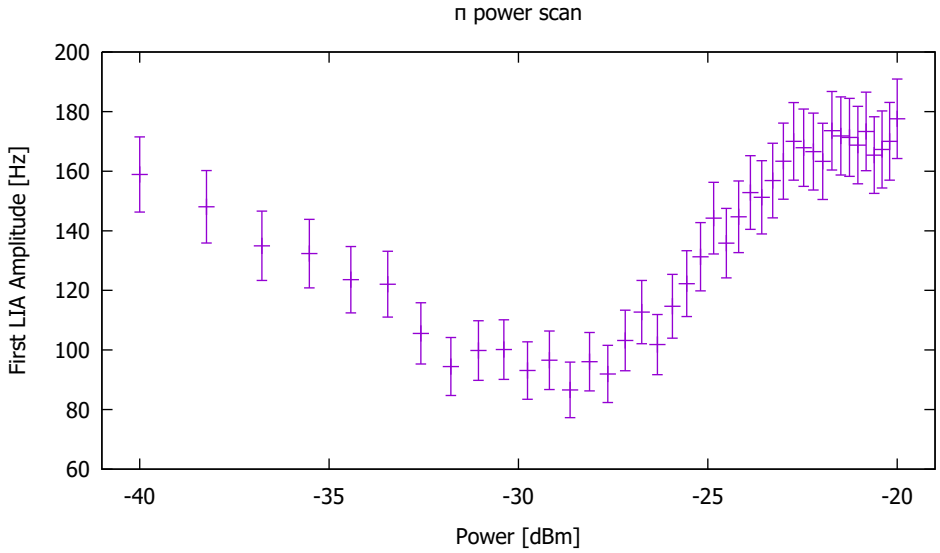

Figure 42: π_1-transition power scan

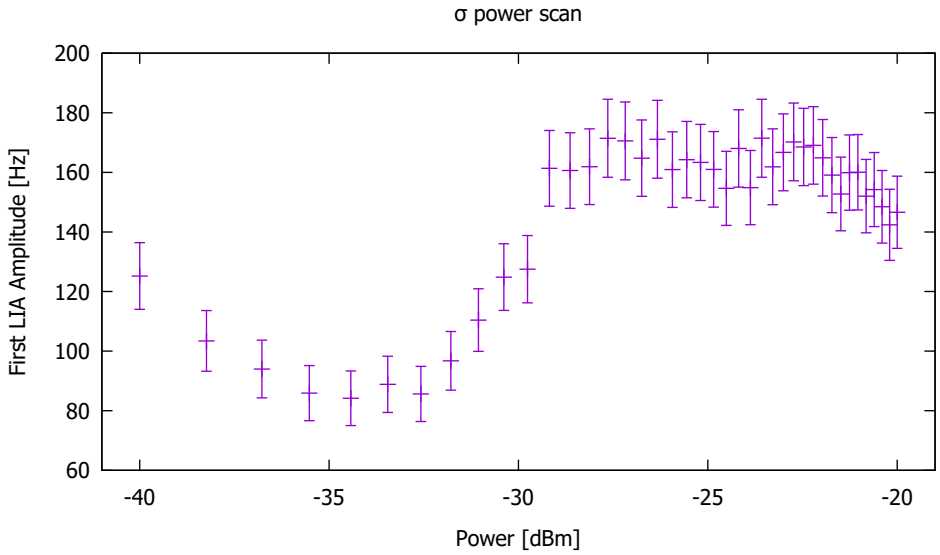

Figure 43: σ_1-transition power scan

The power used during the measurements was -34.5 dBm for the σ_1-transition and -29 dBm for the π_1-transition.

5.5 Structure of the acquired data and outline of the analysis

Using a Labview based program frequency scans can be performed. This program also recorded histograms of the count rate versus chopper phase for every single frequency scan point for an improved extraction of the beam rate during the off line analysis. The thus

obtained count rate versus the frequency can be plotted and the fit function discussed in section 5.3 can be used to extract the central frequency.

The nomenclature introduced in table 7 will be used to make the description of the measurement clearer.

Table 7: Nomenclature for the measurement

Term	Definition
Cycle	A cycle describes a single frequency scan over a span of 50 kHz. The scan consists of 41 points stepped in a random sequence. Each point is measured twice for 15 seconds.
Scan	A scan is a repetitive data acquisition of cycles at a fixed current in the McKeehan-like coils. A scan consists of 2 cycles.
Set	A set consists of a series of scans taken for 6 different currents in the McKeehan-like coils.

The McKeehan-like coils were set to the following currents:

- 0.5 A (and the inverted polarity). Corresponds to a B_{stat} of $\approx 1.16 \cdot 10^{-4}$ T,
- 0.3 A (and the inverted polarity) Corresponds to a B_{stat} of $\approx 6.98 \cdot 10^{-5}$ T,
- 0.1 A (and the inverted polarity) Corresponds to a B_{stat} of $\approx 2.33 \cdot 10^{-5}$ T.

With the Heizinger PTNhp 32-10 power supplier the polarity can be inverted by remote control using a Labview based program.

The data acquisition scheme proceeded as follows:

1. A scan is going to be taken for a σ_1-transition (Power -34.5 dBm) and a current value of 0.5 A then for a π_1-transition (Power -29.0 dBm).
2. The current was changed to 0.3 A and the frequency center was adjusted to the corresponding theoretical transition frequency value. One more time a σ_1 and π_1 scan were measured.
3. The first two steps were repeated for the other 4 currents. Resulting in a complete set.
4. The first three steps give a set with a total amount of six σ_1 scans and six π_1 scans. The total measurement consists of 13 sets. Accordingly 156 scans have been recorded in a period from February 10th until February 15th of 2017.

The following steps were done in order to calculate the hydrogen ground state hyperfine splitting:

1. All scans were fitted using the fit function discussed in the previous section.
2. Using the fit results the velocity parameter was fixed to a common mean value (see section 5.6).
3. Using the fit results the oscillating magnetic field parameter was fixed to a common mean value (see section 5.7).
4. All scans were fitted again using the fit function with a fixed velocity and oscillating magnetic field value.
5. Using the resulting transition frequencies from step 4 the hyperfine structure can be determined using three methods (see section 5.8).

5.6 Analysis of the beam velocity

The velocity values given by the fit function were analyzed in order to find a common mean value and fix this parameter for the fit function. Simulations were done to compute the expected velocity of the states. The results are presented in figure 44.

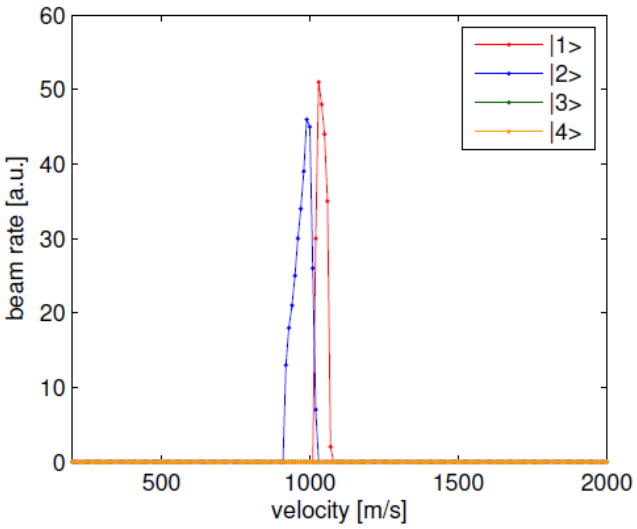

Figure 44: Simulated expected velocities for the 4 hydrogen ground states. Taken from [24].

From this figure, it can be seen that the states $|1\rangle$ and $|2\rangle$ are expected to have different velocities. For this reason, it is important to separate the fit results between σ_1 and π_1 during the analysis.

The σ_1-transition velocity

The fitted values of the velocity of all the σ_1 scans were plotted to investigate the possibility of fixing the velocity. Figure 45 shows the results for velocities.

It can be seen that the measured points scatter around the weighted mean value, like expected for a purely statistical process. 97.43 % of the measured points are within two sigma. Furthermore the Birge ratio [39] was calculated to check the statistical consistency of the fit and is equal to 0.90. These two parameters give a quantitative confirmation that the measurements deviate just statistically from the weighted mean value (statistically 95% of the points should be within two standard deviations, which is known as the 95% confidence level and the Birge ratio should be equal to unity). The velocity was fixed to the calculated weighted mean value of:

$$v_{\sigma_1} = 1014.61 \text{ ms}^{-1}, \tag{79}$$

for the σ_1-transition.

The π_1-transition velocity

The same analysis was done for all π_1 scans. Figure 46 shows the results of the velocity values extracted from the fit function:

This time one of the scans had a deviation of almost 5 sigma. It was scan point number 64. This point is not shown in figure 46 and was taken out for the computation of the weighted mean value. Once again 97.40 % of the points are within two sigmas (96.15% including point 64). The Birge ratio is 0.98. The velocity was fixed to the weighted mean value of:

$$v_{\pi_1} = 1083.76 \text{ ms}^{-1}, \tag{80}$$

for the π_1-transition.

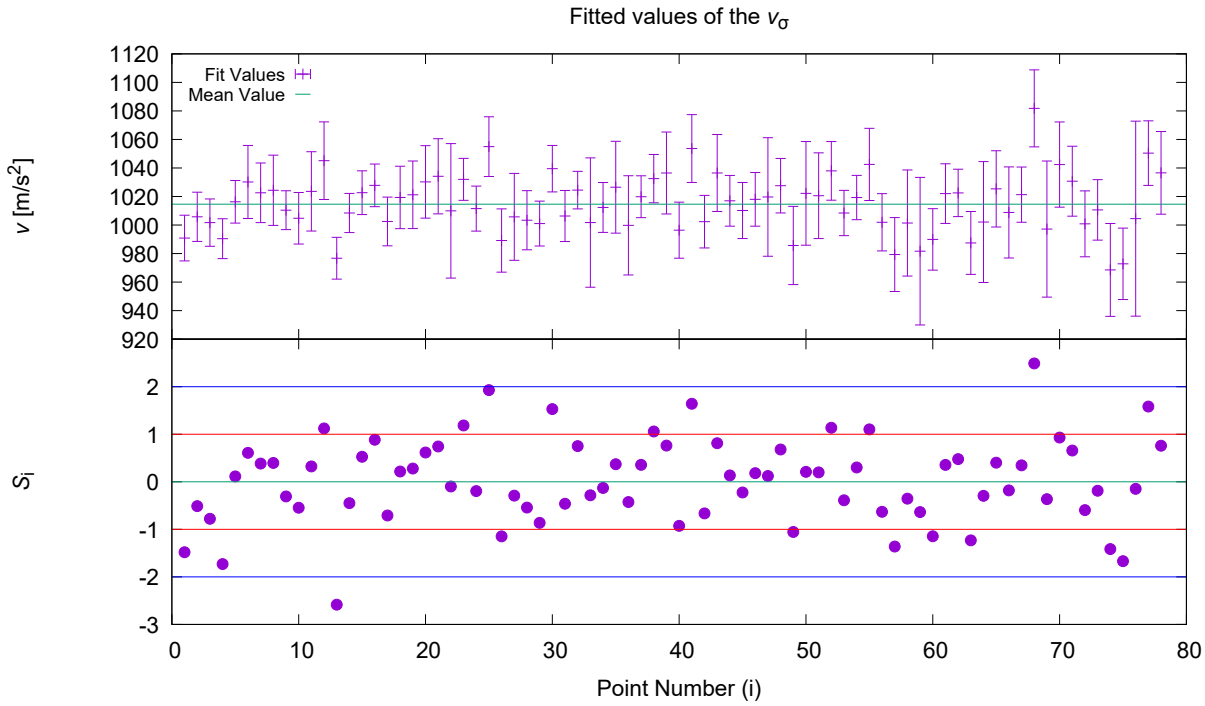

Figure 45: Fitted beam velocity values for each σ_1 scan. Upper section shows the velocity and the lower part shows the standard score, which is the number of standard deviations by the measured points deviates from the mean value.

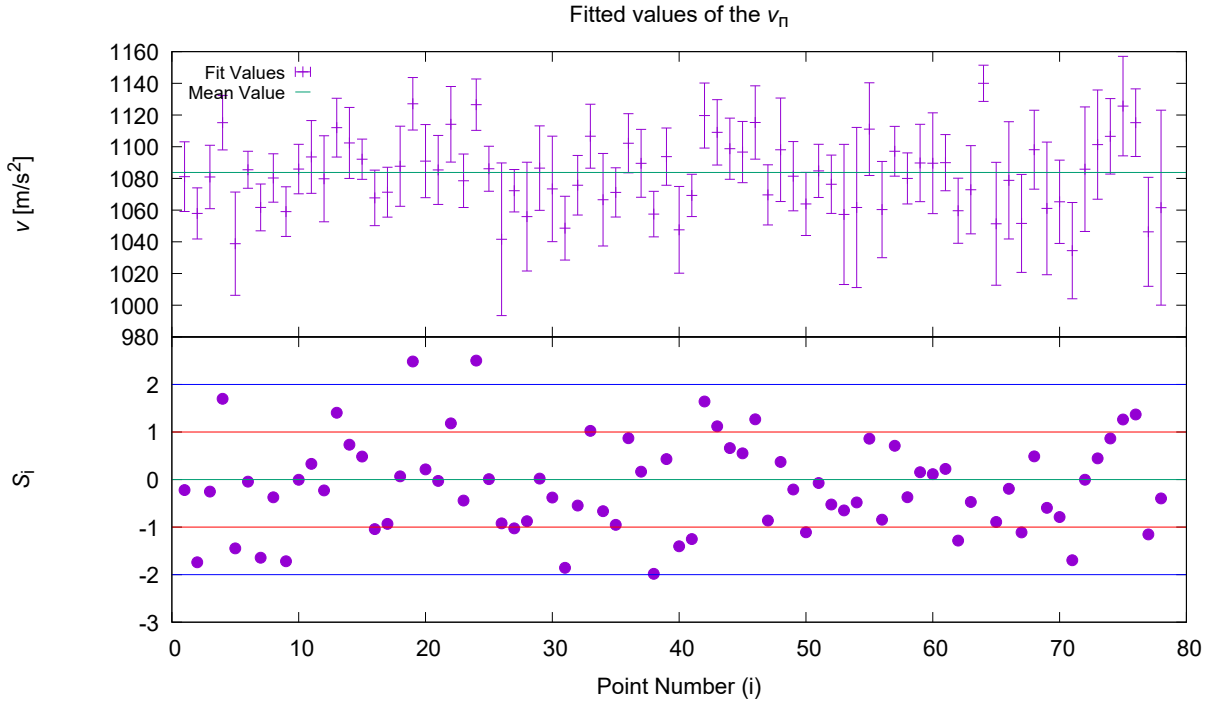

Figure 46: Fitted beam velocity values for each π_1 scan. Upper section shows the velocity and the lower part shows the standard score.

For this setup, the transmitted velocities were calculated using the simulation program and also from time of flight (ToF) measurements [24]. The TOF was calculated comparing the phase of a laser signal and the phase of the beam count rate using the LIA. Table 8 compares these results with the ones given by the fit function.

Table 8: Velocities comparison

	Velocity of the σ_1 transition [m/s]	Velocity of the π_1 transition [m/s]
Simulations	974.1	1040.4
ToF	997 ± 12	1074 ± 15
Fit results	1014.61 ± 2.33	1083.76 ± 2.4

From all the calculations it is clear that the velocity of the π_1 beam component (state $|1\rangle$) is higher than the σ_1 beam component (state $|2\rangle$). Furthermore, the fit results are in good agreement with the ToF measurement, especially for the π_1-transition. The simulation results suggest a slightly slower beam, which can be a consequence of the unrealistic ideal conditions assumed for the simulation.

5.7 Analysis of the oscillating magnetic field ($B_{\mathbf{osc}}$)

The same analysis as the one done in the previous section for the beam velocity can be done for the B_{osc}. The goal is to fix the B_{osc} value. As before, the σ_1 and π_1 transitions have to be filtered from one another. This time a second selection has to be done, because the transition frequency is different for the different static magnetic field configurations (see figure 3) and the effect of the cavity resonance structure might have a significant influence on the extracted B_{osc} values.

The σ_1-transition $B_{\mathbf{osc}}$

The σ_1 oscillating magnetic field was analyzed separately for ±0.5 A, ±0.3 A and ±0.1 A (where ± means that the second measurement was done with inverted polarity). The fitted B_{osc} values extracted from the fit function were plotted for each σ_1 scan. These results are shown in figures 47, 48 and 49.

The reason why the last scan in figure 47 has a very large standard deviation will be discussed at the end of this chapter. For this analysis, it will not be significant. 100% of the measurement points are within 2 sigmas and the Birge ratio is 0.87.

The B_{osc} weighted mean value for the σ_1-transition at 0.1 A is:

$$B^{\sigma}_{\text{osc}-0.1} = (579 \pm 19) \cdot 10^{-17}\ \text{T} \tag{81}$$

For the 0.3 A σ_1 scans, 96.15% of the measured points are within 2 sigmas and the Birge ratio is 0.94.

The B_{osc} weighted mean value for the σ_1-transition at 0.3 A is:

$$B^{\sigma}_{\text{osc}-0.3} = (601 \pm 17) \cdot 10^{-17}\ \text{T} \tag{82}$$

For the 0.5 A σ_1 scans, 96.15% of the measured points are within 2 sigmas and the Birge ratio is 0.88.

The B_{osc} weighted mean value for the σ_1-transition at 0.5 A is:

$$B^{\sigma}_{\text{osc}-0.5} = (595 \pm 18) \cdot 10^{-17}\ \text{T} \tag{83}$$

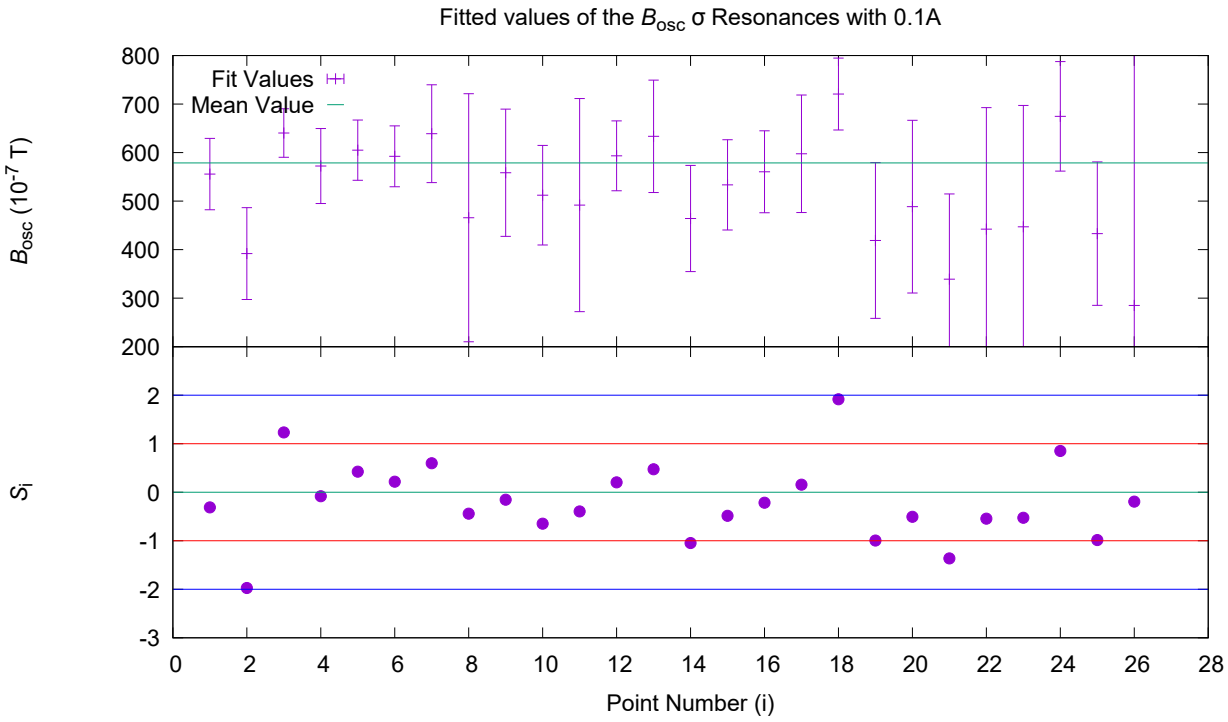

Figure 47: Fitted beam B_{osc} values for each σ_1 scan with $\pm$0.1A. Upper section shows the B_{osc} values and the lower part shows the standard score.

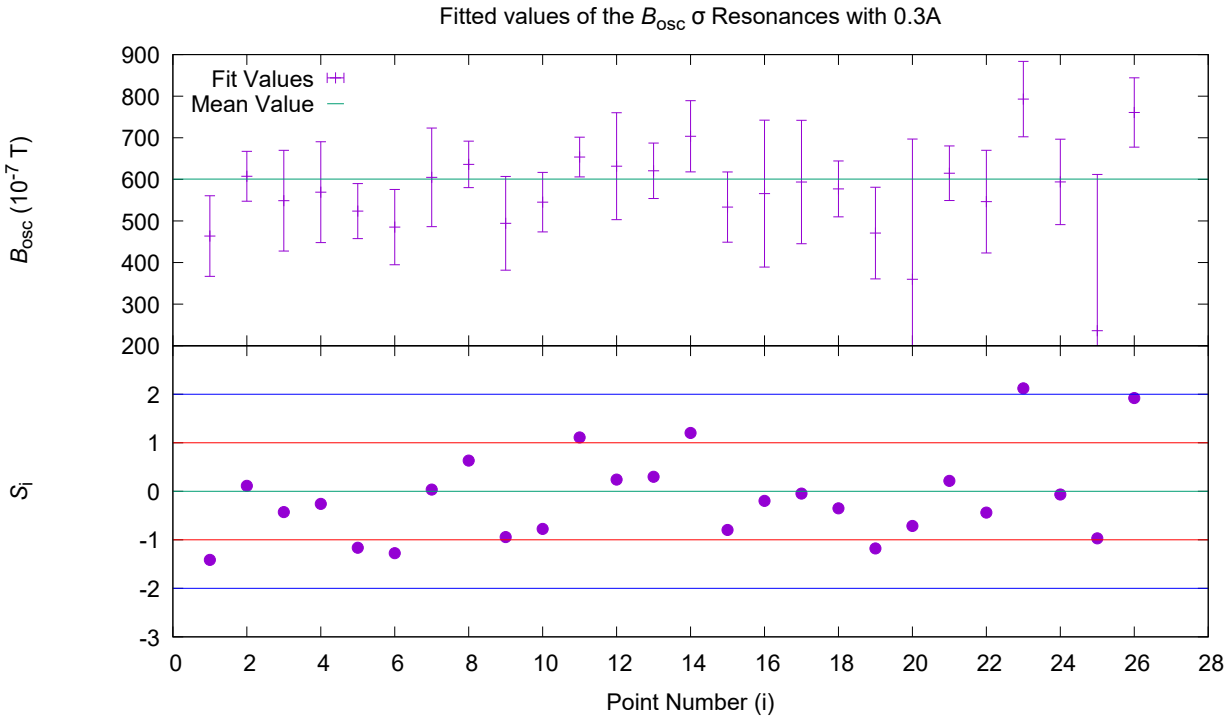

Figure 48: Fitted beam B_{osc} values for each σ_1 scan with $\pm$0.3A. Upper section shows the B_{osc} values and the lower part shows the standard score.

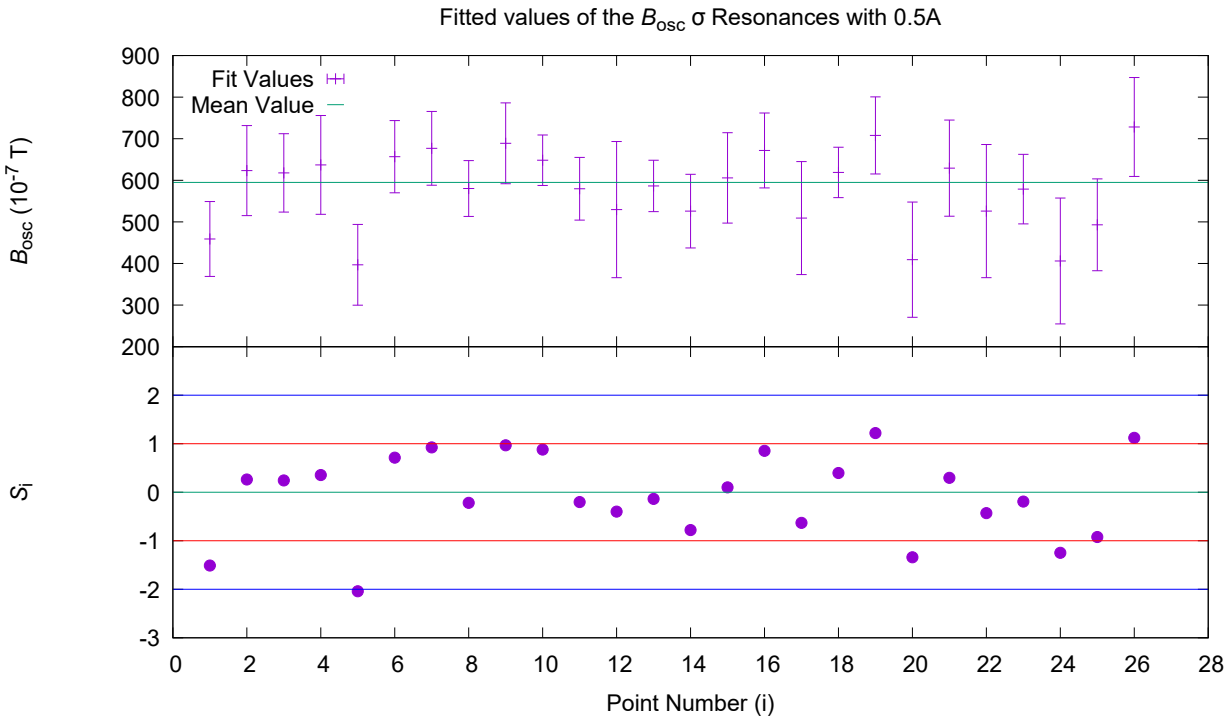

Figure 49: Fitted beam B_{osc} values for each σ_1 scan with ±0.5A. Upper section shows the B_{osc} values and the lower part shows the standard score.

The π_1-transition B_{osc}

The same analysis was made for the π_1-transition. The fitted B_{osc} values extracted from the fit function were plotted for each π_1 scan. These results are shown in figures 50, 51 and 52. The fit function uses the simulation of the σ_1-transition to do the spline interpolation. This means, it cannot distinguish between a σ_1 and a π_1 transition. The mean value result extracted from the fit parameter was multiplied by $\sqrt{2}$, which is the theoretical factor between the B_{osc} of the σ_1 and π_1 transitions when assuming same interaction time.

For the 0.1 A π_1 scans, the 100% of the measured points are within 2 sigmas and the Birge ratio is 0.80.

The B_{osc} weighted mean value for the π_1-transition at 0.1 A is:

$$B^{\pi}_{\text{osc}-0.1} = (1062 \pm 20) \cdot 10^{-17} \text{ T} \tag{84}$$

For the 0.3 A π_1 scans, 100% of the measured points are within 2 sigmas and the Birge ratio is 0.77.

The B_{osc} weighted mean value for the π_1-transition at 0.3 A is:

$$B^{\pi}_{\text{osc}-0.3} = (989 \pm 22) \cdot 10^{-17} \text{ T} \tag{85}$$

For the 0.5 A π_1 scans, 96.15% of the measured points are within 2 sigmas and the Birge ratio is 0.94.

The B_{osc} weighted mean value for the π_1-transition at 0.5 A is:

$$B^{\pi}_{\text{osc}-0.5} = (1024 \pm 23) \cdot 10^{-17} \text{ T} \tag{86}$$

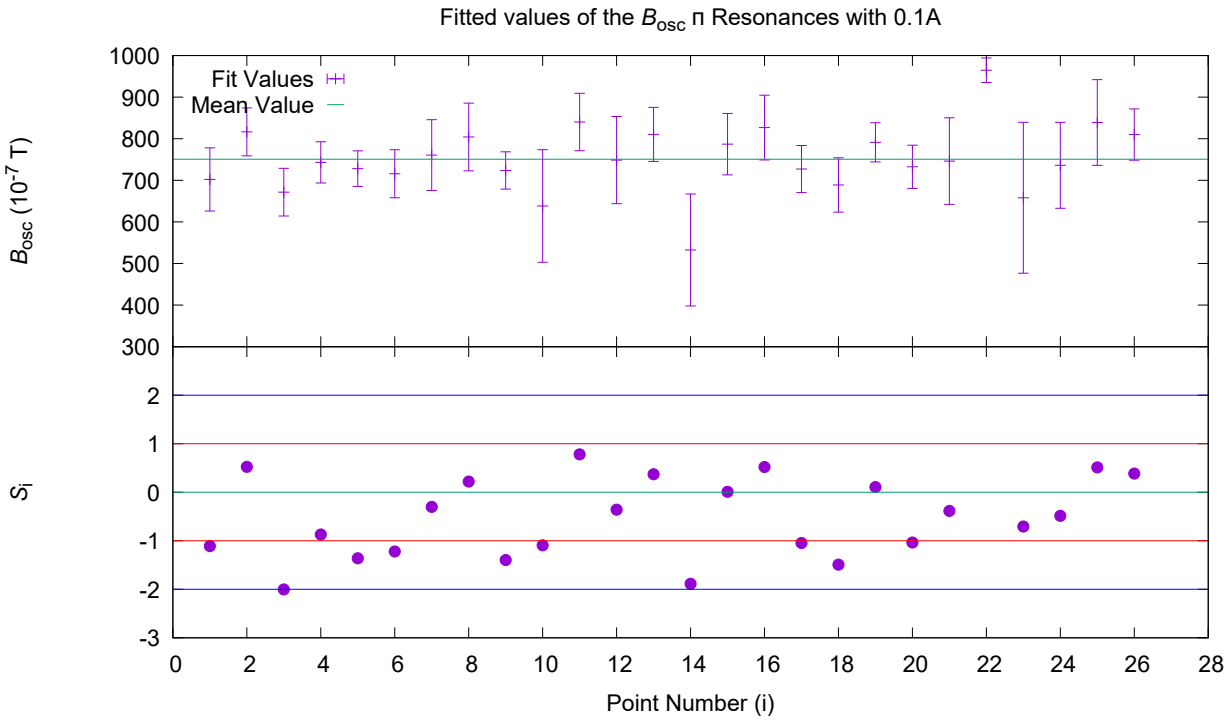

Figure 50: Fitted beam B_{osc} values for each π_1 scan with $\pm$0.1A. Upper section shows the B_{osc} values and the lower part shows the standard score.

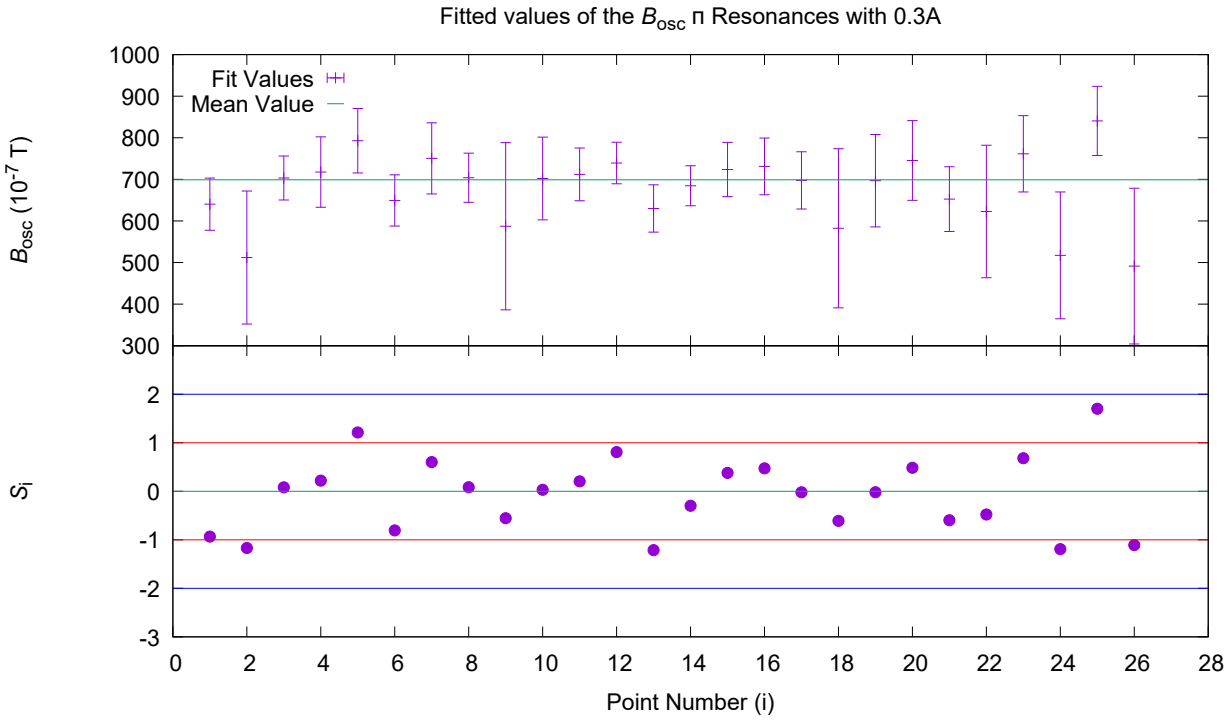

Figure 51: Fitted beam B_{osc} values for each π_1 scan with $\pm$0.3A. Upper section shows the B_{osc} values and the lower part shows the standard score.

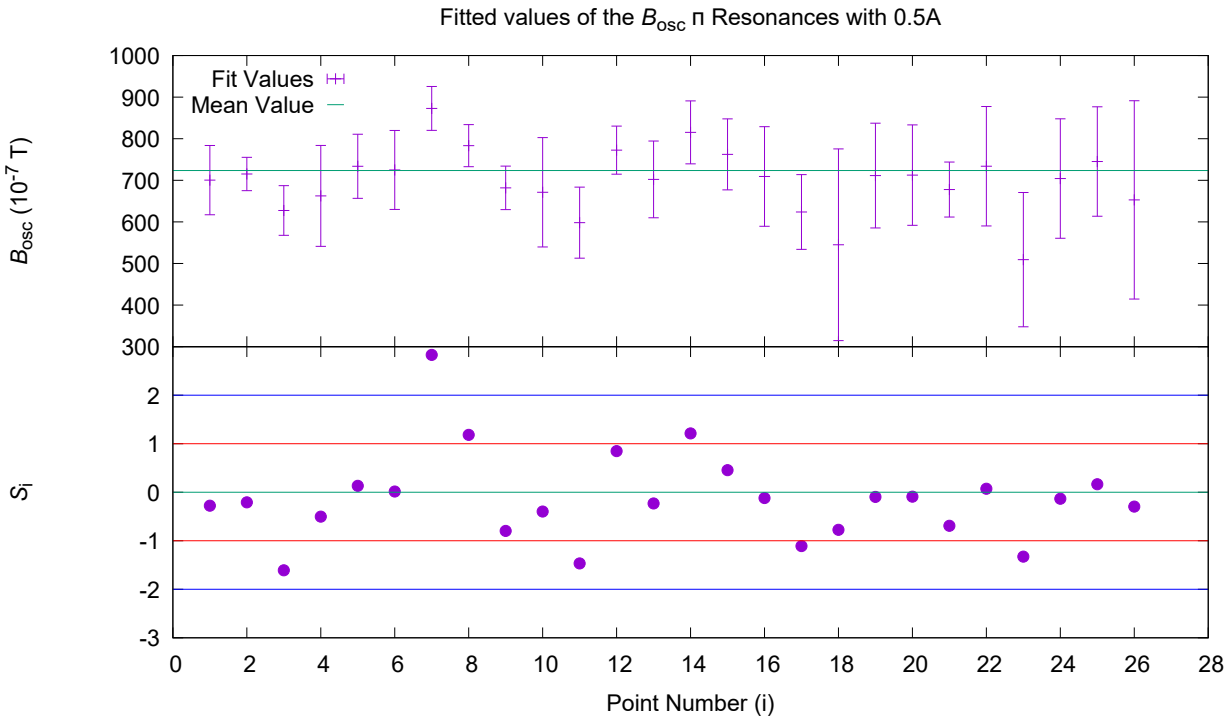

Figure 52: Fitted beam B_{osc} values for each π_1 scan with $\pm$0.5A. Upper section shows the B_{osc} values and the lower part shows the standard score.

A quantitative analysis can be made to see if the results are in accordance with theory. In section 2.3.1 it was shown that the optimal B_{osc} value is different for π_1 and σ_1 by a factor of $\sqrt{2}$ when assuming the same interaction time. Also, the B_{osc} was calculated for a similar interaction time with the cavity field, since the velocities are different for π_1 and σ_1 the interaction time will also be different. This factor has to be also considered when doing the comparison. The expected value is given by:

$$\frac{B^{\pi}_{\text{osc}}}{B^{\sigma}_{\text{osc}}} = \sqrt{2}\frac{v_{\pi}}{v_{\sigma}} = \sqrt{\frac{P^{\pi}}{P^{\sigma}}} \tag{87}$$

The left hand side of the equation was calculated using equations (81), (82), (83), (84), (85), and (86). The middle part of the equation was calculated using equations (79) and (80). The right hand side was calculated using the power (in μW) given in section 5.4 for the π_1 and σ_1 transitions as found experimentally with power scans (see figures 42 and 43). The results of these calculations are:

$$\begin{aligned} \frac{B^{\pi}_{\text{osc}}}{B^{\sigma}_{\text{osc}}} &= 1.73 \\ \sqrt{2}\frac{v_{\pi}}{v_{\sigma}} &= 1.51 \\ \sqrt{\frac{P^{\pi}}{P^{\sigma}}} &= 1.88 \end{aligned} \tag{88}$$

The power values were selected without using a fit function and larger deviation from optimal position has to be expected. It is possible that for P^{π} the deviation from the center

was bigger than for P^{σ}, this translates to a bigger final result for the power ratio. This will also affect the value of the B_{osc} extracted for the fit. These can be the reasons for the small differences seen in equation (88). Nevertheless, for a quantitative analysis the values given by the fit function are in reasonable agreement with the expected ones from the theory.

5.8 Hydrogen ground state hyperfine splitting results

With the new McKeehan-like coils, the ASACUSA hydrogen beam is now able to measure the π_1-transition between the ground-state hyperfine states as well. This allows for three methods to determine the zero field transition. First the three methods are going to be explained and then the results for the three of them are going to be given.

1. **Extrapolation of the σ_1-transition frequencies for different static magnetic fields**: The results of the σ_1 transitions can be plotted versus the static magnetic field and the points can be fitted using equation (32). The resulting fit function will be evaluated at zero to get the hyperfine splitting.

2. **Extrapolation of the π_1-transition frequencies for different static magnetic fields**: The results of the π_1 transitions can be plotted versus the static magnetic field and the points can be fitted using equation (33). The resulting fit function will be evaluated at zero to get the hyperfine splitting. This method was not achievable with the previous setup [9], due to the orientation of the strip lines and the inhomogeneity of the static magnetic field. The results presented here are the first ones using this method.

3. **Calculating the hyperfine splitting using the π_1 and σ_1 transitions at the same static magnetic field**: If the transition values at same B-field of π_1 and σ_1 are known, the system of equations given by equations (32) and (33) can be solved to obtain the frequency at zero magnetic field:

$$\nu_0 = \frac{g_+\sqrt{g_+^2\nu_\sigma^2 - 4g_-^2\nu_\pi^2 + 4g_-^2\nu_\pi\nu_\sigma} + g_-^2(2\nu_\pi - \nu_\sigma)}{g_+^2 + g_-^2} \tag{89}$$

   where $g_\pm = g_I \pm g_J$.

All scans were fitted using equation (78) and the values of equations (79), (80), (81), (82), (83), (84), (85), and (86). Figures 53 and 54 give an example of a single σ_1 and π_1 scan, respectively. Three goodness-of-fit parameters are also given for the two examples. The sum of squares due to error (SSE) which measures the total deviation of the response values from the fit to the response values, the R-Square which measures how successful the fit is in explaining the variation of the data and the root mean squared error (RMSE) which estimates the standard deviation of the random component in the data.

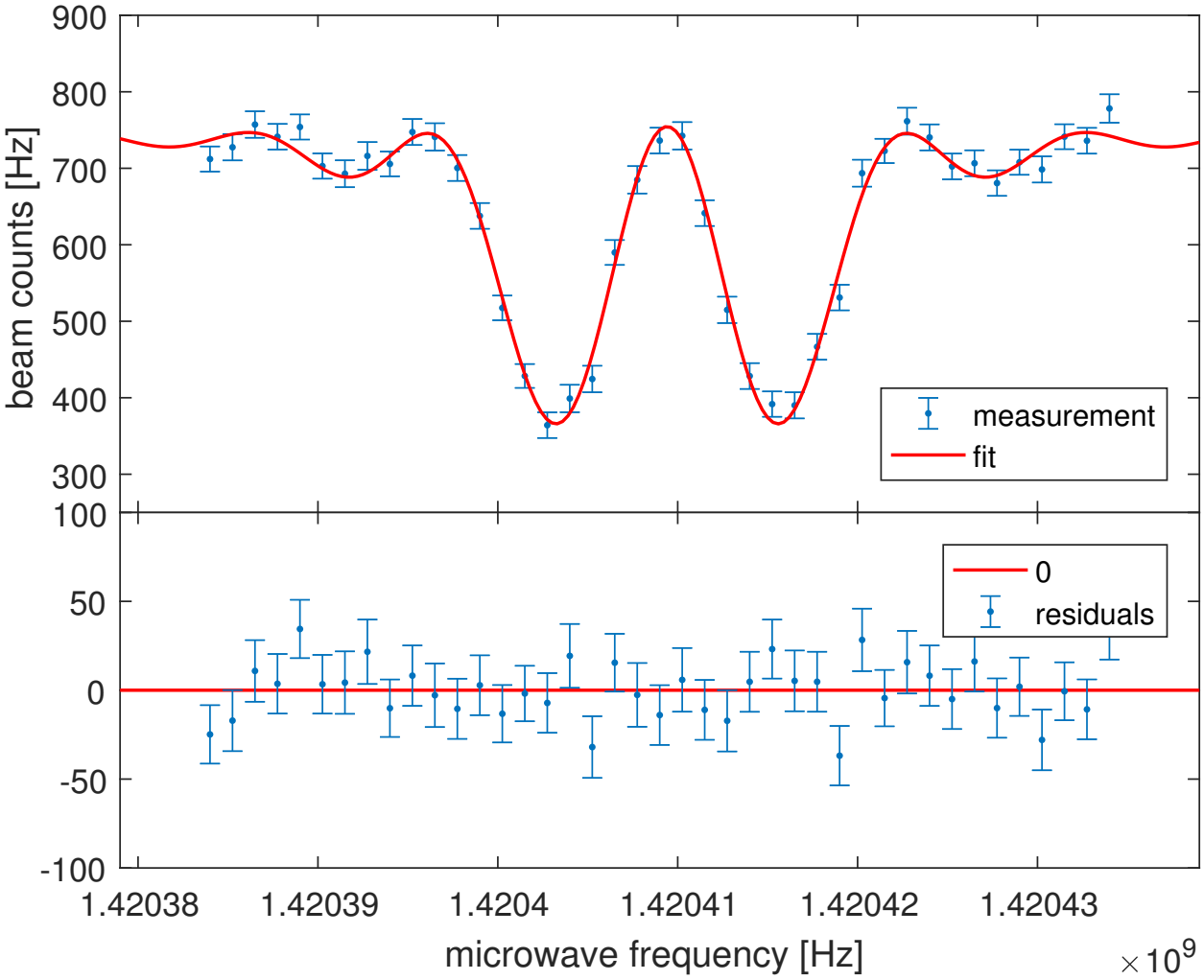

Figure 53: Upper part: Beam rate versus microwave frequency for the σ_1-transition. The beam counts are calculated by fitting a positive half-wave of a sine to the histogram of the count rate versus chopper phase [24]. Bottom part: Residuals. Goodness-of-fit: 1.SSE: 36.05 2.R-square: 0.98 3.Adjusted R-square: 0.98 4.RMSE: 1.00. Result for scan #1 of set #1 for a current of 0.5 A.

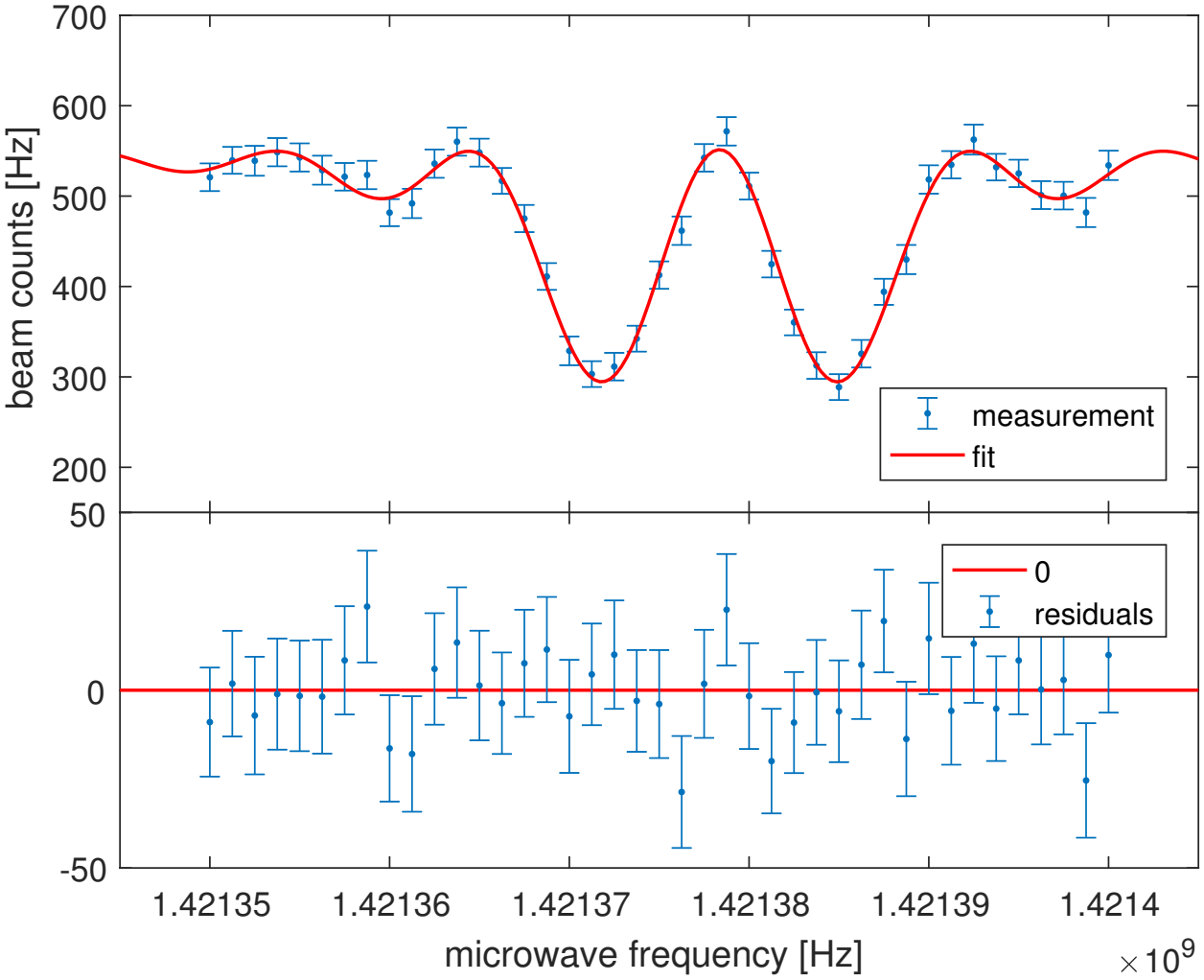

Figure 54: Upper part: Beam rate versus microwave frequency for the π_1 transition. The beam counts are calculated by fitting a positive half-wave of a sine to the histogram of the count rate versus chopper phase [24]. Bottom part: Residuals: Goodness-of-fit: 1.SSE: 22.04 2.R-square: 0.98 3.Adjusted R-square: 0.98 4.RMSE: 0.78. Result for scan #10 of set #7 for a current of 0.3 A

5.8.1 Results of the σ_1 extrapolation

Figure 56 shows the results of the σ_1 extrapolation for one set. Table 9 gives the results of the hyperfine splitting for all 13 sets.

Table 9: Hyperfine splitting frequencies obtain by the σ_1 extrapolation method

Set Number	ν_0 [Hz]
1	1420405801 ± 73
2	1420405734 ± 42
3	1420405780 ± 47
4	1420405819 ± 106
5	1420405839 ± 40
6	1420405736 ± 78
7	1420405730 ± 27
8	1420405732 ± 65
9	1420405810 ± 78
10	1420405777 ± 121
11	1420405815 ± 45
12	1420405712 ± 108
13	1420405654 ± 140

Figure 55 shows the results of table 9 compared to the literature value of ν_0.

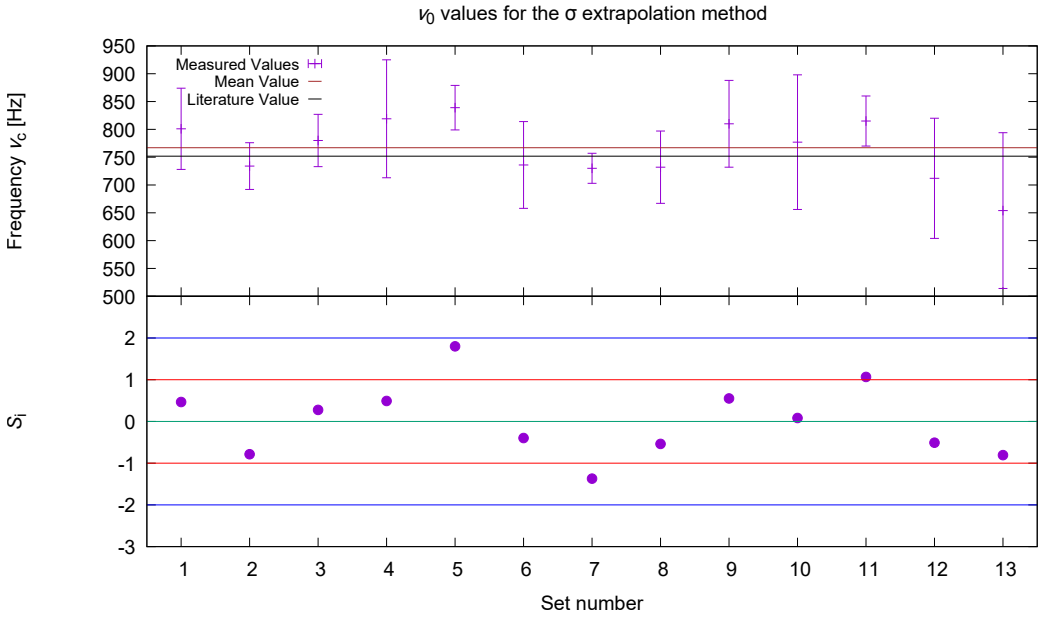

Figure 55: Upper part: Values for the ν_0 frequency obtained using the σ_1 extrapolation method (where $\nu_c = \nu_0 - 1420405000$). Bottom part: Standard score.

Using these values the weighted mean value was computed:

$$\boxed{\nu_0 = (1420405767 \pm 15)\text{Hz}} \tag{90}$$

This value deviates from the literature value by 15 Hz and agrees within the 1σ error. It has a relative error of 1.04×10^{-8}

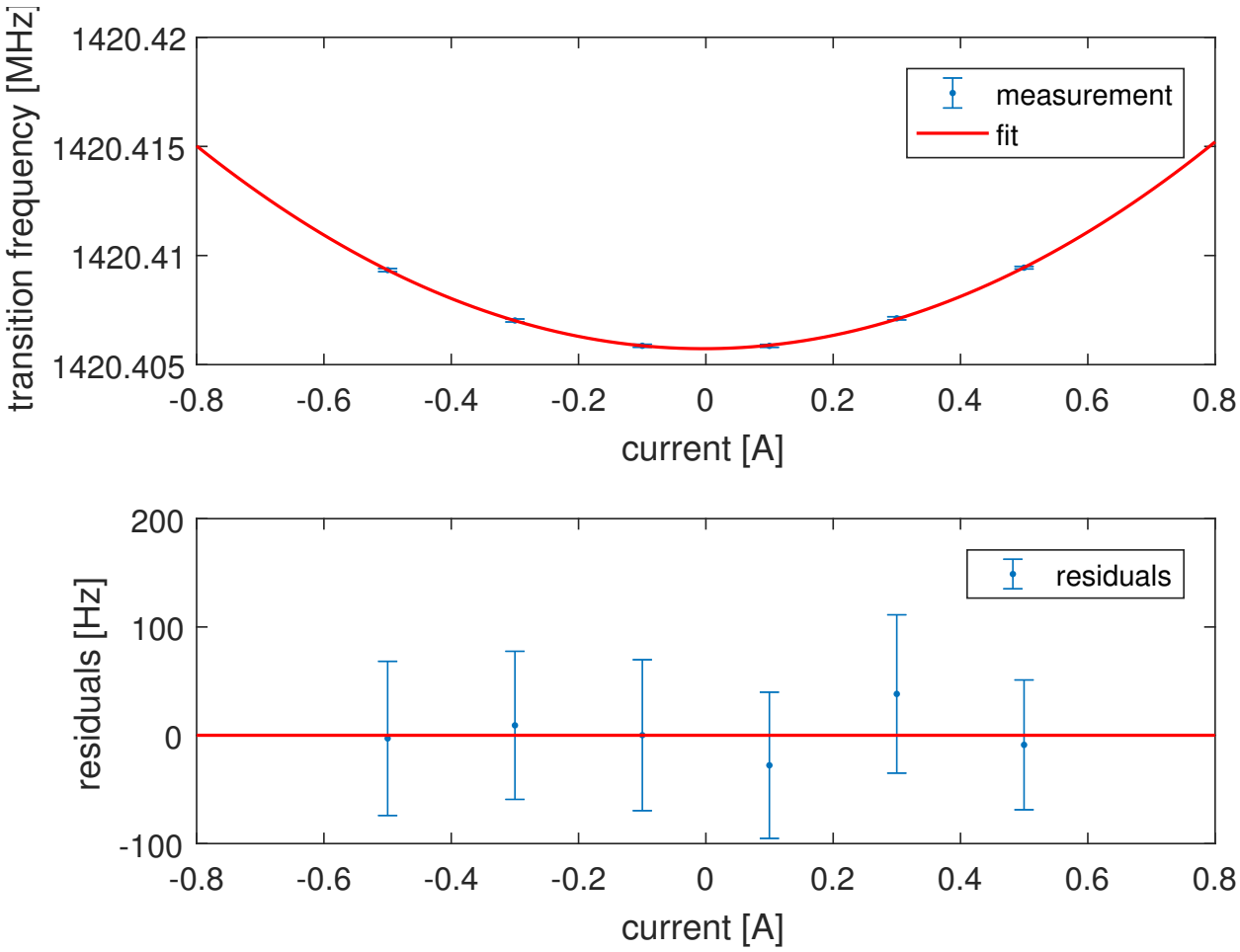

Figure 56: Upper part: Transition frequency for the σ_1 transitions versus the current. Bottom part: Residuals

5.8.2 Results of the π_1 extrapolation

Figure 58 shows the results of the π_1 extrapolation for one set. Table 10 gives the results of the hyperfine splitting for every set.

Table 10: Hyperfine splitting frequencies obtain by the π_1 extrapolation method

Set Number	ν_0 [Hz]
1	1420405697 ± 111
2	1420405674 ± 138
3	1420405788 ± 132
4	1420405824 ± 155
5	1420405798 ± 119
6	1420405732 ± 87
7	1420405742 ± 138
8	1420405611 ± 121
9	1420405779 ± 69
10	1420405729 ± 303
11	1420405908 ± 154
12	1420405758 ± 304
13	1420405928 ± 149

Figure 57 shows the results of table 10 compared to the literature value of ν_0.

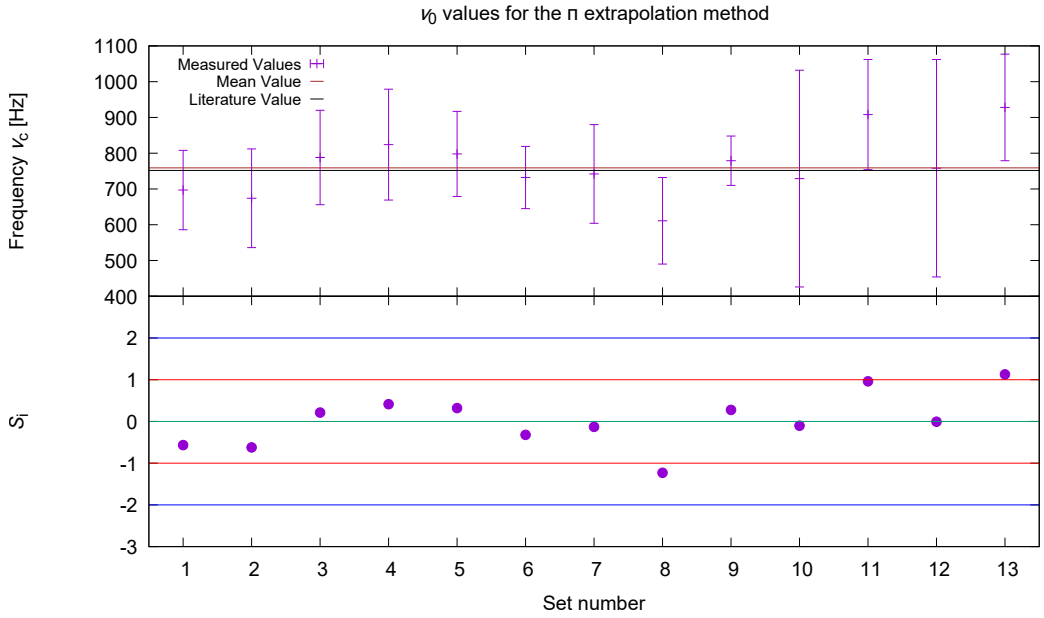

Figure 57: Upper part: Values for the ν_0 frequency obtained using the π_1 extrapolation method (where $\nu_c = \nu_0 - 1420405000$). Bottom part: Standard score.

Using these values the weighted mean value was computed:

$$\boxed{\nu_0 = (1420405760 \pm 34)\text{Hz}} \tag{91}$$

This value deviates from the literature value by 8 Hz and agrees within the 1σ error. It has a relative error of 2.38×10^{-8}

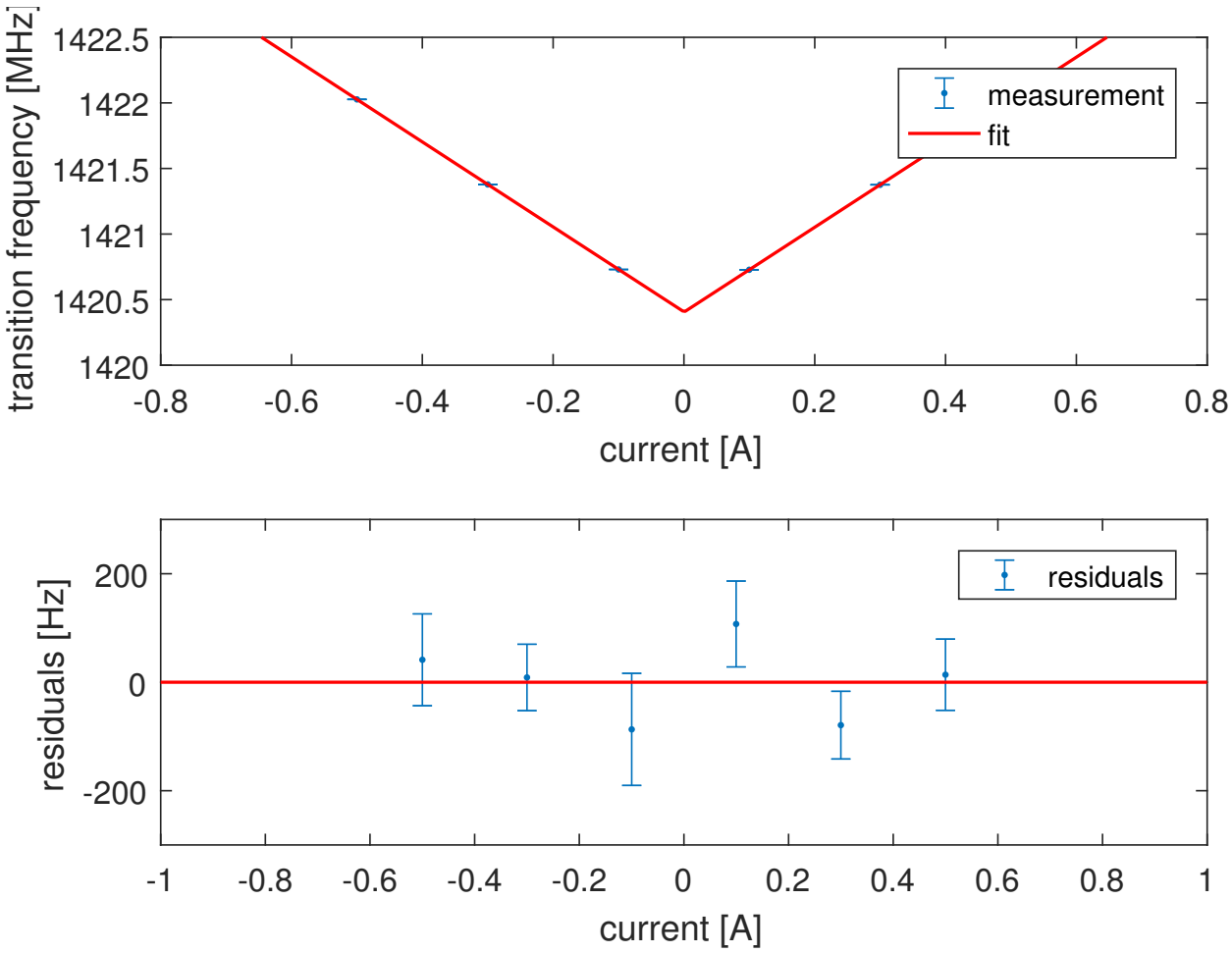

Figure 58: Upper part: Transition frequency for the π_1 transitions versus the current. Bottom part: Residuals

5.8.3 Results for the hyperfine splitting using both transitions at the same static magnetic field

For this method, for each σ_1 and π_1 scan pair the hyperfine splitting were calculated using equation (89). The obtained values were filtered by current. Afterwards, the weighted mean value was computed for each current. Table 11 gives the results of the hyperfine splitting for each current.

Table 11: Hyperfine splitting frequencies obtain with the π_1 and σ_1 transitions at the same static magnetic field.

Set Number	ν_0 [Hz]	Current [A]
1	1420405734 ± 18	0.5
2	1420405761 ± 19	0.3
3	1420405773 ± 20	0.1
4	1420405789 ± 20	-0.1
5	1420405724 ± 20	-0.3
6	1420405739 ± 20	-0.5

Figure 59 shows the results of table 11 compared to the literature value of ν_0.

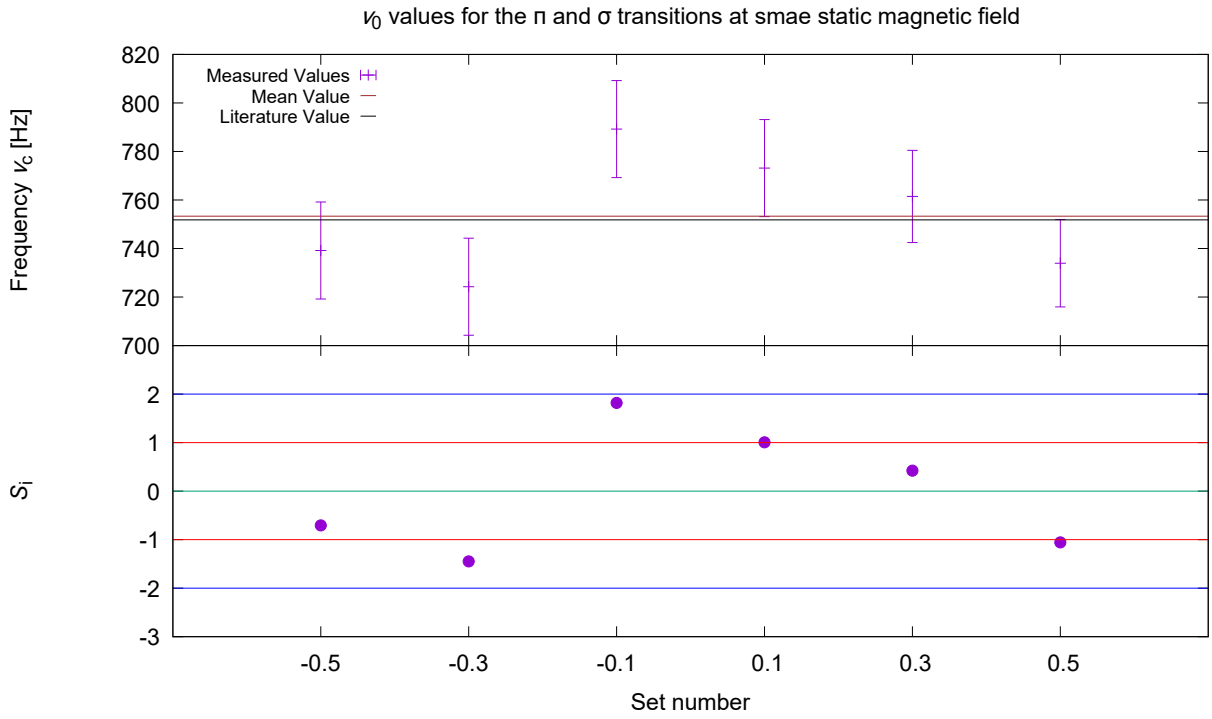

Figure 59: Upper part: Values for the ν_0 frequency obtained using the π_1 and σ_1 transitions at same static magnetic field (where $\nu_c = \nu_0 - 1420405000$). Bottom part: Standard score.

Using these values the weighted mean value was computed:

$$\boxed{\nu_0 = (1420405753 \pm 8)\text{Hz}} \tag{92}$$

This value deviates from the literature value by 1 Hz and agrees within the 1σ error. It has a relative error of 5.6×10^{-9}.

5.9 Discussion of the results

The final results using the three methods described in the previous sections are listed in table 12.

Table 12: Hydrogen ground state hyperfine splitting using the ASACUSA hydrogen beam.

	ν_0 [Hz]	Relative error	Deviation of literature value [Hz]
σ_1 extrapolation	1420405767 ± 15	1.04×10^{-8}	15
π_1 extrapolation	1420405760 ± 34	2.38×10^{-8}	8
Mean Value of the 2 extrapolations	1420405766 ± 14	9.96×10^{-9}	14
σ_1 and π_1 at same static magnetic field	1420405753 ± 8	5.60×10^{-9}	1

The mean values of the two extrapolation methods (third row of the above table) was computed in order to make a comparison between the third method (forth row) and the extrapolation methods. The third method uses all scans, however each extrapolation used just half of them. Combining the two will give a result that is based on the same data as the third method. From this table, it can be seen that the third calculation method is the one which gives a better precision. To improve the precision of the extrapolation methods, more points at low currents can be taken. This will improve the approximation of the fit function near the zero magnetic field regime. As expected the π_1-transition is harder to extrapolate because a small inhomogeneity has a bigger influence when calculating the transition at zero magnetic field. Nonetheless, the goal of this work was to show that with the new McKeehan-like coils the π_1 extrapolation method can be used. As mentioned in chapter 4, the coils can be moved even further apart, that could improve the homogeneity of the static magnetic field. Combining this possibility with doing more measurements at different currents will significantly improve the results of both extrapolation methods.

The result of the third method presented in this work was not able to surpass the precision obtained during the 2014 campaign (σ_1-transition) [9]. A possible reason for this could be the stability beam conditions of the hydrogen beam. For the 2014 setup (σ_1-transition) the total count rate was $\approx$ 2000 Hz and stayed at that number during the measurement. This time the count rate started at $\approx$ 1000 Hz and slowly decreased during the measurement. This was the reason why the measurement was stopped after 13 sets. During the 14th set the count rate was already $\approx$ 550 Hz and the fit quality decreased significantly. The effects of this drop in the count rate can also be seen in some of the scans of the last 2 sets. From the figures presented in the last 3 sections it can be seen that the uncertainty of the measurement point increases. The scans with higher point number are scans from the later sets. The decreased count rate at the end of the measurement resulted in a bigger uncertainty of the fit parameters which directly affected the calculation of the ground state hyperfine splitting. Another difference between this measurement and the 2014 campaign is the location of the H-beam. In 2014 the H-beam setup was located at another CERN building in a position perpendicular to the Earth magnetic field (E-W orientation). The influence of the Earth magnetic field in the direction of the beam was almost none. Now the setup is located at building 275 at a more parallel position to the Earth's magnetic field (N-S orientation). The component of the Earth's magnetic field parallel to the beam direction is harder to shield due to the unavoidable opening for the beam pipes. Additionally it cannot be compensated to zero by the coil's field and it exits the possibility that this generates a residual magnetic field. The extrapolation methods are affected by this residual magnetic

field and could cause a systematic shift towards higher frequencies. Indeed the mean values for the extrapolation methods are above the literature value and above the value of method three, however at the level of uncertainty this is not a significant effect.

The count rate decrease could be caused by the coldhead or the freeze out of residual gas to the Teflon tubing. If this happens some parts of the Teflon tube can get frozen and less atomic hydrogen will enter the beam line. The coldhead uses a heater to maintain the temperature at the set temperature. After some time the performance of the coldhead decreased and at some point the temperature will not stay constant and could rise above 20 K. As of right now the beam can run for 3 to 4 days without any inconvenience, but for longer runs of over a week a solution to the problems mentioned above has to be found.

The other reason for the higher relative error can be that the previous data was analyzed using ROOT while these resonances were analyzed using Matlab. There exists a possibility that ROOT's spline interpolation works better than Matlab's one, this results in fit parameters with smaller uncertainties. Possibly error bars are also handled differently, when fit parameters are fixed. These and other possible data analysis influences were not possible to be scrutinized in detail within the scope of this work. For that reason the results presented in table 12 can be considered as preliminary and thorough data analysis can be attempted to investigate for instance different effects of parameter fixing in C++/ROOT and Matlab.

6 Summary and Outlook

The ASACUSA hydrogen beam was constructed as a parallel experiment to the ASACUSA antihydrogen beam. It is an experiment which tests components of the antihydrogen GSHS spectroscopy beamline. An ultimate test is to measure the hydrogen GSHS following the Rabi method. The SME developed by the Kostelecky group motivated the idea of measuring the hyperfine structure of ground state antihydrogen because this transition presents one of the most precise test of the CPT symmetry on an absolute energy scale.

Previously [9], the superconducting sextupole was characterized with hydrogen and then returned to the antihydrogen experiment. After demonstrating a hydrogen GSHS determination based on the σ_1-transition the next mile stone was the preparation for the more demanding π_1-transition. The beam line was moved to a new building within CERN and the superconducting sextupole was replaced by permanent magnets. New optics were designed, simulated and tested for the new beam line [24].

In this work, the necessity of an extremely homogeneous static magnetic field due to the strong dependency of the π_1-transition to this field was explained. Also, a description of the new geometry for the coils and shielding was given. Simulated results were compared to the experimental data to find out the best position for the McKeehan-like coils. After this analysis the final value measured for the homogeneity of the static magnetic field was 590 ± 70 ppm, which is better than the maximal tolerable value to resolve the double peak structure. Afterwards, the new McKeehan-like coils and shielding were integrated into the beam line for the first time.

Finally, a five days measurement campaign was started, where the sigma and pi transitions have been measured repeatedly at a set of external B-field values. The hydrogen ground state hyperfine splitting was calculated using three different methods. Two of them were achievable for the first time using this setup. It was shown that by just measuring the π_1-transition, an extrapolation can be done to measure the transition at zero magnetic field. The extrapolation gave a result with a relative error of 2.38×10^{-8}. Showing this was the major goal of this work and it was a successful measurement. Nonetheless, there are ways to optimize the measurement to get better results. For instance, taking measurements at more than six coils currents. Furthermore, using the π_1 and σ_1 transitions at same static magnetic field a precision of 5.60×10^{-9} was reached. This is the second best precision for the ground state hyperfine structure using the Rabi spectroscopy method.

By the end of this master thesis the H-beam was left optimized and ready to undertake more measurements. Repeating the process done in chapter 5 with more than 13 sets will improve the precision of the measurement. Three weeks of taking data would be enough to surpass the result achieved in the previous campaign [9].

The H-beam still offers many opportunities and other type of measurements can be investigated using the setup. For instance, the McKeehan-like coils can be moved further apart to see if the homogeneity improves. A more stable source and cooling system can be applied to perform longer runs of data taking.

Moreover, the oscillating magnetic field inside the cavity can be investigated to see if it is really trajectory independent in the x-y plane. The new frame where the cavity is mounted can be moved and allows for probing different parts of the cavity volume with the comparatively small hydrogen beam. This is of interest for the antihydrogen beam, which is expected to fill the whole volume. Measuring the hyperfine splitting at different positions can tell if the spin flip probability is trajectory independent.

The H-beam can also become an independent experiment to test the CPT symmetry. The group led by Kostelecky group showed that depending on the position of the Earth the transition frequencies could experience a shift. A long run measurement could test for the

annual and sidereal effects of the transition frequency. That would set limits to some of the SME coefficients. The other possible measurement is to change from hydrogen to deuterium. Measurements with deuterium can also be used to test the CPT symmetry and set some boundaries on SME coefficients [40].

Appendix A Surface zonal harmonic

The zonal surface harmonics are defined as:

$$P_n(x) = M_n(A_n x^n - A_{n-2}x^{n-2} + \cdots) \tag{93}$$

with:

Table 13: Values to order 12 of the zonal surface harmonics terms

n	M_n	A_n	A_{n-2}	A_{n-4}	A_{n-6}	A_{n-8}	A_{n-10}	A_{n-12}
0	1/1	1						
1	1/1	1						
2	1/2	3	1					
3	1/2	5	3					
4	1/8	35	30	3				
5	1/8	63	70	15				
6	1/16	231	315	105	5			
7	1/16	429	693	315	35			
8	1/128	6435	12012	6930	1260	35		
9	1/128	12155	25740	18018	4620	315		
10	1/256	46189	109395	90090	30030	3465	63	
11	1/256	88179	230945	218790	90090	15015	693	
12	1/1024	676039	1939938	2078505	1021020	225225	18018	231

The first derivative is given by:

$$P'_n(x) = M_{n-1}(A_{n-1}x^{n-1} - A_{n-3}x^{n-3} + \cdots) \tag{94}$$

with:

Table 14: Values to order 12 for the first derivative

n	M_{n-1}	A_{n-1}	A_{n-3}	A_{n-5}	A_{n-7}	A_{n-9}	A_{n-11}
1	1/1	1					
2	3	1					
3	3/2	5	1				
4	5/2	7	3				
5	15/8	21	14	1			
6	21/8	33	30	5			
7	7/16	429	495	135	5		
8	9/16	715	1001	385	35		
9	45/128	2431	4004	2002	308	7	
10	55/128	4199	7956	4914	1092	63	
11	33/256	29393	62985	46410	13650	1365	21
12	39/256	52003	124355	106590	39270	5775	231

Appendix B S-Parameters of the vector network analyzer (VNA)

The VNA is an instrument that allows the characterization of microwave or radio frequency devices through the scattering parameter (S-Parameters). For the measurement done in section 5.2 the VNA was used as a two port VNA system. For a two port system the S-Parameter matrix is given by:

$$\begin{bmatrix} b_1 \\ b_2 \end{bmatrix} = \begin{bmatrix} S_{11} & S_{12} \\ S_{22} & S_{21} \end{bmatrix} \begin{bmatrix} a_1 \\ a_2 \end{bmatrix} \tag{95}$$

where a_i is the incident power and b_i is the reflected power. The S-parameter are the given by:

$$S_{11} = \frac{b_1}{a_1} \tag{96}$$

$$S_{12} = \frac{b_1}{a_2} \tag{97}$$

$$S_{22} = \frac{b_2}{a_2} \tag{98}$$

$$S_{21} = \frac{b_2}{a_1} \tag{99}$$

The S-parameters can be defined as:

- S_{11}: is the input port voltage reflection coefficient.
- S_{12}: is the reverse voltage gain.
- S_{22}: is the output port voltage reflection coefficient.
- S_{21}: is the forward voltage gain.

References

[1] Carl D. Anderson. The positive electron. *The Physical Review*, 43:491, 1933.

[2] G. Bauer et al. Production of antihydrogen. *Physics Letters B*, 368:251, 1996.

[3] D. Colladay and A. Kostelecký. Lorentz-violating extension of the standard model. *Physical Review*, 58:1–23, 1998.

[4] D. Colladay and A. Kostelecký. CPT and lorentz test in hydrogen and antihydrogen. *Phys.Rev.Lett*, 82:2254, 1999.

[5] L. Essen et al. Frequency of the hydrogen maser. *Nature*, 229:110–111, 1971.

[6] H. Hellwig et al. Measurement of the unperturbed hydrogen hyperfine transition frequency. *IEEE Transactions on Instrumentation and Measurement*, 19:200–209, 1970.

[7] N. Ramsey. Experiments with separated oscillatory fields and hydrogen masers. *Rev.Mod.Phys.*, 62:541–552, 1990.

[8] S.G. Karshenboim. Some possibilities for laboratory searches for variations of fundamental constants. *Can. J. Phys.*, 78:639–678, 2000.

[9] M. Diermaier. *Determination of the Hydrogen Ground-State Hyperfine Splitting in a Beam and Perspectives for Antihydrogen.* PhD thesis, Vienna University of Technology, 2016.

[10] C. S. Wu et al. Experimental test of parity conservation in beta decay. *The Physical Review*, 105:1413, 1957.

[11] J. H. Christenson et al. Evidence for the 2π decay of the K_2^0 meson. *The Physical Review*, 13:138, 1964.

[12] Weisskopf V Pauli W., Rosenfelf L. *Niels Bohr and the Development of Physics.* McGraw-Hill, 1955.

[13] J. Schwinger. The theory of quantized fields. I. *Physical Reviews*, 82:914, 1951.

[14] S. G. Karshenboim. Some possibilities for laboratory searches for variations of fundamental constants. *Can.J.Phys.*, 78:639–678, 1951.

[15] P.J. Mohr et al. CODATA recommended values of the fundamental physical constants: 2014. *Rev. Mod. Phys.*, 88:035009, 2016.

[16] R. Loudon. *The Quantum Theory of Light.* Oxford University Press, 2000.

[17] B. Kolbinger. Numerical simulation of hyperfine transition in antihydrogen. Master's thesis, University of Vienna, 2014.

[18] I. I. Rabi et al. The molecular beam resonance method for measuring nuclear magnetic moments. the magnetic moments of ${}_3\mathrm{Li}^6$, ${}_3\mathrm{Li}^7$, ${}_9\mathrm{F}^{19\star}$. *Phys. Rev.*, 55:526–535, 1939.

[19] N. Kuroda et al. A source of antihydrogen for in-flight hyperfine spectroscopy. *Nature communications*, 5:3089, 2014.

[20] E. Widmann et al. Measurement of the antihydrogen hyperfine structure in a beam. *Hyperfine Interactions*, 215:1–8, 2013.

[21] J. Eades et al. Measurement of the antihydrogen hyperfine structure. *Tech.Rep. CERN-SPSC-2003-009.SPSC-I-226*, 2003.

[22] P.A. Thonet. Use of permanent magnets in multiple projects at cern. *IEEE Transactions on Applied Superconductivity*, 26:110–111, 2016.

[23] M. Fleck. Design of a permanent halbach sextupole magnet. Technical report, Vienna University of Technology, 2015.

[24] M. Wiesinger. Design and implementation of new optics for the atomic hydrogen beam of ASACUSA's antihydrogen hyperfine spectroscopy experiment. Master's thesis, Vienna University of Technology, 2017.

[25] M. Huzan. CERN summer student programme at the h-beam, ASACUSA. Technical report, CERN, `http://cds.cern.ch/record/2217860`, 2016.

[26] M. Wolf. Lock-in based detection scheme for a hydrogen beam. Master's thesis, University of Vienna, 2013.

[27] MKS Instrument. Quadrupole mass spectrometer theory - ion source, mass filter, detector, control unit. `https://link.springer.com/article/10.1007%2FBF01392963`.

[28] S. Federmann. *A Spin-Flip Cavity for Microwave Spectroscopy of Antihydrogen*. PhD thesis, University of Vienna, 2012.

[29] C. Sauerzopf. *The ASACUSA Antihydrogen Detector: Development and Data Analysis*. PhD thesis, Vienna University of Technology, 2016.

[30] L.W. McKeehan. Combination of circular currents for producing uniform magnetic fields. *Review of Scientific Instruments*, 7:150, 1936.

[31] F.E. Neumann. *Vorlesungen über elektrische Ströme*. Leipzig, B.G. Teubner, 1884.

[32] G. Fanselau. Die erzeugung weitgehend homogener magnetfelder durch kreisstöme. *Zeits.f.Physik*, 54:260–269, 1929.

[33] M. Nikolic. The shielding factor of the magnetic shielding for the spin-flip cavity of ASACUSA's antihydrogen experiment simulated with comsol-multiphysics. Technical report, Bachelor Thesis, University of Vienna, 2016.

[34] C. Malbrunot et al. Spectroscopy apparatus for the measurement of the hyperfine structure of antihydrogen. *Hyperfine Interactions*, 228:61, 2014.

[35] Physik Instrument. M-404 precision translation stage. `https://www.physikinstrumente.com//en/products/linear-stages-and-actuators/stages-with-motor-screw-drives/`.

[36] Bartington. Mag-03 three-axis magnetic field sensor. `http://www.bartington.com/presentation/mag-03-three-axis-magnetic-field-sensor`.

[37] C.B. Jepsen. CERN summer student work project report: Data taking and simulation-based data analysis at the ASACUSA experiment. Technical report, CERN, `http://cds.cern.ch/record/1752579`, 2014.

[38] M. Diermaier et al. In-beam measurement of the hydrogen hyperfine splitting and prospects for antihydrogen spectroscopy. *Nature*, 8:15749, 2017.

[39] R. Birge. The calculation of error by the method of least squares. *Physics Review*, 40:207, 1932.

[40] J. Vargas and A. Kostelecký. Lorentz and CPT test with hydrogen, antihydrogen, and related systems. *Physical Review*, 92:056002, 2015.